AIR FORCE ACADEMY

# Design of a Class I Remotely Piloted Aircraft for Maritime Surveillance

## Performance, Aerodynamics and Stability

**Vasco Henrique Reis Franco**

***ALFAL/ENGAER 138080-L***

Thesis to obtain the Master of Science Degree in

## Military and Aeronautical Sciences - Aeronautical Engineering

### Examination Committee

| | |
|---|---|
| Chairperson: | MGEN/ENGAER 076441-J Paulo Manuel Veloso Gonçalves Guerra |
| Supervisor: | MAJ/ENGAER 129905-A Luís Filipe da Silva Félix |
| Co-Supervisor: | CAP/ENGAER 131603-G João Vítor Aguiar Vieira Caetano |
| Member of the Committee: | Doutor Frederico José Prata Rente Reis Afonso |

**Sintra, May 2018**

*“O ignorante afirma, o sábio duvida, o sensato reflete.”*

**Aristóteles**

Dedicado à Inês, família e amigos.

# Agradecimentos

Gostaria de endereçar votos de gratidão a um conjunto de pessoas cuja intervenção e auxílio prestado se revestiram da maior importância na realização do presente trabalho.

Primeiramente, ao Major, Engenheiro Aeronáutico, Luís Félix e ao Capitão, Engenheiro Aeronáutico, João Caetano, agradeço a proposta do tema e orientação providenciada ao longo da realização do trabalho. A forma constante e sempre presente como, desde o início, incentivaram e acompanharam a evolução do projecto, oferecendo *feedback* e sugestões pertinentes em todas as suas etapas, revelou-se fulcral para o cumprimento dos objectivos incialmente propostos.

Dirijo um grande obrigado e um forte abraço ao meu camarada, aluno da especialidade de Engenharia Aeronáutica, João Correia, que me acompanhou ao longo do caminho, nomeadamente na fase conceptual do projecto, na qual foi necessária uma forte cooperação e união de esforços de modo a levá-lo a bom porto.

Ao Tenente, Engenheiro Aeronáutico, Ricardo Veríssimo, demonstro a minha profunda gratidão pelo auxílio providenciado em matéria de mecânica de fluidos computacional, através da utilização do programa comercial Star-CCM+. Apesar de não estar, em momento algum, ligado ao presente projecto e como tal este não ser da sua responsabilidade, sempre demonstrou uma prontidão e predisposição para ajudar tremendas. Por ter facultado o seu próprio trabalho final de mestrado *Best Practice Guidelines in CFD External Aerodynamics: Applied to Unmanned Aerial Vehicles at Cruise Conditions* e esclarecido muitas dúvidas, frequentemente em horas menos oportunas, é merecedor de toda a minha estima e gratidão.

Agradeço também ao Tenente, Engenheiro Eletrotécnico, Diogo Silva por garantir, muitas vezes fora do seu horário de serviço, a pronta utilização de equipamento informático indispensável à consecução do projecto.

Ao Major, Técnico de Manutenção de Material Aéreo, Aurélio Santos, e ao Sargento-Ajudante, Operador Radarista de Deteção, Paulo Mendes, membros do Centro de Investigação da Academia da Força Aérea, agradeço a disponibilidade demonstrada para, em várias ocasiões, comigo reunirem e debaterem o projecto.

Sem os referidos contributos, este trabalho não teria sido possível.

# Resumo

É objetivo da presente dissertação o projeto de um veículo aéreo não tripulado de classe I, para vigilância marítima, monitorização de poluição atmosférica e apoio a missões de busca e salvamento. O seu desenvolvimento engloba a totalidade do projeto conceptual e parte do preliminar, com foco nas áreas de aerodinâmica, estabilidade de voo, design exterior e desempenho em voo. Os requisitos de missão baseiam-se nas especificações da Agência Europeia de Segurança Marítima.

A abordagem ao projeto conceptual segue uma metodologia intuitiva através da qual a aeronave é concebida passo a passo, de forma iterativa, utilizando folhas de cálculo. Inicia-se com a elaboração e consequente selecção de vários possíveis conceitos de veículos aéreos, baseados nos resultados de uma prévia pesquisa de mercado. Segue-se uma estimativa inicial do peso máximo à descolagem, dimensionamento da asa principal, fuselagem, estabilizador horizontal e vertical, e caracterização do sistema propulsor. Após uma análise refinada da distribuição de peso, é auferida a estabilidade estática e dinâmica da aeronave, incluindo o dimensionamento das superfícies de controlo, e analisa-se o desempenho em voo da mesma. Esta abordagem baseia-se em dados empíricos recolhidos de várias fontes bibliográficas e simulações computacionais efetuadas através do programa XFLR5.

Na fase preliminar, é empregue o programa Star-CCM+, ferramenta de mecânica de fluidos computacional, num estudo paramétrico da geometria da asa principal com vista à maximização da autonomia em voo. Adicionalmente, outros componentes são analisados e o projeto é refinado.

Como produto da dissertação, é apresentada uma aeronave conceptual capaz de cumprir os requisitos de missão impostos. Do estudo paramétrico conclui-se que os benefícios aerodinâmicos não compensam os prejuízos estruturais e de manufatura.

**Palavras-chave:** Veículo Aéreo Não Tripulado, Vigilância Marítima, Projeto Aeronáutico, Desempenho, Aerodinâmica, Mecânica de Fluidos Computacional.

# Abstract

It is the present dissertation's objective to design a class I remotely piloted aircraft, intended for maritime surveillance, atmospheric pollution monitoring and search and rescue missions. Its development encompasses the entirety of conceptual design and part of preliminary design, focusing on aerodynamics, flight stability, exterior design and flight performance. Mission requirements are set to comply with the European Maritime Safety Agency's specifications.

The approach to conceptual design follows an intuitive methodology in which the airplane is conceived in a step-by-step, iterative fashion, making use of spreadsheets. It starts with an aircraft concept generation, based on a previous market research, and subsequent concept selection. An initial estimate of maximum take-off weight follows, as well as sizing of the main wing, fuselage, horizontal and vertical stabilizers and a characterization of the propulsion system. After a refined weight analysis, static and dynamic stabilities are evaluated, which includes the sizing of control surfaces, and the aircraft flight performance is assessed. This approach relies on empirical data gathered from various sources and computational simulations conducted with the software XFLR5.

In preliminary design, the software Star-CCM+, a computational fluid dynamics tool, is employed in a main wing's geometry parametric study, performed with the aim of maximizing endurance. Additionally, other aircraft components are analysed and the design is refined.

As the dissertation's output, a conceptual aircraft capable of meeting the demanded mission requirements is presented. The main wing parametric study concludes that the aerodynamic benefits fail to balance the structural and manufacture drawbacks.

**Keywords:** Remotely Piloted Aircraft, Maritime Surveillance, Aircraft Design, Performance, Aerodynamics, Computational Fluid Dynamics.

# Contents


**1 Introduction** **1**

1.1 Background . . . . . 1

1.2 Motivation . . . . . 3

1.3 Objectives . . . . . 5

1.4 Method . . . . . 6

1.5 Layout . . . . . 7

**2 Fundamental Concepts & State-of-the-Art** **8**

2.1 The Design Process . . . . . 8

2.1.1 Design Method . . . . . 8

2.1.2 Aircraft Design . . . . . 8

2.1.3 Conceptual Design Approach . . . . . 11

2.2 Performance & Aerodynamics . . . . . 12

2.2.1 Performance . . . . . 12

2.2.2 Viscous Flow . . . . . 14

2.2.3 Drag . . . . . 16

2.2.4 Drag Reduction Techniques . . . . . 17

2.3 XFLR5 . . . . . 18

2.3.1 XFOIL . . . . . 19

2.3.2 Vortex Lattice Method . . . . . 20

2.4 Computational Fluid Dynamics . . . . . 21

2.4.1 Approximation Models . . . . . 22

2.4.2 Turbulence Models . . . . . 24

2.4.3 Transition Models . . . . . 27

2.4.4 Spacial Discretization: Meshing . . . . . 28

2.4.5 Near-Wall Treatment . . . . . 31

2.5 RPA Design Features . . . . . 32

2.5.1 Wing System Configuration . . . . . 32

2.5.2 Propulsion Integration . . . . . 34

2.5.3 Fuselage Configuration . . . . . 36

2.5.4 Tail Configuration . . . . . 36

2.6 Market Research . . . . . 37

**3 Conceptual Design** **41**

3.1 Concept Generation & Selection . . . . . 41

3.1.1 Concept Generation . . . . . 41

3.1.2 Concept Selection . . . . . 43

3.2 Preliminary Estimate of Maximum Take-Off Weight . . . . . 45

3.3 Design Point - Wing Loading and Power-to-Weight Ratio Selection . . . 49

3.4 Wing Design . . . . . 52

3.4.1 Planform Definition & Flight Regime Characterization . . . . . 52

3.4.2 Airfoil Selection . . . . . 52

3.4.3 Wing Drag Estimation . . . . . 55

3.5 Enhanced Lift Design . . . . . 56

3.6 Fuselage Sizing . . . . . 57

3.7 Tail Design . . . . . 59

3.7.1 Horizontal Tail Sizing . . . . . 59

3.7.2 Vertical Tail Sizing . . . . . 61

3.8 Propulsion System . . . . . 62

3.8.1 Drag Build-Up . . . . . 62

3.8.2 Engine Performance . . . . . 64

3.9 Refined Weight Analysis . . . . . 65

3.10 Static Stability . . . . . 67

3.10.1 Static Margin . . . . . 67

3.10.2 Stability Derivatives . . . . . 68

3.10.3 Tail Force & Trim Drag . . . . . 69

3.10.4 Control Surfaces Sizing . . . . . 70

3.11 Dynamic Stability . . . . . 71

3.12 Performance . . . . . 72

3.12.1 Stall Speed & Cruise Velocity Optimization . . . . . 72

3.12.2 Steady Climbing, Gliding and Level Turning Flight . . . . . 74

3.12.3 Take-off and Landing . . . . . 76

3.13 Aircraft Layout and Characteristics . . . . . 78

**4 Preliminary Design** **81**

4.1 2D Analysis: Methodology Validation . . . . . 81

4.1.1 Methodology Definition . . . . . 81

4.1.2 Results & Validation . . . . . 86

4.1.3 Application to 3D Flow . . . . . 89

4.2 3D Analysis: Wing Configuration Parametric Study . . . . . 90

4.2.1 Configuration Layout . . . . . 90

4.2.2 Parametric Study Results . . . . . 93

4.3 Vertical Tail Planform . . . . . 96

4.4 Horizontal Tail Incidence . . . . . 97

**5 Conclusions & Recommendations** **98**

5.1 Conclusions . . . . . 98

5.2 Recommendations . . . . . 99

# List of Figures


1 Aircraft development process. Adapted from [12]. . . . . 9
2 Boundary layer development over a flat plate. Adapted from [20]. . . . . 15
3 Representation of elemental panels and horseshoe vortices for a typical wing planform in the Vortex Lattice Method. Adapted from [31]. . . . . 20
4 Examples of structured meshes: (a) non-uniform cartesian, (b) body-fitted C, (c) multi-block. Adapted from [37]. . . . . 29
5 Examples of unstructured meshes: (a) triangular, (b) hexahedral, (c) hybrid. Adapted from [37]. . . . . 30
6 Wing system configurations. Adapted from [2]. . . . . 32
7 (a) Pusher (adapted from [4]) and (b) tractor (adapted from [46]) arrangements. . . . . 35
8 Examples of tail arrangements. Adapted from [2]. . . . . 36
9 (a) MiniFalcon (adapted from [48]), (b) Nasnas MK1 (adapted from [47]), (c) AR5 (adapted from[49]) and (d) Antex X03 (adapted from [7]). . . . . 39
10 Sketches of several aircraft concepts: (a) Configuration 1, (b) Configuration 2, (c) Configuration 3, (d) Configuration 4, (e) Configuration 5, (f) Configuration 6. . . . . 41
11 AHP hierarchy. . . . . 44
12 Mission profile. . . . . 46
13 Maximum take-off weight vs aspect ratio. . . . . 48
14 Representation of a segment of the design space and identification of the design point. Range, endurance and glide ratio lines are not represented. 50
15 SG6042 airfoil. Adapted from [58]. . . . . 53
16 Schematic of trailing-edge plain and slotted flaps. Adapted from [10]. . . 56
17 Fuselage total drag vs fineness fatio. . . . . 59
18 NACA 0009 airfoi. Adapted from [52]. . . . . 61
19 Maximum take-off weight and respective subgroups. Units in kg. . . . . 66
20 Thrust (a) and power (b) required vs cruise velocity. . . . . 74
21 Climb rate (a) and sink rate (b) vs cruise velocity. . . . . 74
22 (a) Take-off and (b) landing breakdown schematic. Adapted from [11]. . 77
23 Projected view. . . . . 78

24 Front view. . . . . 79
25 Top view. . . . . 79
26 Lateral-projected view. . . . . 79
27 Detail of the 2D mesh surrounding the SG6042 airfoil. . . . . 86
28 (a) Lift coefficient vs angle of attack and (b) drag coefficient vs lift coefficient curves for the experimental data and both computational simulations at Reynolds numbers of $1 \times 10^6$ and $5 \times 10^5$. . . . . 88
29 Pressure coefficient distribution over the SG6042 airfoil with AoA=0°and $Re = 1 \times 10^6$. . . . . 88
30 Configurations A (a) and B (b). C and D have the same planform shape but different twist angles, hard to notice, hence not represented. Only half span is displayed. . . . . 92
31 (a) Lift coefficient vs angle of attack and (b) drag coefficient vs lift coefficient curves for both Star-CCM+ and XFLR5 simulations of configuration A. $Re = 1 \times 10^6$. . . . . 93
32 Rectangular (a) and tapered (b) planforms of each panel of the vertical stabilizer. Only half span is represented. . . . . 96

# List of Tables


1 Design proposal adapted from EMSA and provided by the AFARC. . . . 4
2 Market research results. . . . 38
3 Evaluation of the generated concepts according to the AHP. . . . 45
4 Payload, avionics and propulsion system weights. . . . 46
5 Fuel weight fractions. . . . 47
6 Maximum wing loading ($N/m^2$) allowed for each flight condition or requirement. . . . 50
7 Wing loading ($N/m^2$) and power-to-weight ratio (W/N) for similar aircrafts. 51
8 Comparison between wing loading and power-to-weight ratio values for the different approaches employed. Units as in table 7. . . . 51
9 Wing geometric parameters. Formulas taken from [10]. . . . 52
10 Performance results of the top six best airfoils. . . . 54
11 Performance characteristics of different trailing-edge devices. . . . 57
12 Performance results of NACA airfoils considered for the tail design. . . . 60
13 UAV Engines's *AR741* specifications. . . . 64
14 Structural weight determined by crewd aircraft [10] and RPA [2] statistical approaches. Units are in kg. . . . 66
15 Longitudinal oscillatory modes and their respective natural frequencies, $\omega_n$, and damping factors, $\xi$. . . . 72
16 Lateral-directional oscillatory modes and their respective natural frequencies, damping factors, time constants, $\tau$, and time to double the amplitude, $t_2$. . . . 72
17 Stall speed at different flight conditions. . . . 73
18 Rate of climb at different flight conditions. Flight speed, $V$, and the ratio of flight and stall speed, $V/V_s$, are represented for comparison purposes. 75
19 Glide ratio and sink rate at different flight conditions. Flight speed, $V$, and flight and stall speed ratio, $V/V_s$, are represented for comparison purposes. . . . 75
20 Take-off distance under different conditions. All distances in meters. . . 77
21 Landing distance under different conditions. All distances in meters. . . 77
22 Summary of the aircraft's main characteristics. . . . 80

23 Best practice guidelines concerning the physics model. . . . . 82
24 Comparison between experimental and computational results for $Re = 5 \times 10^5$. Deviation of the latter from the former is expressed as a percentage. Angles in degrees. . . . . 87
25 Comparison between experimental and computational results for $Re = 5 \times 10^5$. Deviation of the latter from the former is expressed as a percentage. Angles in degrees. . . . . 87
26 Wing configurations subject to CFD analysis. Twist angle in degrees. . . 92
27 Star-CCM+ results of all four wing configurations at an angle of attack of 4°. . . . . 94
28 Performance of various wing arrangements. . . . . 95

# List of Abbreviations

| | |
|---|---|
| 2D | Two-Dimensional |
| 3D | Three-Dimensional |
| AFARC | Air Force Academy Research Center |
| AHP | Analytic Hierarchy Process |
| AIS | Automatic Identification System |
| AMSL | Above Mean Sea Level |
| AoA | Angle of Attack |
| BSL | Baseline |
| CAD | Computer-Aided Design |
| CFD | Computational Fluid Dynamics |
| CG | Center of Gravity |
| CPU | Central Processing Unit |
| DDD | Dull, Dirty and Dangerous |
| DNS | Direct Numerical Simulation |
| DP | Design Proposal |
| EEZ | Exclusive Economic Zone |
| EMSA | European Maritime Safety Agency |
| EO | Electro-Optic |
| EU | European Union |
| FDM | Finite Difference Method |
| FEM | Finite Element Method |
| FVM | Finite Volume Method |
| GPS | Global Positioning System |
| GR | Glide Ratio |
| IR | Infrared |
| ISR | Intelligence, Surveillance and Reconnaissance |
| HP | Horsepower |
| LEBU | Large Eddy Break-Up |
| LES | Large Eddy Simulation |

| | |
|---|---|
| LEVM | Linear Eddy Viscosity Models |
| LLT | Lifting Line Theory |
| LOS | Line-of-Sight |
| LRN | Low Reynolds Number |
| LSB | Laminar Separation Bubble |
| MAV | Micro Air Vehicle |
| MSL | Mean Sea Level |
| MTOW | Maximum Take-Off Weight |
| NATO | North Atlantic Treaty Organization |
| NLEVM | Non-Linear Eddy Viscosity Models |
| NP | Neutral Point |
| OCH | Onboard Computation Hardware |
| PAF | Portuguese Air Force |
| PBM | Parts-Based Meshing |
| PM | 3D Panel Method |
| RANS | Reynolds Averaged Navier-Stokes |
| RBM | Regions-Based Meshing |
| RDI | Research, Development and Innovation |
| ROC | Rate of Climb |
| RPA | Remotely Piloted Aircraft |
| RPAS | Remotely Piloted Aircraft Systems |
| RSTM | Reynolds Stress Transport Models |
| SAR | Search and Rescue |
| SIR | Sink Rate |
| SR | Synthetic Aperture Radar |
| SatCom | Satellite Communications |
| SCM | Second Closure Models |
| SST | Shear-Stress Transport |
| STOL | Short Take-Off and Landing |
| TS | Tollmien-Schlichting |
| TSB | Transitional Separation Bubble |
| TVR | Turbulent Viscosity Ratio |

| | |
|---|---|
| UA | Unmanned Aircraft |
| UAS | Unmanned Aircraft Systems |
| US | United States |
| VLM | Vortex Lattice Method |

# List of Symbols

## Greek Symbols

| | |
|---|---|
| $\alpha$ | Angle of Attack |
| $\alpha_{0_L}$ | Zero-Lift Angle of Attack |
| $\alpha_s$ | Stall Angle of Attack |
| $\alpha_{trim}$ | Trim Angle of Attack |
| $\beta$ | Sideslip Angle |
| $\delta$ | Boundary Layer Thickness |
| $\delta_f$ | Flap Deflection Angle |
| $\epsilon$ | Dissipation of Turbulent Energy |
| $\eta_p$ | Propeller Efficiency |
| $\theta$ | Wing Twist |
| $\lambda$ | Taper Ratio |
| $\Lambda_{LE}$ | Leading Edge Sweep Angle |
| $\Lambda_{t/c}$ | Maximum Thickness Line Sweep Angle |
| $\mu$ | Dynamic Viscosity |
| $\mu_r$ | Rolling Friction Coefficient |
| $\mu_t$ | Dynamic Turbulent Viscosity |
| $\nu$ | Kinematic (molecular) viscosity |
| $\xi$ | Damping Factor |
| $\rho$ | Density |
| $\tau$ | Time Constant |
| $\omega$ | Specific Turbulence Energy Dissipation Rate |
| $\omega_n$ | Natural Frequency |

## Roman Symbols

| | |
|---|---|
| $a$ | Speed of Sound |
| $AR$ | Main Wing Aspect Ratio |
| $AR_{HT}$ | Horizontal Tail Aspect Ratio |
| $b$ | Span of a Lifting Surface |
| $b_W$ | Wing Span |
| $\bar{c}$ | Mean Aerodynamic Chord |
| $C_d$ | 2D Total Drag Coefficient |
| $C_D$ | 3D Total Drag Coefficient |
| $C_{d_0}$ | 2D Parasitic Drag Coefficient |
| $C_{D_0}$ | 3D Parasitic Drag Coefficient |
| $C_{D_{0_{strut}}}$ | Struts Parasitic Drag Coefficient |
| $C_{D_{0_{tires}}}$ | Tires Parasitic Drag Coefficient |
| $C_{d_{min}}$ | 2D Minimum Drag Coefficient |
| $c_f$ | Flap Chord |
| $C_f$ | 3D Viscous Drag Coefficient |
| $C_{HT}$ | Horizontal Tail Volume Coefficient |
| $C_l$ | 2D Lift Coefficient |
| $C_L$ | 3D Lift Coefficient |
| $C_{l_0}$ | 2D Lift Coefficient at Zero AoA |
| $C_{L_0}$ | 3D Lift Coefficient at Zero AoA |
| $C_{l_{max}}$ | 2D Maximum Lift Coefficient |
| $C_{L_{max}}$ | 3D Maximum Lift Coefficient |
| $C_{L_{min\ D}}$ | 2D Lift Coefficient Range for Minimum Drag |
| $C_{l_\alpha}$ | 2D Lift Curve Slope |
| $C_{L_\alpha}$ | 3D Lift Curve Slope |
| $C_{\mathcal{L}}$ | Rolling Moment Coefficient |
| $C_{\mathcal{L}_\beta}$ | Rolling Moment Derivative with Respect to Sideslip Angle |
| $C_{L_{HT}}$ | Horizontal Tail Lift Coefficient |
| $C_M$ | Pitching Moment Coefficient |

| | |
|---|---|
| $C_{M_\alpha}$ | Pitching Moment Derivative with Respect to Angle of Attack |
| $C_n$ | Yawing Moment Coefficient |
| $C_{n_\beta}$ | Yawing Moment Derivative with Respect to Sideslip Angle |
| $c_p$ | Specific Fuel Consumption |
| $c_r$ | Root Chord |
| $c_t$ | Tip Chord |
| $C_{VT}$ | Vertical Tail Volume Coefficient |
| $\bar{c}_w$ | Main Wing Mean Aerodynamic Chord |
| $D$ | Drag Force |
| $D_0$ | Parasitic Drag Force |
| $d/l$ | Fuselage Fineness Ratio |
| $D_{max}$ | Fuselage Maximum Diameter |
| $D_{trim}$ | Trim Drag |
| $e$ | Oswald Efficiency Factor |
| $e^N$ | Amplification Ratio |
| $E$ | Endurance |
| $F$ | Form Factor |
| $g$ | Acceleration of Gravity |
| $i$ | Imaginary Unit |
| $k$ | Kinetic Energy of Turbulent Fluctuations |
| $l$ | Characteristic Length |
| $L$ | Lift Force |
| $l_{HT}$ | Distance between quarter-chord locations of the mean aerodynamic chords of the main wing and horizontal tail |
| $L_{HT}$ | Horizontal Tail Lift |
| $L_s$ | Length Scale |
| $l_{VT}$ | Distance between quarter-chord locations of the mean aerodynamic chords of the main wing and vertical tail |

| | |
|---|---|
| $M$ | Mach Number |
| $MF_{Struct}$ | Structures Mass Fraction |
| $MF_{Subs}$ | Subsystems Mass Fraction |
| $MF_{Energy}$ | Energy Mass Fraction |
| $M_{tip}$ | Propeller Tip Mach Number |
| $p$ | Pressure |
| $P$ | Power |
| $q$ | Dynamic Pressure |
| $Q$ | Interference Factor |
| $q_s$ | Velocity Scale |
| $Re$ | Reynolds Number |
| $S$ | Main Wing Reference Area |
| $S_A$ | Approach Distance |
| $S_B$ | Braking Distance |
| $S_C$ | Climb Distance |
| $S_f$ | Sphere Fronta Area |
| $S_{FR}$ | Free-Roll Distance |
| $S_G$ | Ground Roll Distance |
| $S_{HT}$ | Horizontal Tail Planform Area |
| $SM$ | Static Margin |
| $S_{Panel}$ | Vertical Tail Panel Planform Area |
| $S_R$ | Rotation Distance |
| $S_{strut}$ | Strut Frontal Area |
| $S_{tires}$ | Tire Frontal Area |
| $S_{TR}$ | Transition Distance |
| $S_{VT}$ | Vertical Tail Planform Area |
| $S_{wet}$ | Wetted (Exposed) Area |
| $S_{WF}$ | Flapped Wing Area |
| $t$ | Time |
| $T$ | Thrust Force |
| $t_2$ | Time to Double Amplitude |
| $(t/c)_{max}$ | Maximum Thickness-to-Chord Ratio |

| | |
|---|---|
| $Tu$ | Turbulence Intensity |
| $u_\tau$ | Friction Velocity |
| $U^+$ | Dimensionless Velocity Profile |
| $V$ | Velocity |
| $V_s$ | Stall Speed |
| $V_{TO}$ | Take-Off Speed |
| $W$ | Weight |
| $W_{Avion}$ | Avionics Weight |
| $W_{begin}$ | Weight at the Start of Cruise |
| $W_{end}$ | Weight at the End of Cruise |
| $W_{feq}$ | Fixed Equipment Weight |
| $W_{fuel}$ | Fuel Weight |
| $W_{Other}$ | Other Fixed Equipment Weight |
| $W_{PL}$ | Payload Weight |
| $W_{Propulsion}$ | Propulsion System Weight |
| $W_{Struct}$ | Structural Weight |
| $W_{TO}$ | Maximum Take-Off Weight |
| $x_{cg}$ | Center of Gravity Location |
| $x_{np}$ | Neutral Point Location |
| $y^+$ | Dimensionless Wall Distance |
| $y^+_{target}$ | Target Dimensionless Wall Distance |
| $y_1$ | Near Wall Thickness |

## Subscripts

| | |
|---|---|
| $\partial$ | Partial Derivative |
| $x, y, z$ | Cartesian Components |

# 1 Introduction

## 1.1 Background

History proves that unmanned aircraft took to the skies long before the manned aviation advent. One of the earliest attempts is credited to chinese general Zhuge Liang (180-234) who used hot air paper balloons as military decoys. The turn of the $20^{th}$ century saw remarkable inventions such as the manned airplane, radio and mechanical autopilot that, combined with the World War I weapons demand, spurred the birth of that which is considered the first modern unmanned aircraft: the Curtis N-9 Aerial Torpedo, in 1918. The interwar years and World War II itself witnessed an increase in unmanned aviation research and development, whether in the form of target drones or weapon delivery systems.

However, it was not until the Cold War years that, galvanized by imagery and navigation technology improvements, unmanned aircraft would be employed in reconnaissance missions. During the following decades, as small-sized, lightweight digital computers, inertia navigation systems and the global positioning system (GPS) entered the technological fray, autonomous unmanned aircraft operation became truly reliable and acquired greater flexibility and accuracy. This led to its notorious and successful use in the 1982 Bekaa Valley conflict between Israeli and Syrian forces and later, during the 1991 Desert Storm operation, where employment in a wide-scale happened for the first time in history [1].

Awakened by the 9/11 terrorist attacks, the United States dramatically increased development, production and military employment of these systems. Cumulative flight hours of U.S. and Israel armed forces exceeded 100,000 by 2002. By 2011, the U.S. Army and Air Force alone surpassed 1,000,000 cumulative flight hours. Although pioneered by the United States, considerable investment in unmanned aviation has since been performed in countries like Israel, China, United Kingdom, Germany, France, Italy, Sweden, Russia, South Africa and South Korea. Due to this recent flourishing, the $21^{st}$ century has so far been dubbed the unmanned aircraft systems (UAS) golden era. However, it should be noted that the employed terminology has never been consistent, commonly varying between the latter, remotely piloted aircraft systems (RPAS) or even drones. UAS or RPAS refers to the system as a whole, comprising the aerial

vehicle, ground station, data links and remaining interfaces. Unmanned aircraft (UA) or remotely piloted aircraft (RPA) refers to the airborne platform alone [2]. For consistency, the nomenclature employed throughout the text is RPAS and RPA.

In its 2017 market profile and forecast, Teal Group Corporation estimates that RPAS production will increase from current worldwide production of 4.2 billion dollars annually to 10.3 billion dollars by 2026. Additionally, military RPAS research spending is predicted to contemplate 26 billion dollars over the same period, making this the most dynamic growth sector of the world aerospace industry [3].

Such meteoric rise of unmanned aviation is closely associated with the advantages it offers in performing certain tasks and missions when compared to manned aircraft, particularly the ones categorized as *dull*, *dirty* and *dangerous* (DDD). The first are characterized by long flight periods with little stimulation, promoting loss of human concentration and, therefore, mission effectiveness. Tasks performed in nuclear, chemical, biological or radiological contaminated areas, hazardous for the human body, are considered *dirty*. Missions conducted over hostile territories or under threatening conditions, placing human lives under harm's way, are typically defined as *dangerous*. Furthermore, covert missions, where it is of vital importance not to alert a particular entity to one's presence, research endeavours, where minimizing costs and hazards is paramount and environmentally critical tasks, where low levels of emission and noise are desirable, add to the list of missions, of military and civil nature, where employment of RPAS provides numerous benefits over their manned counterparts. A list which is completed with the economic argument since from design and production to operation and maintenance, the costs associated with RPAS are usually lower [4].

Having proven their value in both military and civil contexts over countless situations, RPAS are a must in any credible armed force. As such, the Portuguese Air Force (PAF), in the context of accomplishing strictly military national missions, other missions of public interest and international commitments as a member of the North Atlantic Treaty Organization (NATO) and the European Union (EU), recognizes the benefical impacts of inserting these systems in its operational apparatus [5].

The context of Intelligence, Surveillance and Reconnaissance (ISR) operations, fundamental for the performance of any militarized force and par excellence the application context of RPAS, may be considered a key operational domain, in which the

establishment of a national RPAS capacity may provide significant operational benefits by enhancing the flexibility of the current apparatus [6]. Considering the dimension and context of the PAF, two different, yet complementary, approaches to the incorporation of RPAS are suggested: one is through research, development and innovation (RDI) programs, the other via acquisition of complete, proven systems [5].

RDI in the field of unmanned aviation is conducted at the Air Force Academy Research Center (AFARC). Since 1996 several projects have been directed, contributing to the development of RPAS technology and creation of systems capable of demonstrating such technology [7]. In 2009, the PITVANT project spurred the execution of operational and technological activities. In the wake of its success, the AFARC began participating in several other RPAS related projects suported by external financing sources, namely the PERSEUS and SUNNY projects, in the context of maritime surveillance, and the SEAGULL project, in the domain of maritime situational awareness. By 2012, various class I platforms (maximum take-off weight, MTOW, under 150 kg) had been designed, produced and tested, exceeding a total of 250 cumulative flight hours [8].

## 1.2 Motivation

With an Exclusive Economic Zone (EEZ) of 1.656.181 km$^2$, territorial sea of 50.960 km$^2$ and inland waters comprising 13.419 km$^2$, Portugal possesses a vast maritime area, around 18.7 times the national land territory, over which sovereignty and jurisdiction are exercised. In addition, established by international commitments, a Search And Rescue (SAR) maritime area of 5.792.740 km$^2$, roughly 63 times the national territory area, is assigned to the Portuguese Republic. The strategic importance of the wide territorial waters is reinforced by the fact that 60% of all portuguese international trade, 70% of national imports and 53% of the EU international trade flows through them. A broad list of threats to the maritime environment jeopardize the exercise of national sovereignty, having negative impacts on global and national stability, the most relevant being terrorism, piracy, proliferation of weapons, narcotraffic, human trafficking, illegal immigration, degradation of maritime resources and sea pollution [9].

It is, therefore, no surprise that most of the RDI projects in which the AFARC is involved are related with the maritime environment and have the common objective of

operationalizing RPAS technology, keeping in mind its integration with the operational apparatus of the Air Force responsible for maritime surveillance and SAR missions [8].

Considering the AFARC need to pursue this line of investigation and testing of platforms and technology with possible applicability in operational contexts, a design proposal for a class I vehicle has been issued, motivating the present dissertation. Mission and performance requirements are set in order to comply with a call from the European Maritime Safety Agency (EMSA) for an RPA capable of performing maritime surveillance, SAR and pollution monitoring.

Table 1: Design proposal adapted from EMSA and provided by the AFARC.

| **Operational Requirement** | **Description** | **Observations** |
|---|---|---|
| MTOW | $<$ 150 kg | |
| Endurance | 8 hours | Full set of sensors. Longer endurance above 8 hours is a key advantage of the system |
| Range | 300 km | |
| Flight ceiling | 15 000 ft | Above mean sea level |
| Take-off and landing | Conventional | Gravel/Non-prepared |
| Take-off distance | 150 m | Ground roll and rotation |
| Landing distance | 150 m | Free-roll and braking |
| Maximum take-off altitude | 10 000 ft | Above mean sea level |
| Cruise speed | 90 kts | Full set of sensors |
| Maximum speed | 120 kts | |
| Maximum stall speed | 55 kts | Cruise configuration |
| Maximum stall speed | 45 kts | Landing configuration |
| Minimum glide ratio | 10 | |
| Minimum climb rate | 750 ft/min | At MTOW |
| Engine type | Internal combustion | Fuel injected |
| Payload | Synthetic aperture radar | |
| | Air pollution monitor | |
| | AIS receiver | |
| | Distress sensor | |
| | Pilot Cam | |
| | Gimble | EO, IR and laser |
| Avionics | Autopilot | |
| | Transponder | |
| | Satellite communications | |
| | Power supply | |
| | Onboard computation | |
| | Servo-actuators | |
| | Datalink | |

## 1.3 Objectives

The purpose of the current dissertation is to design a class I RPA, with special incidence on aerodynamics, stability, exterior design and flight performance, capable of meeting the aforementioned requirements and being manufactured with the available resources at the AFARC. Due to temporal constraints and available resources, a fully detailed and complete design is not attainable in the scope of the current academic endeavour. As such, the main objective is to perform conceptual design in its entirety and initiate preliminary design. The author clarifies the objective by dividing it into several goals:

- State-of-the-Art:
  - Review of fundamental concepts concerning the design process, flight performance, aerodynamics and the computational approach to design;
  - Assessment of contemporary RPA design best practices and market research;
- Conceptual Design:
  - RPA concept generation, selection and initial sizing;
  - Determination of the conceptual aircraft's characteristics with special emphasis on aerodynamics, stability and performance;
- Preliminary Design:
  - Establishment of a computational fluid dynamics (CFD) methodology applicable to the current design;
  - Parametric study of the main wing for maximum endurance by means of the referred CFD model;

## 1.4 Method

The design process ought to start with a review of the current state-of-the-art aircraft configurations for the particular set of requirements that have to be met. This includes understanding the industry best practices and taking a look at the aerospace market in order to identify existing aircraft that possess performance and operational characteristics similiar to the ones desired, giving the inventor greater insight into the specific challenge.

Due to its embryonic nature, conceptual design makes use of historical trends and empirical data, based on aircraft similarity, to estimate certain design parameters. A wide repository of literary works on this subject is available. Some of the most notorious in academia are the works by Thomas Corke [10] and Daniel Raymer [11]. Specifically written for RPA design are the texts by authors Jay Gundlach [2] and Reg Austin [4]. It is the author's decision to follow Corke's spreadsheet approach for conceptual design, complemented with information from Raymer and Gundlach's texts, in order to augment its reliability.

Supplementing the referred method, XFLR5 v6.33 flow analysis are conducted in order to provide additional results and therefore enhance the initial spreadsheet estimates, particularly in the fields of aerodynamics and stability, the main focus of the current text. XFLR5 is a computational tool, based on XFOIL, Lifting Line Theory (LLT), Vortex Lattice Method (VLM) and Panel Method (PM), that is frequently used in the aerospace community as an auxiliary design tool. It provides fast calculations with a fine balance between precision and computational requirements [29].

As the design matures and enters the preliminary phase, a more computationally demanding, complex and reliable tool, such as Star-CCM+ v.8.04, is used. This CFD software is an extremely powerful design instrument, able to supply the designer with detailed characterization of the flow over the aircraft's components, capturing the vast majority of flow phenomena [28]. It assumes particular relevance when refining and detailing the RPA design.

## 1.5 Layout

The present dissertation is structured in the following way: chapter 1 comprises an historical and situational background of RPAS, followed by a motivation for the project under development, indentification of its objectives, a brief description of the methods used in achieving the latter and an outline of the full document.

Chapter 2 adresses a set of fundamental concepts regarding the design process, flight performance and aerodynamics, followed by a detailed discussion on the theoretical basis of the computational approach, its potentialities and limitations. It also describes the state-of-the-art of RPA design, culminating in a market research report.

In chapter 3 an extensive debate over conceptual design is performed, from the early concept generation process to the final flight performance calculation. The line of thought in building up the airplane is properly explained as well as the employment of spreadsheets and complementing XFLR5 simulations.

Preliminary design is initiated in chapter 4 as CFD tools enter the design environment. Establishment of a robust, applicable CFD methodology is conducted, in accordance with the community best practices. Once defined, the CFD model is used in a parametric study of the main wing for maximum endurance.

A general overview of the project is done in chapter 5, as well as an array of pertinent conclusions. Finishing the dissertation, recommendations for future works and further developments necessary to accomplish the ultimate goal of producing a class I RPA are drawn.

# 2 Fundamental Concepts & State-of-the-Art

## 2.1 The Design Process

### 2.1.1 Design Method

Design is defined as “the process of planning the physical characteristics and construction methods of a product” [12]. In the process of inventing a product, design is the most important phase, where the individual responsible for it – the designer – attempts to meet a set of established requirements while making the best use of resources and projecting an efficient construction process.

Based on the scientific method, the design process can be interpreted as a group of five steps, starting from the problem definition, followed by data collection, creation of design concepts, analysis of their performance and, ultimately, decision making which is based on the results obtained. This is a highly iterative procedure since the results will often fail to meet the objectives, forcing the designer to return to the initial steps and perform suitable changes.

Refinement is also a source of iteration and is performed in order to make the best possible design, i.e., one that is optimized to its full potential and enables the creation of a true superior product. It is frequent, however, to determine that one of the original requirements is unreasonable or two of them conflict with each other. In this situation, a redefinition of the customer’s demands is conducted [12].

According to Nicolai [13], the design process requires three main actions: synthesis, analysis and decision making. The first is characterized by a relatively unstructured, often intuitive creative thinking whilst the remaining two are marked by their highly structured and methodical thinking. In order to succeed, designers must master both types of thought processes which is a challenging task due to their sharp dissimilarity.

### 2.1.2 Aircraft Design

An aircraft design is initiated because customers such as airlines, corporations, private pilots, government agencies or military services, have needs. These are usually specified as one or more design missions that the aircraft must be able to accomplish and a set of constraints or performance requirements that have to be met and are formally

described in a design proposal (DP). The most important requirements to meet – design drivers – have the strongest influence on the configuration and characteristics of the aircraft and must be clearly identified [12]. The process is broken into three major phases: conceptual, preliminary and detailed design.

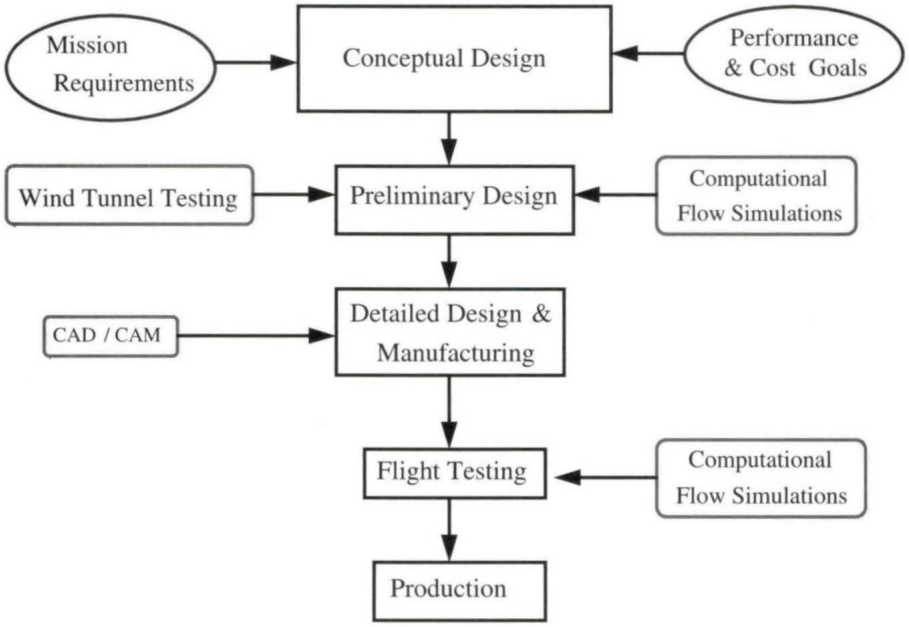


Figure 1: Aircraft development process. Adapted from [12].

Conceptual design answers the basic questions of configuration arrangement, size, weight and performance. It involves estimation of weights, choice of aerodynamic characteristics that best suit the mission specifications, total drag predictions, power plant sizing, determination of the best airframe to accommodate the payload and main components, location of principle weight groups, estimates of static stability behaviour, sizing of control surfaces and predictions of flight performance [10]. All this is done in a very fluid process where new ideas and problems are constantly emerging as the design matures and is further investigated in increasing detail [11]. Continuous iteration compels the designer to keep a keen eye on the influence of minor changes on the general picture and keep the design updated. Once a conceptual aircraft, capable of fulfilling the mission requirements, is designed, one may move on to next phase.

When the major changes are over, preliminary design begins. In this phase, minor revisions may happen but the configuration arrangement is expected to be fixed and remain constant. Specialists in areas such as aerodynamics, propulsion, struc-

tures and stability and control will design, analyse and test specific components of the airplane [11]. A fine tuning of the conceptual design is made through computational simulations and wind tunnel tests that allow for the prediction of intricate aspects such as the structural and aerodynamic interaction between the wing, fuselage and tail surfaces. A more detailed analysis of aerodynamic loads and component weights is also performed, leading to a refinement in the structural design [10]. At the completion of this phase, the design is *frozen* and a comprehensive definition of the complete system with its interfaces is elaborated.

The detailed design phase comprises the design of the actual pieces to be fabricated and a plan of the airplane manufacturing process, starting with the smallest and simplest subassemblies and building up to the final assembly. Computer-aided design (CAD) tools are extremely useful at providing realistic three-dimensional (3D) views of the interior layout. At this point, testing effort intensifies as major items and structural components are built and tested. A detailed structural design of the aircraft, containing every detail needed for its construction, is the final output of this phase [10], [11].

Typically, after conclusion of detailed design, a prototype is produced and flight testing initiates [10]. The need for subsequent modifications may arise due to flaws identified during this period. Once testing is successfully accomplished and airworthiness and certification issues are dealt with, the aircraft enters operation. While in service, several improvements might be conducted, leading to new versions of the product. All changes performed since the initial manufacture are considered part of the design process [4].

An airplane design brings different areas of aerospace engineering together, such as aerodynamics, propulsion, structural mechanics, stability and control. Each of these areas is paramount and involves parameters that govern the size, shape, weight and performance of the aircraft. Ideally, a designer seeks to optimize all these aspects, however, such is practically impossible since optimizing one characteristic usually degrades others. For this reason, compromise is often the nature of aircraft design, i.e., obtaining a balance between the different aspects of the total performance while attempting to optimize one or more, based on clearly identified mission requirements, is the objective [10].

Generally, the parameter which exerts the biggest influence on the design of a RPA

is the payload. Its size, mass and electrical power requirements are crucial in determining the layout, dimensions and MTOW of the aircraft. Other parameters can be just as important as the payload, namely endurance, range, speed range and launch and recovery specifications [4].

### 2.1.3 Conceptual Design Approach

The first task of the designer is to read and fully comprehend the design proposal. This implies understanding three distinct ideas: the motivation for the design, i.e., the aircraft's purpose or mission, the *technology readiness* of new technology for incorporation into the design, and the specific set of design requirements that comprises performance parameters (e.g., range, take-off and landing distances and speed requirements), but also a vast set of civil or military design specifications which must be met (e.g., stall speed and structural design limits) [10], [11].

Conceptual design usually starts with various conceptual sketchs of different configurations. Such drawings include the approximate wing and tail geometries, the fuselage shape and the locations of major components such as engines, payload compartment, landing gear and fuel tanks. They are used to predict aerodynamics and weight fractions by comparison to historical data and, in turn, produce initial estimates of the required total and fuel weight. This first-order sizing is complemented by actual aerodynamics, weights, propulsion and stability information, leading to a detailed sizing calculation. The performance capabilities of the design are calculated and compared to the requirements. Refinement follows in order to obtain better estimates of different parameters which lead to revisions in various areas of design. The refined results frequently demand changes in the design layout. After some iterations, the revised conceptual aircraft is expected to meet the full requirements and confidently transit to the preliminary design phase [11].

Corke [10] suggests an intuitive and methodic approach to the process of conceptual design which consists in breaking it down into 14 steps and developing it in a step-by-step fashion. This strategy focus on the implementation of spreadsheets for iterative and repetitive calculations. Using these, the effect of different input parameters may be easily investigated and optimums can be sought. Reference aircraft are used in order to check various design elements and determine if they deviate too far from

expected tendencies. Other authors, such as Raymer [11] and Sadraey [14], present their own strategies for tackling conceptual design. Although not as intuitive as the former, they may prove useful in providing complementary data which enhances the design.

Any of the previous approaches draws on historical information to provide necessary input parameters, particularly at early stages of the design process, when there is a considerable lack of knowledge regarding the product to be built. In the field of manned aviation, the need for empirical information poses no problem as an extensive documentation inventory (e.g., [10], [11], [14]) is available . Regarding unmanned aviation, the same cannot be said as literature on this topic is significantly sparser. Alerted to this handicap, some authors such as Jay Gundlach [2] and Reg Austin [4] have developed concise RPA design texts, in an attempt to bridge the gap and provide an empirical database of RPA information.

## 2.2 Performance & Aerodynamics

The present dissertation deals with the process of aircraft design with special emphasis on aerodynamics and flight performance. In light of this, a brief discussion on the basic concepts of both topics is in order.

### 2.2.1 Performance

Flight performance is a wide subject that covers various flight conditions. Of particular relevance to the current dissertation are steady level flight, steady climbing and descending flight, level turning flight, gliding flight and take-off and landing. Although all the referred conditions are analysed in later chapters, a discussion on their theoretical basis would be tedious, unnecessary and out of this text's scope. However, by investigating the design proposal, one is able to understand that steady level flight is undoubtedly the mission's core and endurance is one, if not *the*, main design driver of the project. For this reasons, a brief introduction to the concept of endurance and its maximization for level flight is of key importance.

Endurance is defined as the maximum time an aircraft can continue flying under given conditions without refuelling [15]. The Breguet equation, for propeller driven

airplanes, expresses it in the following manner [16]:

$$E = \int_{W_{begin}}^{W_{end}} \frac{\eta_p}{c_p g} \frac{dW}{DV} = \frac{\eta_p}{c_p g} \frac{C_L^{3/2}}{C_D} \sqrt{2\rho S} \left( \frac{1}{\sqrt{W_{end}}} - \frac{1}{\sqrt{W_{begin}}} \right) \tag{1}$$

In equation 1, $E$ represents endurance, $\eta_p$ is the installed propeller efficiency, $c_p$ the specific fuel consumption, $g$ the acceleration of gravity, $C_L$ and $C_D$ are the total aircraft lift and drag coefficients, $\rho$ the air density, $S$ the main wing reference area and $W_{end}$ and $W_{begin}$ represent the weight of the airplane at the end and start of cruise, respectively. Additionally, $D$ and $V$ represent the total drag and speed in level flight, respectively.

The resulting Breguet equation is a closed form solution of the preceding integral, i.e., it is merely an approximation and not an exact solution. This is due to the fact that the integration is carried out assuming constant altitude, propeller efficiency, specific fuel consumption and lift and drag coefficients. Such might not always be the case, especially for very long endurances (longer than 3 hours) in which the former parametres vary during the flight. To improve accuracy, equation 1 can be numerically integrated, i.e., solved for a number of endurance segments, re-evaluating the time-changing parameters at each new segment [16]. Nevertheless, the closed form solution stresses the influence of several parameters on endurance and is widely used for conceptual design purposes [2], [10], [11].

When flying at a given altitude, best endurance occurs when the combined parameter $(\eta_p/c_p g)(C_L^{3/2}/C_D)$ is maximized [16]. The first term depends heavily on the propulsive system's characteristics but the second is determined by the aerodynamic coefficients of lift and drag. It is clear that, keeping all remaining factors constant, increasing lift and decreasing drag results in an endurance increment. For steady level flight, lift is determined by the need to balance the weight, as expressed in equation 2, in which $L$ and $W$ represent the total lift and weight, respectively [10].

$$L = W = \frac{1}{2}\rho V^2 S C_L \tag{2}$$

At cruise conditions (constant velocity), increasing the lift coefficient results in a vertical acceleration that drives the aircraft upwards, gaining altitude, which may not be desired [10]. Decreasing drag does not cause any undesired effect during steady level flight, on the contrary, it reduces the power required from the propulsive system.

Therefore, for a prescribed cruise velocity, minimizing drag is a possible measure for maximizing endurance.

### 2.2.2 Viscous Flow

Prior to the definition and scrutiny of drag, as well as a discussion on the topic of drag reduction techniques, a review on the fundamentals of viscous flow is presented.

Aircraft flight regime is characterized by two important dimensionless parameters: Mach number and Reynolds number [2]. Mach number is defined as the ratio of the flow velocity to the speed of sound (freestream values are commonly used).

$$M = \frac{V}{a} \tag{3}$$

For a calorically perfect gas, as air is typically considered, speed of sound is a function of temperature alone. Below Mach numbers of approximately 0.3, the air density is constant and the airflow is said to be incompressible [17].

By far the most important dimensionless parameter, the Reynolds number represents the ratio of the inertia to the viscous forces acting on the fluid.

$$Re = \frac{\rho V l}{\mu} \tag{4}$$

In equation 4, $\rho$ and $\mu$ are the air density and dynamic viscosity, respectively, $V$ is the freestream velocity and $l$ a characteristic length. For flows over airfoils and wings, the mean aerodynamic chord is generally chosen. If $Re$ is large, the inertia forces overshadow the viscous ones and vice versa [18]. Depending on the application, typical Reynolds numbers of RPAs vary between $3 \times 10^4$ and $2 \times 10^7$ [2]. An important regime is the Low Reynolds Number (LRN), which occurs below $5 \times 10^5$ [19].

As the Reynolds number suggests, viscosity plays a major role in determining the behaviour of the flow. In fact, the distinguishing feature of the flow of a viscous fluid (e.g., air) around a body (e.g., wing) is the fact that at the fluid-solid interface there is no relative motion between the two. Due to the effect of viscosity, a no-slip condition occurs at a solid surface. This boundary condition states that, at the wall, the total velocity is reduced to zero.

The influence of the no-slip condition on the flow decreases as the distance from the

surface increases, until it vanishes. The region adjacent to the body in which the effects of viscosity are concentrated is termed the boundary layer. In aeronautical applications, the boundary layer formed over an airfoil varies from practically zero thickness near the leading edge to a few percent of the chord at the trailing edge.

Inside the boundary layer, a consequence of viscosity is the appearance of shearing stresses. At the wall, the shearing stress exercised by the fluid on the surface, in the tangential direction – skin-friction – is the source of frictional drag, a crucial parameter in the design of airplanes [18].

The vast majority of RPAs operates at Reynolds numbers above $2 \times 10^5$, with the exception of Micro Air Vehicles (MAVs) and small RPAs [2]. In these conditions, the boundary layer structure is generally divided into three regions: laminar, transition and turbulent [18].

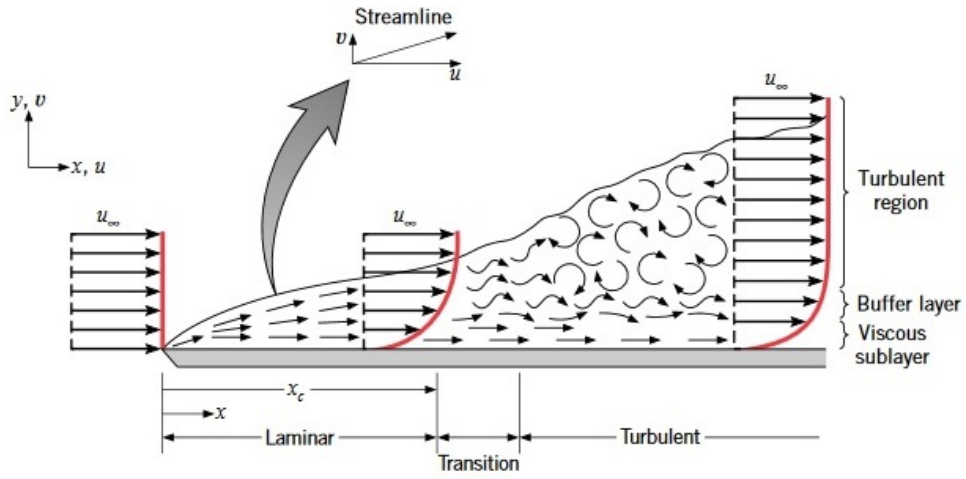


Figure 2: Boundary layer development over a flat plate. Adapted from [20].

The laminar portion of the flow is marked by a highly ordered motion [20]. Laminar boundary layers are especially susceptible to flow separation in the presence of adverse pressure gradients. Downstream of the separation point, the streamlines may deflect towards the surface, forming a turbulent boundary layer, or deflect farther away, forming a highly unsteady wake. In either situation a significant increase in drag occurs.

Transition from laminar to turbulent flow can be triggered by three distinct mechanisms. The most common in aeronautical applications is natural transition, in which small disturbances typically caused by surface roughness or pressure pulses tend to grow with time and generate high frequency fluctuations – Tollmien-Schlichting (TS) instability [18]. The remaining two include bypass transition, which is caused by high

levels of turbulence in the freestream [21], and separation induced transition, in which separation of the laminar boundary layer triggers transition [18].

Special attention is drawn to the latter. Such phenomenon occurs at Reynolds numbers greater than $5 \times 10^4$, provided the adverse pressure gradient is not too intense, allowing for the flow to recover sufficient energy through entrainment to reattach to the surface, forming, on a time-averaged basis, a region of recirculating flow denominated transitional separation bubble (TSB) or laminar separation bubble (LSB). Although predominant in the LRN regime, TSBs can also appear at $Re > 5 \times 10^5$ and play a key role in airfoil stall behaviour [19].

Turbulent boundary layers are marked by a random and irregular nature of the flow, governed by chaotic fluctuations over an average flow field. Essentially three-dimensional, turbulent flow comprises ensembles of eddies of different dimensions whose motions and interactions generate circular, twisted trajectories. In turbulent boundary layers, that occur only at large Reynolds numbers, frictional drag increases significantly in comparison to laminar boundary layers, resulting in a deterioration of aircraft aerodynamic performance [22].

### 2.2.3 Drag

Drag is defined by the Cambridge Aerospace Dictionary [15] as “retarding force acting upon body in relative motion through fluid, parallel to direction of motion”. Basic drag nomenclature varies throughout the literature, which can be confusing, jeopardizing clarity and coherence in technical discussions [23]. The nomenclature presented here is derived from several authors [2], [23] - [27], in an attempt to capture all important aspects and definitions.

It is common to divide the airplane total drag in two components: parasite and induced [25]. The former is typically defined as the drag that is produced without any connection to the generation of lift, hence the term *parasitic* as it represents a waste of fuel [24]. It can be interpreted as the sum of all drag components from all non-lifting parts of the aircraft [15].

Parasite drag comprises the profile and interference drag. Profile drag can be divided into three components: skin-friction, form and lift-related profile drag. The latter is generally significantly small and therefore neglected [25]. As stated in 2.2.2, skin-

friction drag is generated by the shear stress acting on a solid surface as a result of viscosity. Form drag is a consequence of the pressure distribution around a body immersed in viscous flow. In the presence of boundary layer separation, this drag component is exacerbated [26]. Interference drag arises from the intersection of different bodies and when two or more bodies are placed one behind the other or near each other without actually touching [24].

Induced drag is associated with the generation of lift. Due to the effect of the downwash angle, caused by the lifting surface's vortex system, the lift force is inclined backwards from the vertical, resulting in a component parallel to the undisturbed stream – induced drag [26]. This component often contributes about half of the entire aircraft drag [25]. Trim drag can be included in the overall induced drag [2].

At airspeeds higher than the critical Mach number, shock waves and other compressibility effects introduce a new component – wave drag [25] – that provides contributions to both parasite and induced drag components [23]. For low subsonic conditions wave drag is inexistent, therefore its discussion is not relevant in the scope of the present text.

Drag is often expressed in terms of a dimensionless drag coefficient, formulated in equation 5, where $D$ represents the total drag, $\rho$ the air density, $V$ the freestream velocity and $S$ a reference area (typically the wing area) [11].

$$C_D = \frac{D}{\frac{1}{2}\rho V^2 S} \tag{5}$$

Assuming a parabolic relationship between both drag and lift coefficients, the former may be split in two terms, representing parasite and induced drag, respectively [2].

$$C_D = C_{D_0} + KC_L^2 = C_{D_0} + \frac{C_L^2}{\pi \cdot AR \cdot e} \tag{6}$$

Investigation of equation 6 reveals a strong dependency of the induced drag coefficient on the aircraft aspect ratio, $AR$, and Oswald efficiency factor, $e$.

### 2.2.4 Drag Reduction Techniques

The main contribution for parasite drag comes from its skin-friction component. Two methods are generally considered to achieve a reduction of the latter: reducing turbu-

lent skin-friction and delaying transition in order to extend the laminar portion of the flow. Their description is outside the scope of the present text, however, the author points out the wide use of devices like riblets and large eddy break-up devices (LEBUs) in the reduction of turbulent skin-friction. Shaping the airfoil and reducing surface roughness are the most simple measures employed in laminar flow control [23].

As equation 6 suggests, increasing both Oswald efficiency factor and aspect ratio leads to a reduction in induced drag. Aspect ratio cannot be excessively increased as it leads to structural and weight penalties. Hence, a compromise between aerodynamic and structural performance must be established [23]. The Oswald efficiency factor accounts for the deviation of the actual lift distribution from the ideal elliptic one, therefore, the key concept is to approximate the lift distribution to that of an elliptic. This is typically accomplished by tapering or twisting the wing [11].

An alternative and widely employed technique for reducing induced drag is the development of wing-tip devices such as endplates and winglets. This solution focuses on reducing the effects of wing-tip vortices, which are the main source of induced drag [23].

## 2.3 XFLR5

Due to their semi-empirical nature, conceptual design estimates, particularly in the fields of aerodynamics and stability, may benefit from being complemented with information obtained from computational analyses performed by simple numerical tools with reasonable reliability. XFLR5 presents itself as one of such tools, offering the possibility of conducting aerodynamic and stability studies of simple 2D and 3D geometries at subsonic conditions with an adequate trade-off between accuracy and computational and temporal efforts. Although limited in scope, it is widely employed throughout the aerospace community as an auxiliary design tool [28], [29].

The XFOIL code is the foundation of XFLR5 2D analyses whereas its 3D simulations are based on LLT, VLM and PM. In the context of the present work, due to software constraints and standardization of all lifting surfaces analyses, it is the author's decision to perform only VLM simulations.

### 2.3.1 XFOIL

Initially written by Mark Drela in 1986, XFOIL has since then undergone several upgrades and enhancements, giving it the status of a modern, interactive program for the design and analysis of subsonic isolated airfoils [29]. Its theoretical model is mainly characterized by an inviscid linear-vorticity streamfunction formulation which incorporates viscous displacement effects, therefore coupling inviscid and viscous flow.

The airfoil outline and wake trajectory are discretized into flat panels. Knowledge of the geometry of the problem, i.e., of all airfoil and wake panel nodes, together with the imposition of a constant value for the streamfunction at any airfoil node and a Kutta condition at the airfoil trailing edge, yields a linear system of equations for all node values. Specifying an angle of attack (AoA) provides an inviscid solution.

The viscous formulation employs different sets of boundary layer governing equations, depending on whether the flow regime is laminar or turbulent. These equations are discretized using two-point central differences with their fundamental variables defined to be located at the panel nodes. By coupling the resulting system of equations with the inviscid formulation, a viscous solution is obtained.

The viscous/inviscid solution scheme is a distinguishing feature of the XFOIL method, allowing the solution algorithm to properly handle the very strong and nonlinear coupling between the viscous, transition and inviscid formulations that are exceptionally important at transitional separation bubbles, capturing the complex physics of such phenomena. The ability to represent all important physical mechanisms that affect airfoil performance (viz., instability, separation, bubble losses) while demanding modest computational requirements, attests the relevance of the present computational model for initial conceptual aircraft design [30].

Before moving on to the VLM, a remark on transition criteria is in order. XFLR5 uses the $e^N$ method to predict boundary layer transition. Based on linear stability theory, it is regarded as a reliable method for the prediction of laminar to turbulent transition for two-dimensional flows, with relevant application in the study and design of airfoils [33].

A range of $N$ values defines the transition region. Data obtained from flat plate experiments sets this range as 7.8-10 [33]. In the specific case of flows over airfoils, the transition region is in practice a transition point defined by an amplification factor of 9, according to experimental data [34]. In fact, the value $N = 9$ is considered universally

valid for airfoil applications [33].

### 2.3.2 Vortex Lattice Method

The VLM is a numerical method widely employed in the study of 3D lifting geometries. Its formulation is based on the theoretical model of a system of vortices that impart the surrounding air a motion similar to the actual flow over a wing and sustain a force equivalent to the wing lift known to be generated. Such system – vortex ring – is divided into three main parts: the starting vortex, the trailing vortex system and the bound vortex system. The starting vortex, however, soon falls behind and the pair of trailing vortices stretches effectively to infinity as steady flight proceeds, resulting in a horseshoe vortex, a three-sided vortex made up by the bound and trailing vortices [26].

The wing is represented as a surface discretized in a finite number of trapezoidal panels. By associating a horseshoe vortex to each panel, a grid of horseshoe vortices is superimposed on the wing, approximating the continuous distribution of bound vorticity over its surface. This situation is illustrated in figure 3.

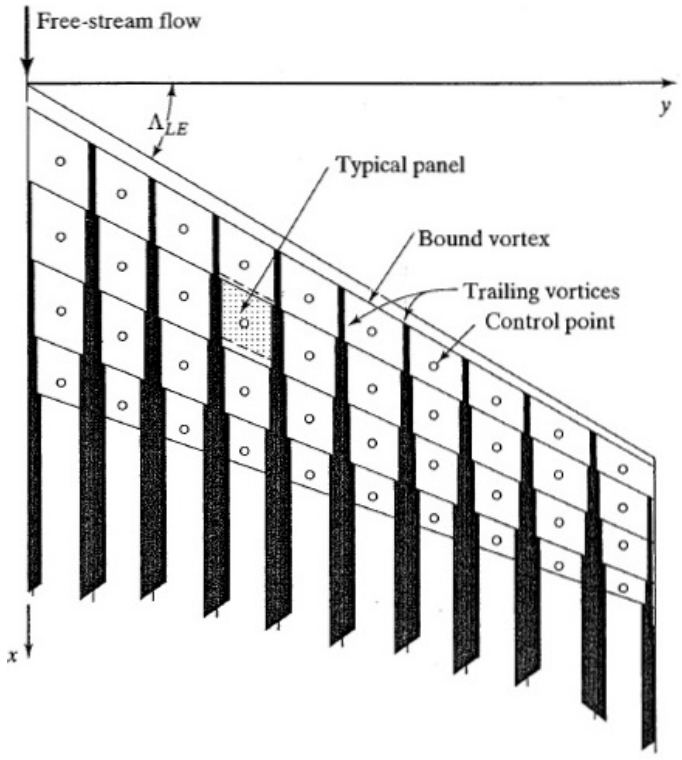


Figure 3: Representation of elemental panels and horseshoe vortices for a typical wing planform in the Vortex Lattice Method. Adapted from [31].

The velocity induced by a vortex filament at a control point of a given panel is given

by the law of Biot and Savart. For a horseshoe vortex, the effect of each segment is calculated separately and added to the remainder. The total induced velocity at the referred point is obtained by considering the effect of all vortices superimposed on the wing. A system of linear equations, one for each panel, is thus created.

Knowledge of the wing geometry, combined with the boundary condition that the flow is tangent to the wing at any point, provides a solution to the linear system of equations, yielding the induced velocities at each control point. Consequently, the pressure differencial between the upper and lower wing surfaces is determined. When integrated, it yields the total forces and moments acting upon the wing [31].

An alternative formulation of the VLM, present in XFLR5 v6.33, is one where the vortex system is modeled as a vortex ring instead of a horseshoe vortex. In this situation, a grid of ring vortices is superimposed on the wing and the induced velocity at a control point depends on the contributions of all four segments, i.e., bound vortex, trailing vortices and starting vortex. The remainder of the formulation is identical [32].

The vortex lattice method offers the ability to evaluate a vast range of lifting surface geometries, including wings with sweep, dihedral and low aspect ratios. Configurations with multiple surfaces can be analysed simultaneously, fully capturing all interactions such as the downwash effect of the main wing on the aft tail. In addition, VLM is able to predict not just lift and drag distributions but also aerodynamic derivatives of vital importance for stability and control analysis, making it a suitable method for conceptual design software implementation [2].

## 2.4 Computational Fluid Dynamics

Proper understanding of aerodynamic phenomena is mandatory when aiming at credible and successful aircraft designs. The governing fluid dynamics equations that characterize such phenomena are approached in three different, yet complementary, ways: theory, experiment and computational fluid dynamics. By 1995, due to advances in storage and speed capacity of modern digital computers, CFD three-dimensional flow field solutions were already plentiful and becoming increasingly prevalent in the aerospace industry, performing a strong role as aircraft design tools [35]. The turn of the century consolidated this idea, making CFD the industrial standard tool for solving fluid flow engineering problems and therefore constituting a reliable instrument for

aircraft design and aerodynamic analysis [36].

The following discussion on CFD intends to highlight basic concepts and summarize the current aerospace community best practices for external aerodynamics applications, adopted in the Star-CCM+ analysis conducted during preliminary design. In the context of the present dissertation, CFD is merely used as a design tool and does not represent its core subject. Therefore, an extensive review of its concepts and state-of-the-art is not in the scope of this work. The author's purpose is simply to provide insight into what is done and why it is done in such way regarding the preliminary design CFD analysis.

### 2.4.1 Approximation Models

CFD transforms a physical continuum and its integral/differential governing fluid dynamics equations into a discretized computational domain governed by a system of algebraic equations. Three methods exist to engage the referred discretization: the Finite Difference Method (FDM), Finite Element Method (FEM) and Finite Volume Method (FVM). The first, despite its traditional and referential aspects, is limited in scope to structured grids. The second, highly dominant in the world of structural mechanics, is seldomly employed in CFD. The third, FVM, is by far the most widely applied method in CFD (including the analysis software Star-CCM+). Characterized by its generality, conceptual simplicity and relative ease of application to both structured and unstructured grids, it is sustained by a large extent of literary works [37]. Hence, the following discussion is devoted to the Finite Volume Method.

The basic equations of fluid mechanics, known as the system of Navier-Stokes equations, express the conservation of the fundamental quantities – mass, momentum and energy – through a system of five fully coupled time-dependent partial differential and nonlinear equations that are inherently and intricately complex. A consequence of the nonlinearity of the flow equations is the appearance of turbulence, a spontaneous instability of the flow, responsible for the statistical behaviour of all flow quantities. These can be interpreted as fluctuations superimposed on mean or averaged values that can often attain 10% of the former, although flow regions such as separation zones may achieve considerably higher levels of turbulent fluctuations.

Due to their statistical nature, turbulent flows cannot be described in a deterministic

way. Nonetheless, the turbulent fluctuations can be computed numerically, allowing a numerical description of turbulent flows by the direct numerical simulation (DNS) approach. Its objective is to simulate on computer the whole range of turbulent statistical fluctuations at all relevant physical scales. Clearly, such is a formidable task, demading extremely high performance of computer resources which is out of reach, in the foreseeable future, for industrial applications, at least in acceptable computer central processing unit (CPU) times.

The engineering solution for this problem is the employment of approximation models that reduce the complexity of turbulent flows, yet still account for its effects. Two families of models are presently available. The first – Large Eddy Simulation (LES) – is the highest approximation, computing directly the turbulent fluctuations in space and time (similar to DNS). However, this is only accomplished above a certain length scale, named the subgrid scale, below which turbulence is modeled by semi-empirical laws. The second highest approximation model – Reynolds Averaged Navier-Stokes (RANS) – is currently the most widely applied in the CFD community and the focus of the current discussion. In this approach, turbulence is averaged out, in time, over the entire spectrum of turbulent fluctuations, requiring empirical or semi-empirical information on the turbulence structure and its relation to the averaged flow [37].

Any variable can be written as the sum of a time-averaged value (steady flows) or an ensemble-averaged value (unsteady flows) and a fluctuation about that value. By formulating the governing equations in terms of the averaged flow field quantities, the RANS model eliminates all turbulence fluctuations. However, inspection of the averaged momentum equation (for incompressible flow and no body forces), equation 7 [38], unveals a term that cannot be represented uniquely in terms of the mean quantities.

$$\frac{\partial(\rho\bar{u_i})}{\partial t} + \frac{\partial}{\partial x_j}(\rho\bar{u_i}\bar{u_j} + \rho\overline{u_i'u_j'}) = -\frac{\partial\bar{p}}{\partial x_i} + \frac{\partial}{\partial x_j}\left[\mu\left(\frac{\partial\bar{u_i}}{\partial x_j} + \frac{\partial\bar{u_j}}{\partial x_i}\right)\right] \tag{7}$$

The term $\rho\overline{u_i'u_j'}$, dubbed the Reynolds stress tensor, prevents the system of equations from being a closed system, i.e., the number of variables exceeds the number of equations, since the relations between these and the mean flow quantities are unknown. In order to close the system, an approximation – turbulence model – which prescribes the Reynolds stress tensor in terms of the mean quantities has to be used

[38].

Following the RANS concept, all turbulence is modeled and the computational effort is placed on determining the mean flow quantities, discarding any attempt to resolve turbulent structures in time and space. This significantly reduced complexity of turbulent flow simulation associated with the RANS model allows it, if selected and applied properly, to provide a very interesting balance between computational resources and accuracy required for most industrial applications. Nevertheless, one should always keep in mind that the RANS model is an approximation of reality and has to bridge many orders of magnitude in computing power, with the consequence of not always producing results with a narrow error margin [39].

### 2.4.2 Turbulence Models

Three main families of turbulence models exist: Linear Eddy Viscosity Models (LEVM), Reynolds Stress Transport Models (RSTM) (or Second Closure Models (SCM)) and Non-Linear Eddy Viscosity Models (NLEVM).

The first dates back to 1877 when Joseph Boussinesq introduced the concept of an eddy viscosity or dynamic turbulent viscosity, $\mu_t$, which relates the Reynolds stresses to the averaged velocity gradients. When carefully applied, LEVM provides reasonably good results for many flows.

RSTM or SCM were initially devised in the 1950's by Julius Rotta who laid the foundation for turbulence models that discarded the turbulent viscosity concept by introducing a model for the differential equation governing the evolution of the Reynolds stress tensor, allowing a direct determination of the turbulent stresses by solving a transport equation for each stress component. For 3D flows, seven equations have to be solved, six coupled equations for each Reynolds stress tensor component and one for the turbulent length scale. RSTM provides advantages such as naturally accounting for non-local and history flow effects, making the referred model suitable for computing complicating effects such as streamline curvature or rigid body rotation. However, the large number of equations and complexity involved increases the computational effort and balances the former benefits [40].

NLEVM has a theoretical foundation similar to LEVM, algebraically relating the turbulent stresses to the averaged velocity gradients. The difference lies in the use of

higher order quadratic and cubic terms featuring additional coefficients. Although not strongly established as its linear counterpart, NLEVM is computationally efficient and may provide greater accuracy in predicting turbulent flow phenomena [36].

LEVM is the dominant approach in industrial CFD applications, therefore, special emphasis is put in reviewing its formulations. These come in the form of zero-equation (algebraic), one-equation or two-equation models, which are distinguished by how they determine the velocity scale, $q_s$, and length scale, $L_s$, that characterize turbulence.

The zero-equation model, or mixing-length model, is the simplest. The velocity and length scales are related to the local flow properties via algebraic equations where $L_s$ is a prescribed function of the coordinates and $q_s$ is directly proportional to $L_s$ and to the local velocity gradients. However, accurate prescription of $L_s$ is only possible for simple flows, leaving separated or highly three-dimensional flows out of the model's range of applicability. Therefore, the zero-equation model is limited to relatively simple flows and its employment in RANS applications is discouraged [38].

One-equation models are an improvement over the former. By using an additional differential transport equation that relates $q_s$ with the kinetic energy of the turbulent fluctuations, $k$, flow history is taken into account, improving the model's mathematical description of the turbulent stresses and, consequently, its ability to predict the properties of turbulent flows. The length scale prescription follows the same approach as in the algebraic model, with the same limitations. One-equation models are the least popular and successful with the Spalart-Allmaras being, perhaps, the most notorious. These models are considered incomplete due to the need for a turbulent length scale specification which requires prior knowledge of the flow, other than initial and boundary conditions, in order to obtain a solution.

Two-equation models are the most widely employed in CFD industrial applications, making use of two differential transport equations to determine the velocity and length scales. The formerly referred equation for $k$ determines $q_s$ and an additional equation is introduced in order to compute $L_s$. These are complete models since they do not require prior knowledge of any flow details in order to obtain a solution. The equation used in computing the length scale defines the particular two-equation model [40].

Initially developed by Peter Chou in 1945 and made famous by Jones and Launder in their 1972 paper, the $k-\epsilon$ model uses a differential transport equation that relates

the dissipation rate of turbulence energy, $\epsilon$, to the length scale $L_s$ [40]. The most popular of all two-equation models, it adequately predicts near-wall and free-shear-flow phenomena and successfully accounts for low Reynolds number features of turbulence, accuratelly predicting recirculating and boundary layer flows with low sensitivity to free stream values. However, due to limitations in the modeling of the flow in near-wall regions, such as the effect of steep property variation, the model becomes inadequate in the presence of adverse pressure gradients, and typically misses or underpredicts flow separation [41], a handicap in the simulation of airfoil and wing flows.

The second most popular two-equation model was proposed by Andrey Kolmogrov in 1942 and continuously improved over the course of the years, its most notorious formulation elaborated by David Wilcox. The $k-\omega$ model relates the dissipation rate of turbulence energy in unit volume and time, i.e., the specific turbulence energy dissipation rate, $\omega$, to the length scale $L_s$ via a differential transport equation [40]. By performing exceptionally well close to walls in boundary layer flows, particularly under adverse pressure gradients, the $k-\omega$ model eliminates some of the $k-\epsilon$ model's shortcomings. However, detailed investigations [42] concluded that the magnitude of the eddy viscosity can be changed by more than 100% if different freestream values of $\omega$ are specified, revealing a strong sensitivity of the model to freestream values, a non-existent handicap of the previous one [43].

The merit of combining the best of both worlds belongs to Florian Menter, who, in 1993, proposed the Baseline (BSL) and Shear-Stress Transport (SST) models. The BSL model is identical to Wilcox's $k-\omega$ model in the inner half of the boundary layer and gradually changes to the standard $k-\epsilon$ model towards the boundary layer edge, keeping the properties and excellent performance of the former close to walls and the latter's low sensitivity to freestream values. The SST model is an improvement over the BSL. It performs in a similar fashion with the additional capacity to account for the transport of the principal turbulent shear stress in adverse pressure gradient boundary layers, based on the assumption that the principal shear stress is proportional to the turbulent kinetic energy. Both models were tested for a large number of meaningful flowfields for aerodynamic applications and provided results in agreement with the accurate modeling of near-wall flow and no freestream dependence, with the SST excelling its predecessor by showing better agreement with experimental data for adverse

pressure gradient boundary layer flows [43].

### 2.4.3 Transition Models

A considerable segment of industrial flows is characterized by Reynolds numbers ranging from $10^4$ to $10^6$, where the regime of boundary layer flows is not completely turbulent, rather consisting of an initial, often significant, laminar portion. Transition from laminar to turbulent has a heavy influence on flow properties, namely, a substantial increase in skin friction, which is considerably higher in the turbulent regime. In addition, under adverse pressure gradients, laminar separation bubbles with turbulent reattachment may appear [39]. Therefore, knowledge of the location and extent of transition is relevant in the study of industrial flows and in the design and performance of aerospace devices, particularly when the effects of wall shear stress and boundary layer separation are of interest.

Three main concepts exist for transition modeling: application of low Reynolds number turbulence models, the $e^N$ method and experimental correlations.

The first method's ability to predict transition is rather coincidental since it is mainly based on reproducing the viscous sublayer behaviour instead of actually predicting transition from laminar to turbulent flow. Using low Reynolds number turbulence models without any coupling to an intermittency equation often proves to be an unreliable method of predicting transition. Furthermore, these models can only be applied to bypass transition which excludes them from being employed in many aerodynamic flows.

The $e^N$ method is considered semi-empirical. It is mostly used in 2D problems, namely for isolated airfoils, where it has been shown to produce very good transition predictions compared to wind tunnel measurements. However, for general aerospace applications, a set of barriers prevents its usage. Since it is based on linear stability theory, it cannot predict transition due to non-linear effects such as high freestream turbulence or surface roughness. Moreover, typical industrial Navier-Stokes solutions are not accurate enough to evaluate the stability equations, creating the need to couple these solutions to accurate boundary layer codes. On top of it, the need to track the growth of the disturbance amplitude ratio along the streamline results in a considerable issue for 3D flows where the streamline direction is not aligned with the grid, jeopardizing the use of this method for three-dimensional flows. In light of these considerations,

the $e^N$ method is regarded as incompatible for general industrial CFD applications.

Experimental correlations usually relate the freestream turbulence intensity, $Tu$, and the local pressure gradient to the transition momentum thickness Reynolds number. While proving sufficiently accurate, this method poses numerical and programming challenges in Navier-Stokes codes due to the necessity to compare the actual values of the former Reynolds number to the transition value from the respective correlation. Since the boundary layer edge is not well defined, such comparison requires implementation of a search algorithm that significantly increases the computational effort of CFD analyses, that are mainly based on unstructured grids and parallel execution. Therefore, the use of experimental correlations in predicting transition is incompatible with modern CFD codes.

Recent efforts by Langtry and Menter led to the devopment of a transition method with potential applicability in aeronautical flows. The model relates the maximum value inside the boundary layer of the strain rate Reynolds number to the momentum thickness Reynolds number. The former accounts for the growth of disturbances inside the boundary layer as well as their damping. Once its critical value is achieved, transition takes place. Improvements upon the former method, conducted by its authors, led to the establishment of a current state-of-the-art correlation-based transition model: the $\gamma - Re_\theta$ model, which is based on two transport equations. One is for intermittency, which is coupled with the SST $k - \omega$ turbulence model, used to trigger transition locally. The other one is for the transition onset momentum thickness Reynolds number, required to capture the non-local influence of the turbulent intensity. By tying the empirical correlation to the onset criteria in the intermittency equation, this model allows accurate simulation of transition in 3D flows, including transition induced by separation of the laminar boundary layer, and is fully compatible with modern CFD codes [21].

### 2.4.4 Spacial Discretization: Meshing

The geometric continuum representing the physical domain is translated to a numerical model representing the computational domain by means of a spacial discretization process – meshing – that distributes a finite number of points in the flowfield and solid surfaces, creating a mesh (or grid). The outcome and accuracy of a CFD analysis is heavily influenced by the mesh properties and quality and, therefore, the generated

grid must provide adequate resolution of the geometrical and expected flow features.

According to Hirsch [37], grids can be classified as structured or unstructured. Structured grids are composed of families of intersecting lines, one for each space dimension, where each mesh point is located at the intersection of one line, and one only, of each family. Connectivity between cells is predetermined, with adjacent cells having consecutive indices, explicitly defining their position relative to one another inside the computational domain. Structured grids tend to be more efficient in terms of accuracy, CPU time and memory requirement relative to their unstructured counterparts.

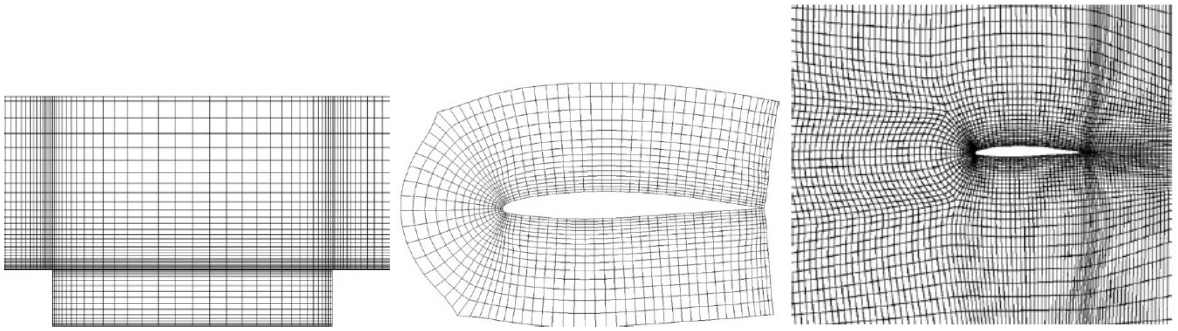


Figure 4: Examples of structured meshes: (a) non-uniform cartesian, (b) body-fitted C, (c) multi-block. Adapted from [37].

The ideal structured mesh, particularly from the accuracy perspective, is a uniform Cartesian mesh where all points are equidistant and every cell is a perfect square (2D) or cube (3D). Increasing mesh complexity can be found in non-uniform Cartesian grids that allow for variable values of the mesh spacing, typically done in order to provide a strong clustering near certain regions of interest, or allow for local refinements with hanging nodes, obtained by subdividing an initial Cartesian grid in sub-cells, either uniformly or non-isotropically. Also classified as structured are body-fitted grids, commonly employed in the presence of curved boundaries such as airfoils. The mesh is made curvilinear in order to adapt to the geometries, guaranteeing smoothness and continuity of cell sizes. Combination of different, basic structured mesh topologies applied in different regions of the computational domain is also possible, as is the overlapping of different meshes. Both multi-block and overset (chimera) grids can offer significant advantages in terms of achieving higher grid quality or adaptation to more complex geometries [37].

Unstructured meshes are defined by an arbitrary distribution of mesh points, con-

nected by polygons (2D) or polyhedrals (3D), in the computational domain. Since the grid is assembled freely, cell by cell, connectivity between cells is not preset and must be stored in a table once the generation process is finished. Despite the tendency to provide a lower accuracy than structured grids, the need to generate good quality grids on complex geometries in a convenient amount of time, through automatic processes, prompted the rise and increasing use of unstructured meshes. These are, nowadays, the dominating approach to industrial CFD. One of its main advantages is the possibility to perform local refinements in a particular region without affecting the grid point distribution outside that region, paving the way for flexible grid adaptation, a process with the objective of optimizing the number of grid points for a given level of accuracy.

Several cell shapes exist in unstructured grids, the most common being triangular/tetrahedral and quadrilateral/hexahedral. The former provides a fast, efficient and simple solution for complex geometries. The main difficulty associated with this cell shape is linked to boundary layer requirements. In near-wall regions, triangles and tetrahedra with proper height-to-base ratios, needed to provide the required grid density in the normal direction, tend to be very poorly configured and lead to a significant loss of accuracy. Hexahedral cells offer significant advantages over tetrahedra, in terms of memory requirements and accuracy, and provide a robust and efficient high-quality grid.

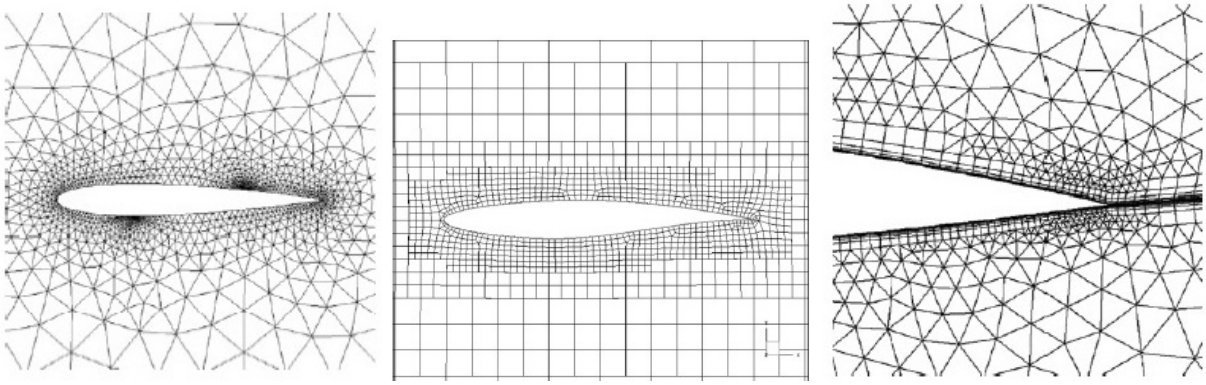

(a) (b) (c)

Figure 5: Examples of unstructured meshes: (a) triangular, (b) hexahedral, (c) hybrid. Adapted from [37].

Unstructured grids have the additional advantage of being able to incorporate layers of quadrilaterals (2D) or prisms (3D) in near-wall regions. These high aspect ratio prismatic layers, also denominated as prism layers, increase the accuracy of the flow

solution in delicate regions such as boundary layers. Combination of different cell types – hybrid grids – allows for greater flexibility, efficiency and better resolution in critical areas [37].

### 2.4.5 Near-Wall Treatment

Overall success of CFD simulations is determined in large measure by the treatment of boundary conditions at solid walls [44]. Flow in near-wall regions is especially intricate and delicate to compute due to the suppression of turbulent fluctuations and greater relevance of viscous effects in the boundary layer sublayer closer to the wall: the viscous sublayer. Such suppression significantly modifies the turbulent structure and invalidates the use of standard turbulence models all the way through the wall. Additionally, near-wall regions are also characterized by considerably large normal gradients that require a large number of computational cells generated close to the walls in order to resolve them and properly capture the boundary layer flow properties. Special modelling procedures are demanded in order to circumvent such issues, with two available approaches: the wall-function method and the explicit solution of the equations of motion and turbulence models in the near-wall region [45].

Use of wall functions is the most common industrial practice. Their theoretical basis is the universal character of the region between the wall and the outer edge of the logarithmic layer that happens for quasi-equilibrium boundary layers. It states that under certain flow conditions the form of the solution between the wall and the outer edge of the logarithmic layer is invariant when appropriate scaling, based on the friction velocity, $u_\tau$, and molecular viscosity, $\nu$, is used. A wall function relates flow variables at the first computational point, at some distance $y$ from the wall, directly to the wall shear stress without explicitly resolving the structure in between. This is accomplished by expressing the dimensionless velocity profile $U^+$ as a function of the dimensionless wall distance $y^+$. This method can only be used if the assumptions of two-dimensional Couette flow with small pressure gradients, local equilibrium of turbulence and constant near-wall shear stress layer are verified and if the value of $y^+$ at the first mesh point is within the validity limits of the wall function [45].

If the flow separates or is highly three-dimensional, the former assumptions are violated, the wall-function method cannot be applied and, consequently, the governing

equations have to be resolved all the way to the wall with a finer mesh. This alternative approach requires the use of turbulence models which are valid across the entire boundary layer, compatible with the demanded higher near-wall resolution and capable of explicitly resolving the governing equations. Such models exist in the form of low $y^+$ or low Reynolds number models [44].

On the one hand, the wall function approach is computationally more efficient due to the smaller grid size but is limited in scope to a particular set of flows. On the other hand, explicitly resolving the turbulent structures across the boundary layer demands a heavier computational effort due to the finer grid generated but is a valid option for various flow conditions where the former is not [45].

## 2.5 RPA Design Features

The layout of a RPA is intricately connected to its mission requirements. Since a wide range of roles can be assigned to these systems and the risk of trying unorthodox solutions is significantly low when compared with crewed aircraft, a highly diversed range of aircraft configurations is available [4]. The current section aims at discussing several airframe configurations typically employed by RPAs, its advantages and disadvantages and the impact of mission requirements on design features. The information is presented in what the author considers to be an intuitive fashion, starting with the wing system and followed by the engine integration, fuselage and tail configurations.

### 2.5.1 Wing System Configuration

The concepts of a conventional, canard, tandem, three-surface and flying-wing are considered, as depicted in figure 6.

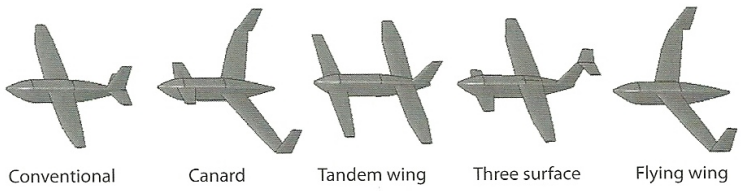


Figure 6: Wing system configurations. Adapted from [2].

A conventional wing configuration is defined by the combination of a main wing which acts as a lifting surface, thereby producing lift, and a smaller horizontal surface

located aft of the former, designed to trim the aircraft [2]. Such arrangement is by far the most ubiquitous [4]. It provides very high aerodynamic efficiency in terms of lift-to-drag ratio and endurance parameter. Since the tail is trimming the aircraft, the wing is capable of generating high lift coefficients. Additionally, negative effects such as downwash or turbulent wake on the main wing do not occur since there are no surfaces ahead of it. Other considerations that favor this wing system are its conceptual simplicity and the fact that it is well understood by design experience making it a low risk/high performance configuration option [2].

The canard configuration has a single horizontal surface – the canard – placed ahead of the main wing. Whether this arrangement is aerodynamically superior or inferior to the former, depends on the literary source. Gundlach [2] is in favour of the conventional wing, stating that the canard stall margin requirement (necessary to prevent unstable pitch break) prevents the wing from achieving its lift potential, therefore decreasing the endurance parameter. Due to the same requirement, the canard aircraft has a lower maximum lift coefficient, which corresponds to a higher stall speed. In addition, the canard produces a wake and downwash effect on the main wing, leading to a drag increase. Other authors, viz. [4] and [11], argue that the canard configuration is aerodynamically more efficient because both lifting surfaces are producing positive lift, thereby reducing total induced drag. Nonetheless it is consensual that this arrangement reduces trim and control effectiveness due to the proximity of the canard to the aircraft's center of gravity (CG). Typically, it takes packaging, special payload integration or the existence of a short fuselage to justify this approach [2].

A tandem wing configuration is characterized by the existence of two wings of similar dimensions, one placed in the front and the other in the rear of the aircraft, making it rather arbitrary to distinguish it from the previous two configurations [2]. Typically, it has a lower aerodynamic efficiency and poorer stall behaviour relative to a conventional configuration which is mainly due to the downwash and wake produced by the front wing on the rear one [11]. Therefore, the use of this configuration is usually justified by payload integration considerations or the need to accomodate for wings of very high span (which can fold into the fuselage) [2].

The three-surface configuration comprises a main wing, a canard and a horizontal stabilizer aft of the wing. It is theoretically possible for this configuration to surpass

the conventional one in terms of aerodyamic efficiency and performance. However, the analysis required to optimize the configuration for best performance demands excessive time and complexity which, for a simple RPA configuration, is not justified. Additionally, the increase in weight, manufacturing costs and supportability impacts, coupled with a higher difficulty in stability and control analysis and the lack of design experience, prevents this configuration from being widely adopted [2], [11].

Lastly, the flying-wing configuration has a single wing that acts simultaneously as a lifting and trimming surface. It is characterized by its simplicity since the manufacturing, transportation and maintenance efforts are considerably reduced relative to the remaining configurations, due to its fewer components. It also offers advantagens for stealth missions and provides a lighter aircraft. For range missions, due to the drag reduction caused by the existence of fewer parts which leads to higher lift-to-drag ratios, the flying wing becomes a good option. However, the same cannot be said for endurance missions, where the reduced lifting capacity, caused by upward elevon deflection and trim necessities, provides a lower endurance parameter relative to the conventional configuration [2]. Furthermore, as in the case of a canard arrangement, it possesses a reduced effective tail-arm and is the most difficult configuration to stabilize, even by computer [4], [11].

The wing vertical location with respect to the fuselage can be classified as high, mid or low. Without going into detail, the following remarks are considered. High wings typically provide adequate ground clearance, which allows placement of the fuselage closer to the ground, beneficial from a weight perspective. However, it may prove problematic when considering external payload integration. High wings also favour stability in detriment of maneuverability. Low wings provide greater maneuverability at the cost of ground clearance. Frequently, a dihedral angle is set in order to augment stability and provide greater clearance. The mid wing arrangement generally provides the lowest drag and is a compromise between the former two [11].

### 2.5.2 Propulsion Integration

The propulsion system design is constrained due to the design proposal requirements that demand integration of an internal combustion, fuel injected engine. Thus, electric propulsion is immediately cast aside. Jet engines and turboprops are also not con-

sidered as possible solutions given the fact that their typical and efficient employment is outside the scope of the requested operation conditions [4]. Hence, it comes down to an argument concerning reciprocating-propeller engines and two possible arrangements: pusher or tractor [2].

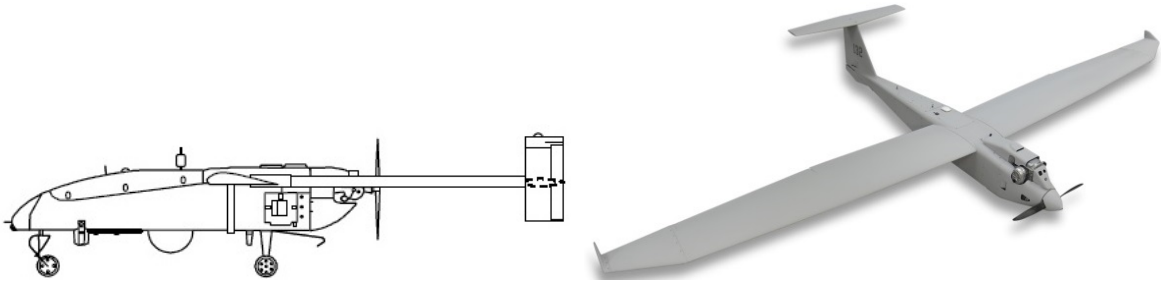

(a) (b)

Figure 7: (a) Pusher (adapted from [4]) and (b) tractor (adapted from [46]) arrangements.

Most RPAs equipped with reciprocating-propeller engines use pusher installations, largely due to beneficial payload integration options. Pusher configurations clear the front of the aircraft for the installation of the payload, providing an unobstructured view forward [4]. In addition, it protects the payload from engine exhaust and leaked fluids, sources of contamination. A tractor configuration does exactly the opposite. Additional advantages are the increase in aerodynamic performance due to the flow entrainment which causes the drag of the body ahead of the propeller to be reduced, and also pitch and yaw stabilizing effects. The downside is the reduced propeller efficiency and noise increase, both caused by the wake generated by the body ahead of the propeller [2].

Conversely, the tractor configuration, seldomly seen in RPAs, benefits from having clean airflow to the propeller which results in higher propeller efficiency and reduced levels of noise compared to its pusher counterpart. Also worthy of consideration is the impact that the propulsion system configuration has on the aircraft weight distribution. Due to longitudinal stability requirements, the aircraft center of gravity should be located ahead of the neutral point. In order to accomplish this, the aircraft usually has more weight in the front than in the rear which is in accordance with using a tractor configuration. The pusher engine is generally located in the rear or in the central sections of the aircraft which might be challenging from a stability perspective [2].

### 2.5.3 Fuselage Configuration

The fuselage configuration is intricately connected to the tail configuration and the propulsion system location. In order to be effective, the tail needs to be placed at a considerable distance from the wing to provide a proper moment arm. The ubiquitous arrangement of a conventional wing configuration with a pusher engine has two ways of meeting this requirement.

One is to place the engine in the rear of the aircraft, creating a single continuous fuselage that acts as a tail attachment. This approach has the disadvantage of placing a heavy weight far aft the CG. A minimum weight in the nose is needed to counter the engine moment and avoid stability problems.

The other is to place the engine in a central section of the aircraft, close to the CG, and make use of booms to provide for tail moment arm. Single and twin booms are both valid options with the latter being, by far, the most adopted.

Tractor arrangements typically yield single fuselages as the placement of the engine at the front of the airplane mitigates stability issues [2].

### 2.5.4 Tail Configuration

When it comes to the tail configuration, the designer is faced with numerous possibilities, some of which can be seen in figure 8.

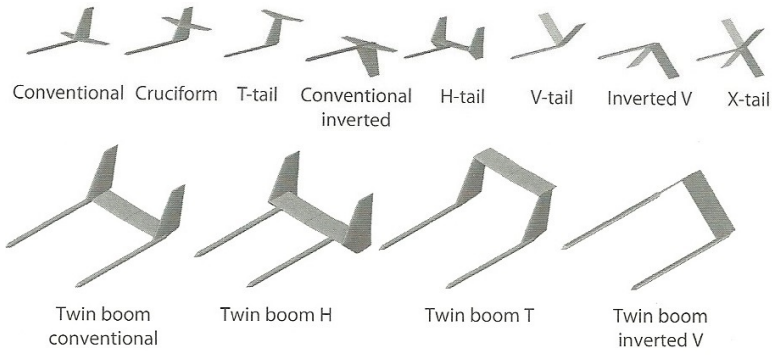


Figure 8: Examples of tail arrangements. Adapted from [2].

As depicted in figure 8, there are two main groups of tail configurations: single-attachment point and twin boom tails. This observation confirms the intricate connection between tail and fuselage configuration, previously stated. An exhaustive discussion on the pros and cons of the many possible tail configurations is not in the scope of

the present work. However, a few remarks must be made about the most predominant arrangements.

Conventional tails provide sufficient stability and control at the lowest tail weight and stand as the datum against which other configurations are compared [10]. T-tails allow for smaller vertical stabilizers due to end-plate effects and smaller horizontal ones due to their clearance from the main wing wake. The downside is the weight increase caused by the strengthening of the vertical tail in order to support the horizontal one. The cruciform tail is a compromise between the former two without the end-plate effect benefit [11].

Advantages of the H-tail are the positioning of the vertical stabilizers in undisturbed air and reduction of the horizontal stabilizer size due to end-plate effects generated by both vertical tails. Again, the need to strengthen one surface increases the overall weight above the conventional tail's reference [10]. V-tails reduce the surface area and the number of surfaces which results in a tail drag decrease, particularly interference drag. Control-actuation is more complex due to the mixing of rudder and elevator in the same surface which is prone to produce adverse yaw-roll. The inverted V-tail avoids the latter. However, it causes difficulties in providing adequate ground clearance [11].

With some minor differences, the former considerations are valid for the twin boom tails. These are typically heavier than a conventional (single) fuselage construction [11]. In the case of inverted-V tails, ground clearance is no longer an issue and the end-plate effects of the vertical stabilizers on the horizontal surface can be considered for the conventional arrangement.

## 2.6 Market Research

Perhaps the best way to conclude the current chapter, the market research acts as the ideal transition from the state-of-the-art discussion to the design process itself, providing insight into possible aircraft configurations and pertinent design aspects. First of all, the mission requirements and performance specifications given in the design proposal have to be clearly understood. Only then is the designer in position to search the aerospace market in order to find RPAs with similar performance capabilities, such as endurance, cruise speed and MTOW, that may be used as reference aircraft throughout the project.

Both international and national, military and civil areas of the RPA market are analysed. Shepard's *Unmanned Vehicles Handbook 2008* [47] offers an extensive compilation of existing RPAs and is therefore the main source of information. Additionally, special attention is taken with innovative and entrepreneurial national companies such as Tekever, Harpia Tech and UAVision as well as with further aircraft operated by the PAF.

The research results comprise a total of 10 pertinent airplanes that exhibit certain performance parameters in line with the design proposal: AAI Corporation's *Shadow 200 (RQ-7B)* and *RQ-2 Pioneer*, Innocon's *MiniFalcon*, ATE *Vulture*, Elbit Systems's *Hermes 180*, Soko ZI *B4*, Tunisia Aero Technologies's *Nasnas MK1*, L-3 BAI Aerosystems's *Viking 100*, Tekever's *AR5 Life Ray Evolution* and PAF *Antex-X03*.

The list is narrowed down to the best four aircraft, depicted in figure 9, whose characteristics and performance best match the ones coveted. Their specifications are shown in table 2, in accordance with data either provided by the respective manufacturers, viz. [48], [49] and [7], or by the UV Handbook [47].

Table 2: Market research results.

| **Features** | **Goal** | **MiniFalcon** | **Nasnas MK1** | **AR5** | **Antex X03** |
|---|---|---|---|---|---|
| MTOW (kg) | $<$150 | 150 | 125 | 150 | 150 |
| Endurance (h) | $>$8 | $<$15 | $>$14 | 8-12 | $>$15 |
| Range (km) | 300 | $<$200 | - | - | - |
| Cruise Speed (kts) | 90 | - | - | 75 | - |
| Max. Speed (kts) | 120 | 120 | 70 | - | 70 |
| Ceiling (ft) | 15000 | $<$18000 | 16000 | - | 15000 |

As a first comment, it is noticeable that none of the selected aircraft is able to fully match the design targets, highlighting the challenging and innovative aspect of the current project.

Inspection of the market research's best ranked RPAs reveals common design features between them. As a starting point, a conventional wing configuration with a main wing and aft tail is always observed, leaving out famous configurations such as canards and flying wings. The main wing is typically rectangular, although a few exhibit taper.

Propulsion is provided by pusher-propeller systems with internal combustion engines. The propulsion system placement is mostly at the aircraft's central sections, close to the CG. The *AR5* and *Hermes 180* are the only exceptions as they have the

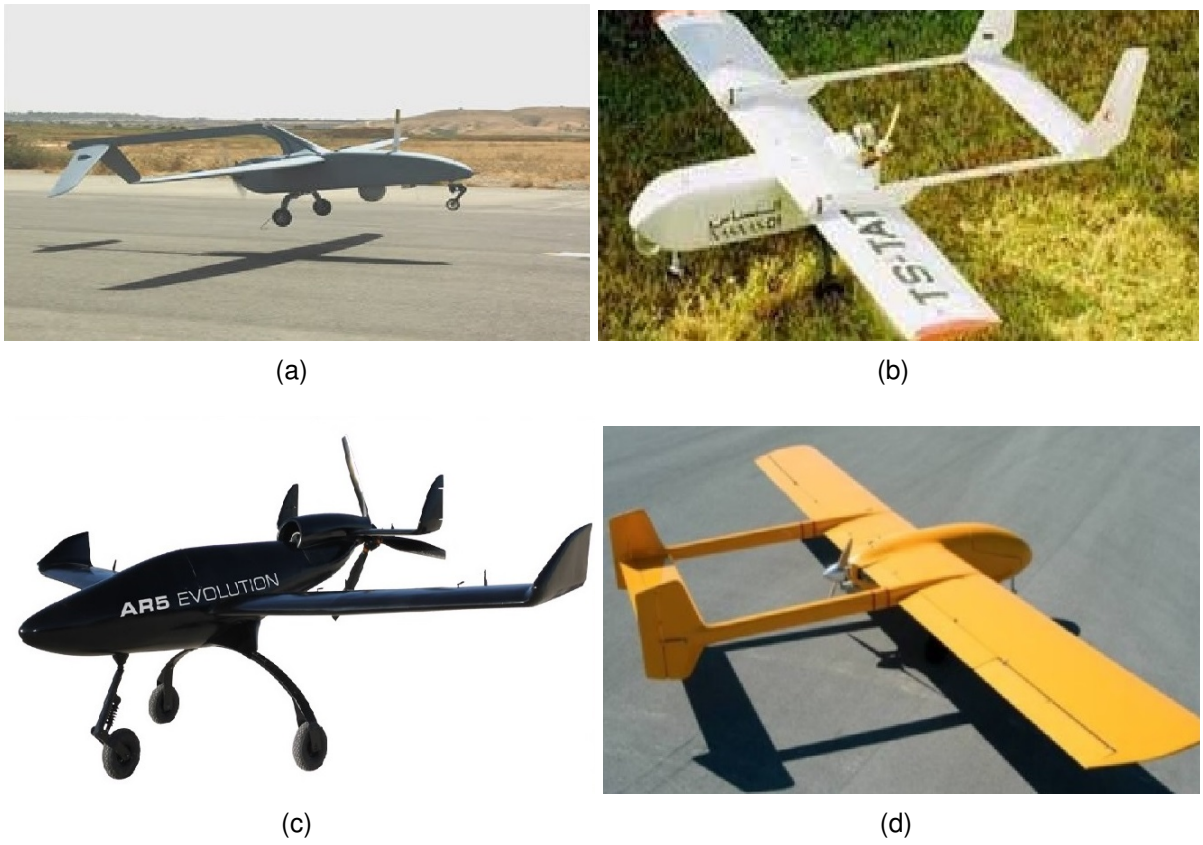


(a) (b)

(c) (d)

Figure 9: (a) MiniFalcon (adapted from [48]), (b) Nasnas MK1 (adapted from [47]), (c) AR5 (adapted from[49]) and (d) Antex X03 (adapted from [7]).

propulsion system placed at the rear. The latter option results in a configuration which is similar to many conventional manned aircraft, with a single continuous fuselage where the tail directly attaches. However, most configurations do not resemble this one, specially if the propulsion system is installed near the CG, and make use of tail booms instead. A single boom such as in the *MiniFalcon* may be used, although twin booms such as the ones in *Nasnas MK1* and *Antex X03* are more frequently designed.

H and conventional tails are predominant, accounting for 70% of the listed aircraft. The exceptions are inverted V tails used by both *MiniFalcon* and *Shadow 200 (RQ-7B)* and the *Vulture*'s T tail. Figure 9 also illustrates the tricycle dominance regarding landing gear configurations, patent in the remaining aircraft as well, with the *Vulture* being the only exception.

The market research demonstrates the expected prevalence of the twin boom pusher configuration. 60% of the RPAs identified have such a design and, of these, approximately 83% have H or conventional tails, evidencing the successful combination of twin boom pusher and H/conventional tail design. The second most frequent design is the

one using a single boom to place the tail at some distance from the main wing, whether the boom is located above (*MiniFalcon*, *Hermes 180*) or below (*Vulture*) the fuselage centerline. It comprises 30% of the selected RPAs. Tekever's *AR5* stands out as the only aicraft with a single continuous fuselage.

The successful RPA designs and respective features showcased in the current section should not be perceived as mandatory, rather as recommended. The twin boom pusher design displayed by the majority of cases analysed, or any other configuration shown, are not the only valid choices, only options that have so far proven successful. Other alternatives may present themselves as valid design options. Indeed, innovation is often a very important criteria in defining a particular design, although often accompanied by an associated risk. In the words of Jay Gundlach [2], "It is a tradeoff between the influences of "nobody ever got fired for buying a conventional twin boom pusher" and a "me too" design".

# 3 Conceptual Design

## 3.1 Concept Generation & Selection

### 3.1.1 Concept Generation

Concept generation is where the engineer's creativity steps into the frame. As demonstrated in 2.6, there is no ideal configuration, rather a broad panoply of successful solutions. Keeping in mind the mission requirements specified in the DP, the author, in collaboration with the remainder of the design team at the AFARC, developed a series of initial aircraft concepts (figure 10). Payload integration and endurance maximization are considered the design drivers, and therefore exert the strongest influence on the vehicle configuration. Nonetheless, aerodynamic performance, stability and control, weight impacts, structural complexity, manufacturing feasibility and associated costs are also key parameters to be evaluated, given their major impact on the final product.

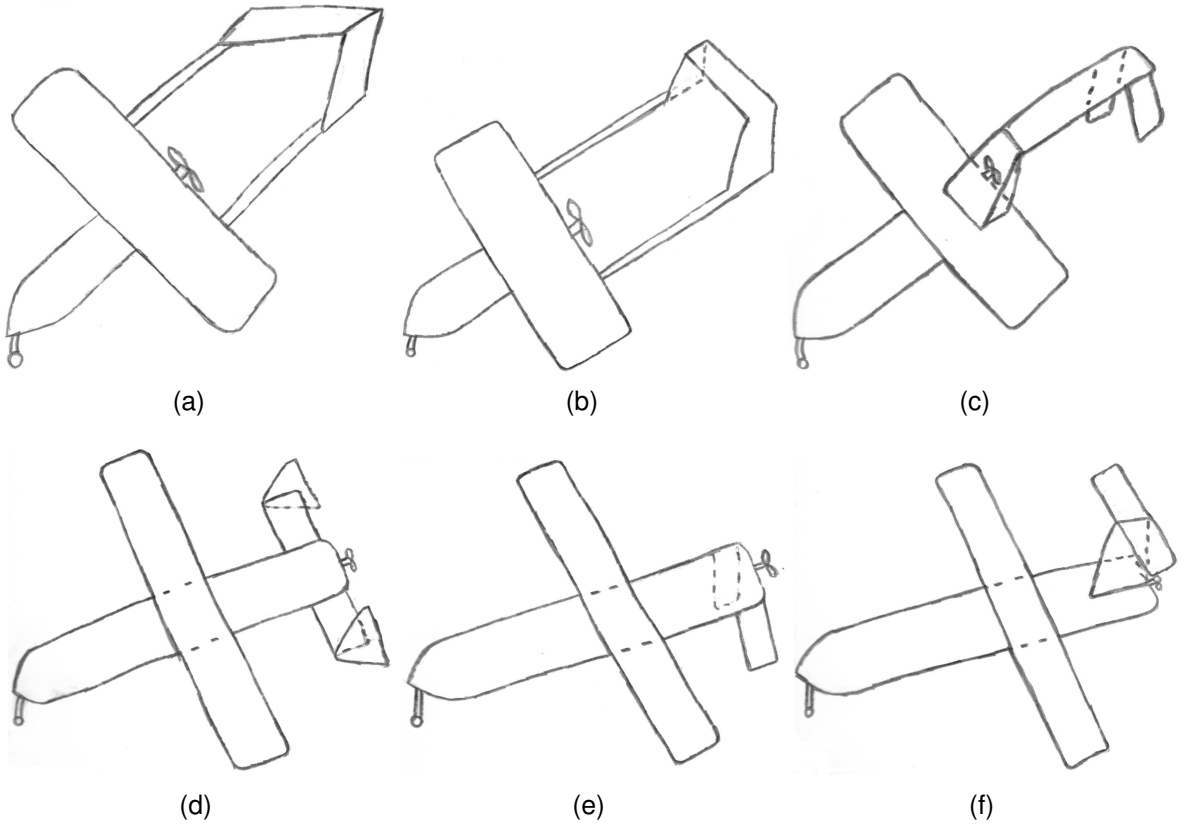


Figure 10: Sketches of several aircraft concepts: (a) Configuration 1, (b) Configuration 2, (c) Configuration 3, (d) Configuration 4, (e) Configuration 5, (f) Configuration 6.

All six concepts are defined by a conventional wing configuration. This is justified

by the debate on the topic in 2.5.1. Due to poor performance in endurance missions, difficulties related to stability and control and lack of design/operational experience in dealing with flying-wings, these are cast aside. The same goes for both tandem and three-surface configurations, where an eventual superior aerodynamic performance is overshadowed by an excessive increase in weight and design/operational complexity. The argument is between the conventional and canard arrangements, where consistency throughout the literature, regarding aerodynamic performance, fails to exist. Nevertheless, considering the inferior stability and control performance of the canard, as well as the associated lack of experience, the designer chooses a conventional wing system. Furthermore, it must be stated that the AFARC has significant experience in the manufacture and operation of the latter, which acts in its favour. Since stability is far more important than maneuverability, taking into account the mission requirements, a high wing concept is considered.

Another common feature between all six concepts is the pusher-propeller arrangement. Such is strongly based on payload integration considerations. Maritime surveillance is the primary mission, therefore payload forward field of regard is of crucial importance. In addition, avoiding payload contamination due to engine exhaust and leaked fluids is also of key importance since it may jeopardize the data collected by the optical systems (gimble) and the air pollution monitoring equipment.

Concepts 1 and 2 are the typical twin-boom pusher configurations. With the propulsion system close to the CG, they mitigate eventual stability problems. The difference between them is the tail arrangement, inverted-V and T-tail, respectively. Pros and cons of both have been discussed in 2.5.4.

Concept 3 resembles the *MiniFalcon*. Not as widely adopted as the previous two, it also brings the propulsion system close the CG and makes use of a single boom to provide tail moment arm. However, structural problems may arise from the boom connection to the fuselage, particularly excessive torsion and shear stresses caused by the weight of the boom-tail. Aggravating the situation is the fact that the fuel tanks are located at the section of the referred connection. It should also be noted that concept 3 is perceived as difficult to manufacture.

Concepts 4, 5 and 6 all aim at innovation with a single fuselage placing the engine at the rear. Such arrangement is typically lighter than a twin-boom and may even

provide better aerodynamic performance due to its fineness ratio (to be discussed at later stages of the design). The downside is the weight distribution difficulty of placing a heavy component at the rear of the vehicle, penalizing stability and control. The difference between these three concepts is the tail configuration, H-tail, inverted-V tail and T-tail, respectively. Again, their pros and cons have already been debated (2.5.4).

Due to the experience acquired in recent years in RPA flight operations, AFARC members of the design team suggested that it would be positive to keep the horizontal stabilizer out of the wake of the propeller flow. This is because changing the engine regime changes the flow generated by the propeller. If the elevator is in the wake of such flow, a need arises of continuously changing elevator deflection to answer the engine regime variations and keep the aircraft trimmed. To a certain extent, all concepts attempt to comply with the former suggestion, with concepts 4, 5 and 6 providing the best solution as the propeller is installed aft of the tail.

### 3.1.2 Concept Selection

Selecting a particular concept from a given set of possibilities is not an easy task. At such an embryonic stage of design, it is hard to quantify the influence of several design parameters on the overall aircraft performance and classify the generated concepts accordingly. In an attempt to circumvent such hindrance, the decision-making method – Analytic Hierarchy Process (AHP) – proposed by Thomas Saaty [50] is adopted. The AHP is a theory of measurement through pairwise comparisons and relies on the judgements of experts (design team) to derive priority scales that measure intangibles in relative terms. Comparisons are made using a scale of absolute judgements that represents how much more one element (aircraft concept) dominates another with respect to a given attribute (comparison parameter) [50]. The AHP approach has been validated and proven successful in aircraft conceptual design [51].

Figure 11 represents the established hierarchy in light of which all six generated configurations are assessed. This hierarchy is defined by the author in collaboration with the design team and comprises four main areas: operation, construction, maintenance and innovation. As the purpose of the RPA is to fly and accomplish a designated mission, operation is considered the most important area and, accordingly, is given the higher weight. Since the current project is constrained by the need to manufacture

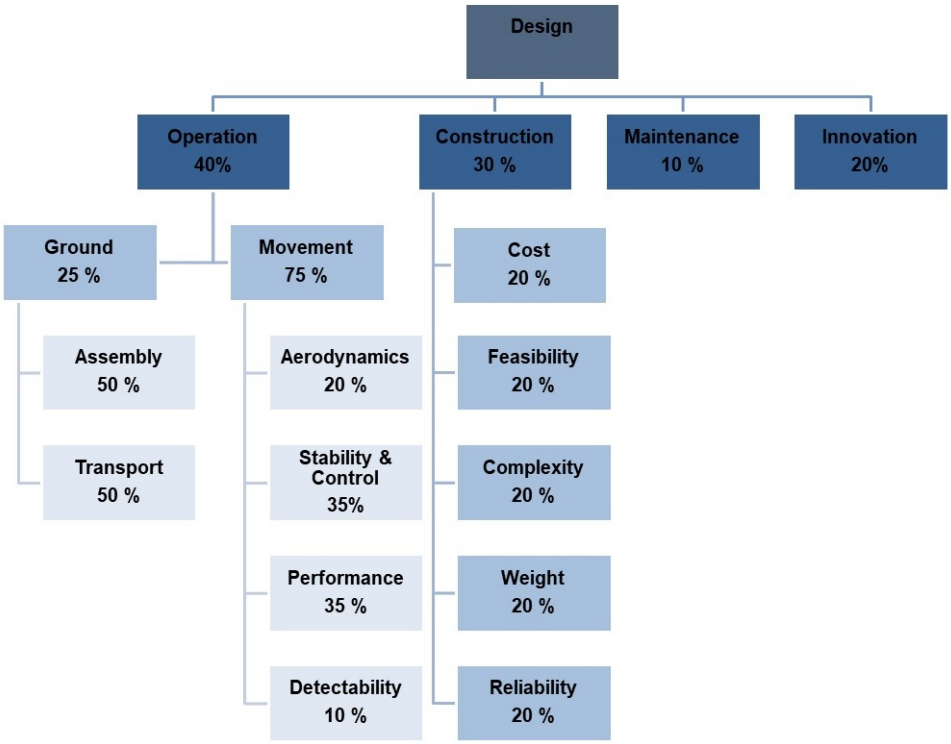


Figure 11: AHP hierarchy.

the aircraft at the AFARC, using its available resources, construction is the next most important area to be considered. Additionally, the design team considers innovation to be an important aspect of the design, which justifies a weight of 20% assigned to this area. Maintenance, although not underestimated, is considered the least important area of design.

Operation comprises both ground and movement operations. The former refers to assembly and transportation procedures (both equally important) whilst the latter encompasses all flight phases, from take-off to landing. Mission effectiveness has a stronger dependence on the latter, which explains its higher weight. Taking into account the mission requirements and design drivers, aerodynamics, flight performance and stability and control are considered key areas of design, therefore exerting a strong influence on the final decision. Given the surveillance nature of the operational context, the ability to avoid detection may determine how effectively accomplished the mission is. Therefore, detectability is also assessed. As for construction, as evidenced by figure 11, cost, feasibility, complexity, weight and reliability are considered equally important.

Each parameter is evaluated in a scale of 1 to 10, where 1 and 10 correspond to a very poor and high performance, respectively. Results are displayed in table 3.

Table 3: Evaluation of the generated concepts according to the AHP.

| **Parameter/Configuration** | **1** | **2** | **3** | **4** | **5** | **6** |
|---|---|---|---|---|---|---|
| **Operation (40%)** | 7.0625 | 7.175 | 6.8 | 7.2 | 6.6375 | 6.7375 |
| **Ground (25%)** | 8 | 8 | 8 | 7.5 | 7.5 | 7 |
| Assembly (50%) | 8 | 8 | 8 | 8 | 8 | 8 |
| Transport (50%) | 8 | 8 | 8 | 7 | 7 | 6 |
| **Movement (75%)** | 6.75 | 6.9 | 6.4 | 7.1 | 6.35 | 6.65 |
| Aerodynamics (20%) | 7 | 6 | 7 | 8 | 9 | 8 |
| Stability & Control (35%) | 7 | 8 | 7 | 7 | 5 | 6 |
| Performance (35 %) | 6 | 6 | 5 | 7 | 6 | 7 |
| Detectability (10%) | 8 | 8 | 8 | 6 | 7 | 5 |
| **Construction (30%)** | 7.6 | 8.6 | 5.8 | 7.6 | 7 | 6.8 |
| **Cost (20%)** | 7 | 9 | 6 | 7 | 6 | 7 |
| **Feasibility (20%)** | 7 | 9 | 4 | 8 | 7 | 6 |
| **Complexity (20%)** | 8 | 9 | 6 | 8 | 7 | 7 |
| **Weight (20%)** | 9 | 9 | 8 | 7 | 7 | 6 |
| **Reliability (20%)** | 7 | 7 | 5 | 8 | 8 | 8 |
| **Maintenance (10%)** | 7 | 7 | 6 | 8 | 8 | 8 |
| **Innovation (20%)** | 6 | 5 | 7 | 8 | 9 | 8 |
| ***Total*** | **7.005** | **7.15** | **6.46** | **7.56** | **7.355** | **7.135** |

In accordance with the defined criteria, configuration 4 has the highest total score and, consequently, is the one selected.

## 3.2 Preliminary Estimate of Maximum Take-Off Weight

The first step in the design of a new aircraft is to obtain an estimate of the maximum take-off weight, $W_{TO}$ [10]. This can be divided in two main groups: fixed and variable weights. The fixed weights include the payload, avionics, and in the current case the propulsion system, which has been selected by the design team and is an input to the present work. Other weights not captured in these categories that do not depend on $W_{TO}$ are also considered fixed weights. The variable weights include the structures, subsystems and energy weights, all dependent on $W_{TO}$. At this stage of design, an approximation is made by assuming that each of the variable weights varies linearly with $W_{TO}$ and therefore can be expressed in the form of a mass fraction [2].

The design proposal specifies the mission payload which comprises a synthetic-aperture radar (SR), air pollution monitoring equipment (sniffer), automatic identification system (AIS) receiver, distress sensor, pilot cam and a gimble that includes an

electro-optical (EO) sensor, an infrared (IR) sensor and a laser illuminator. The avionics set of equipment is made up by the autopilot, transponder, satellite communications (SatCom) equipment, batteries, onboard computation hardware (OCH), datalink and servo-actuators. The propulsion system weight is the sum of the engine, propeller and generator weights. All of the fixed weights, provided by the design team, are presented in table 4.

Table 4: Payload, avionics and propulsion system weights.

| **Payload** | Weight (kg) | **Avionics** | Weight (kg) | **Propulsion System** | Weight (kg) |
|---|---|---|---|---|---|
| SR | 11.34 | Autopilot | 0.11 | Engine | 10.7 |
| Sniffer | 2 | Transponder | 0.15 | Propeller | 1.5 |
| AIS receiver | 0.4 | SatCom | 0.122 | Generator | 4 |
| Distress sensor | 0.6 | Batteries | 5.6 | | |
| Pilot cam | 0.118 | OCH | 2.133 | | |
| Gimble | 1.57 | Datalink | 0.108 | | |
| | | Servos | 1.296 | | |
| **Total** | 16.03 | **Total** | 9.52 | **Total** | 16.2 |

The first variable weight to be addressed is the energy mass fraction. Since power is supplied by an internal combustion engine, the energy source is fuel. Therefore the energy mass fraction is actually the fuel mass fraction. In order to determine it, one needs to define the mission profile and calculate the fuel weight fractions for each flight segment [10]. The mission profile is sketched in figure 12 and comprises the engine start-up and take-off, climb and acceleration to cruise, cruise, descent and landing.

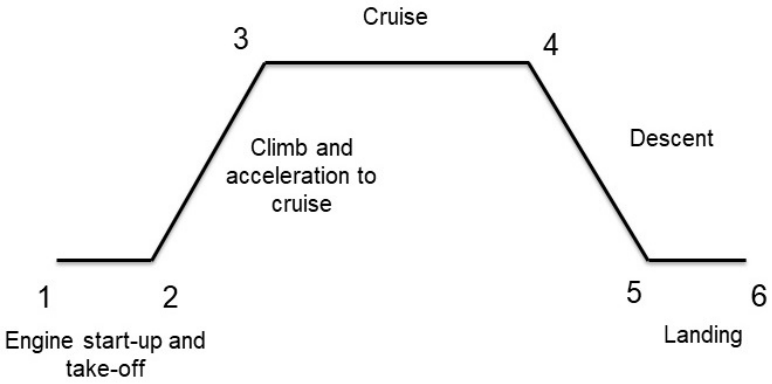


Figure 12: Mission profile.

The cruise segment can either be an endurance or range situation depending on the mission. Since one is operating RPAs from military airfields, there is no need to

consider a loiter segment before the descent and landing. The weight fraction of a segment is simply the ratio of the fuel weight at the end to that at the start of the segment [10]. Table 5 shows the results.

Table 5: Fuel weight fractions.

| **Segment** | Take-off | Climb | Cruise (Range) | Cruise (Endurance) | Descent | Landing |
|---|---|---|---|---|---|---|
| **Fraction** | 0.97 | 0.994 | 0.971 | 0.846 | 1 | 0.97 |

With the exception of the cruise segment, all fractions are determined based on historic trends. The cruise segment weight fraction is calculated using the Breguet endurance and range equations, depending on the mission [10]. These require input of a set of parameters, some of which are unknown at this stage of design. Endurance, range and cruise speed are specified in the DP. Cruise altitude is selected by the design team as 8000 ft above mean sea level (AMSL) due to payload constraints. The engine specific fuel consumption is found from the engine datasheet. The remaining parameters, propeller efficiency and lift-to-drag ratio, $L/D$, need to be estimated since, at this stage, there is not enough information for an accurate calculation. The former is taken to be 0.4 according to the design team's operational experience whilst the latter is initially estimated using the following equation [10]:

$$\frac{L}{D} = 0.94 \left[\frac{L}{D}\right]_{max} = 0.94 \cdot \sqrt{\frac{\pi \cdot e \cdot AR}{4 \cdot C_{D_0}}} \tag{8}$$

In equation 8, $AR$ is the aircraft aspect ratio, $C_{D_0}$ the parasitic drag coefficient and $e$ the Oswald efficiency factor. Aspect ratio is a major design parameter with a strong influence on the aircraft total weight and drag [11]. Given its importance, a parametric study is conducted in order to investigate the influence of the aspect ratio on the maximum take-off weight. Calculations based on the Breguet equation demonstrate that $W_{TO}$ decreases as $AR$ increases (figure 13). These calculations reflect only the influence of $AR$ on the fuel weight and not on the structural weight. At this stage of design, lack of information prevents an estimate of the latter. However, structural weight is expected to increase with aspect ratio [11]. A compromise is achieved by setting $AR = 12$.

The parasitic drag coefficient is given the value of 0.02 based on historic trends [10]

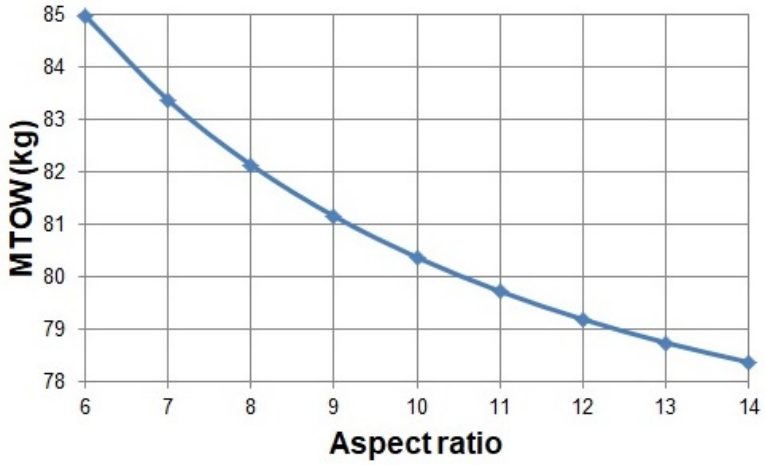


Figure 13: Maximum take-off weight vs aspect ratio.

and assuming a worst case scenario. The Oswald efficiency factor depends on the aspect ratio and is determined by the following empirical formula [11]:

$$e = 1.78(1 - 0.045AR^{0.68}) - 0.64 \tag{9}$$

A value around 0.71 is obtained. In later stages of design, once better estimates of $C_{D_0}$ are determined, one returns to the present point to correct the respective value and obtain a better prediction of the fuel weight fractions.

Since the endurance mission has a higher fuel weight penalty than the range mission, it is the one used in determining the total fuel fraction. There is still a need to account for reserve and trapped fuel which should be 5% and 1% of the total fuel, respectively [10]. Taking all this into consideration, the total fuel mass fraction is initially estimated as 22.13%, i.e., the total fuel weight is roughly 22% of the maximum take-off weight.

For RPAs, the structures weight typically varies from 10% to 20 % of the MTOW [2]. Consequently, a structural weight fraction of 0.2 is assumed as a first estimate in order to predict the worst case scenario. The subsystems weight, which in the current design refers only to the landing gear, usually varies from 3% to 6 % of the MTOW [2]. In compliance, a worst case scenario prediction is made, therefore assuming a subsystems mass fraction of 0.06.

Having all fixed weights and weight fractions determined, one is able to determine a first estimate of $W_{TO}$ by using the following relation [2]:

$$W_{TO} = \frac{W_{PL} + W_{Avion} + W_{Propulsion} + W_{Other}}{1 - (MF_{Struct} + MF_{Subs} + MF_{Energy})} \tag{10}$$

In equation 10 $W_{PL}$, $W_{Avion}$, $W_{Propulsion}$ and $W_{Other}$ represent the payload, avionics, propulsion system and other fixed weights, respectively. $MF_{Struct}$, $MF_{Subs}$ and $MF_{Energy}$ represent the structures, subsystems and energy mass fractions, respectively. The first estimate of MTOW is 80.5 kg. Later in the design process, after performing a refined weight analysis, the author will come to the conclusion that the total aircraft weight is actually slightly above 150 kg, return to the present point and iterate the whole process. For the sake of a clear description of conceptual design, henceforth $W_{TO}$ is taken as the maximum allowable and final value of 150 kg.

## 3.3 Design Point - Wing Loading and Power-to-Weight Ratio Selection

In aircraft design, typically, the design step that follows the determination of the MTOW is the wing loading, $W/S$, and power-to-weight ratio, $P/W$, selection. There are two different approaches for determining these two parameters [2]. One is to follow conventional literature approaches, viz. [11] and [10], that are based on the evaluation of several flight conditions and requirements that determine the aircraft's constraints in terms of both parameters. This approach leads to the construction of the design space graph, which contains the referred constraints and allows an easy selection of the point that gives the minimum $P/W$ for the maximum $W/S$ – the design point. In the field of RPA design, empirical data is scarce and the former method requires extrapolations that can lead to meaningless results. To bypass this obstacle, a second approach that corresponds simply to an estimation of both parameters, $W/S$ and $P/W$, based on similar aircraft, is suggested [2]. The author chooses to follow both methods and compare the results obtained in order to achieve the best possible prediction.

When considering the first approach, evaluation of all wing loading constraints is the first task. These are given by the following flight requirements and conditions: stall speed, range, endurance, maximum ceiling, glide ratio and landing. Afterwards, the power-to-weight ratio is evaluated for several flight conditions and requirements and a given range of wing loading values. These flight conditions include take-off and sus-

tained turn while the flight requirements include climb gradient, climb angle and cruise speed. For each situation $P/W$ is plotted against $W/S$. The design point is found by following two steps: first, one determines the critical flight condition/requirement which gives the minimum wing loading. Calculated values are shown in table 6. Subsequently, the critical condition for the power-to-weight ratio is determined. This corresponds to its maximum value at the minimum wing loading. Identification of the design point provides knowledge of the maximum possible $W/S$ for flight operations and the corresponding minimum possible $P/W$. This situation is illustrated in figure 14.

Table 6: Maximum wing loading ($N/m^2$) allowed for each flight condition or requirement.

| Requirement | W/S |
|---|---|
| Stall Speed | 583 |
| Range | 837 |
| Endurance | 1450 |
| Maximum Ceiling | 670 |
| Glide Ratio | 1112 |
| Landing | 450 |

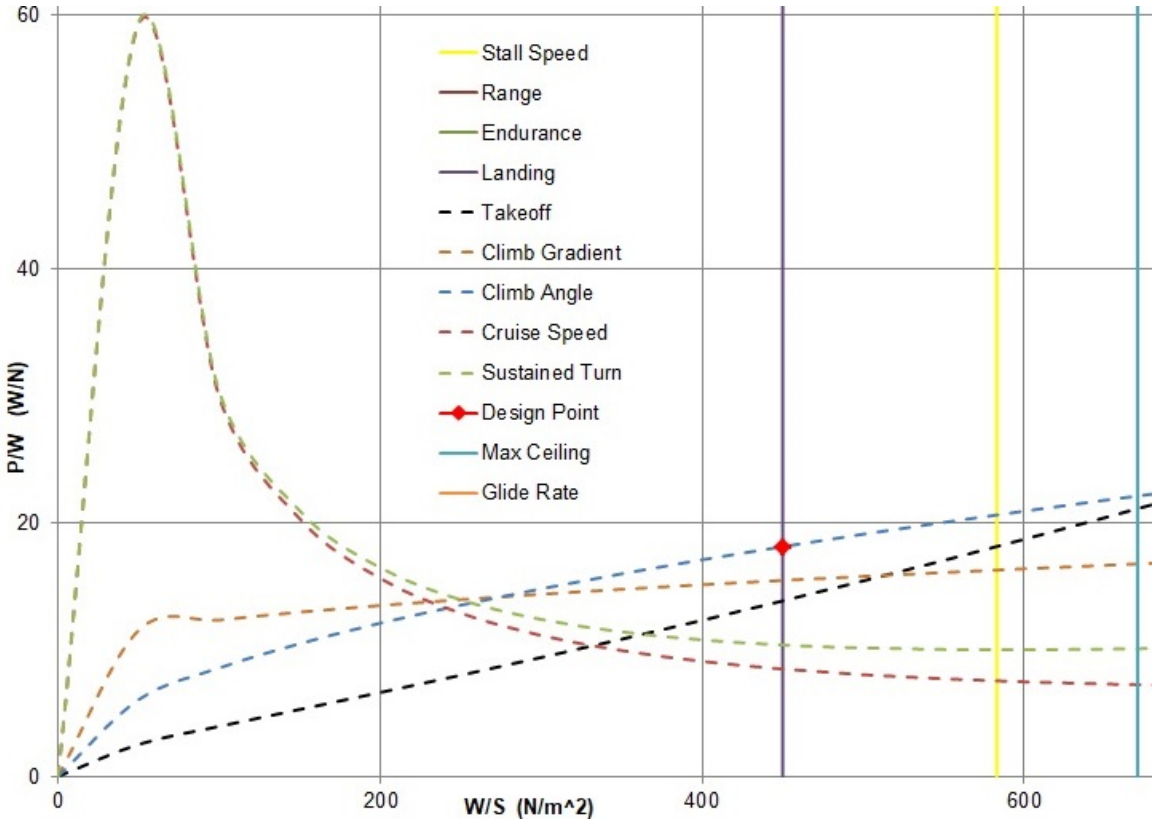


Figure 14: Representation of a segment of the design space and identification of the design point. Range, endurance and glide ratio lines are not represented.

Table 7: Wing loading ($N/m^2$) and power-to-weight ratio (W/N) for similar aircrafts.

| Aircraft | W/S | P/W |
|---|---|---|
| Pioneer | 653 | 10 |
| MiniFalcon | 534 | 19 |
| Nasnas MK1 | 537 | 15 |
| Shadow 200 | 557 | 17 |
| Hermes 180 | 637 | 15 |
| Viking 100 | 354 | 18 |
| Vulture | 404 | 19 |
| B4 | 544 | 13 |
| Antex X03 | 350 | 19 |
| AR5 | 684 | – |
| **Average** | **540.5** | **17** |

Concerning the aircraft similarity approach, all RPAs found in the market research are taken into account and the corresponding $W/S$ and $P/W$ values compilated. An average value is calculated for both parameters. Table 7 displays the results. It is relevant to refer that the wing loading values are not prescribed by the fabricants, forcing the author to make an estimate based on the aircraft weight and wing dimensions. Naturally, such prediction is prone to errors due to the lack of precision in estimating some dimensions. $P/W$ is taken directly from each aircraft datasheet.

After completing both approaches, the desired parameters are compared. As table 8 illustrates, the results obtained using the first method are more conservative, giving a lower wing loading and a higher power-to-weight ratio. Considering that a worst case scenario approach allows for a safer design, these are the selected values.

Table 8: Comparison between wing loading and power-to-weight ratio values for the different approaches employed. Units as in table 7.

| Design approach | W/S | P/W |
|---|---|---|
| Flight performance | 450 | 18 |
| Aircraft similarity | 540.5 | 17 |

Having $W/S$ determined and knowing $W_{TO}$ from previous estimates, calculation of the main wing reference area yields $S = 3.27\ m^2$. Similarly, having determined $P/W$ and $W_{TO}$, the minimum power for flight operations is found to be $P = 35.7$ HP (horse power).

## 3.4 Wing Design

### 3.4.1 Planform Definition & Flight Regime Characterization

Flight regime is characterized by both Mach and Reynolds numbers. At cruise conditions, Mach number is 0.14 which, according to the discussion in 2.2.2, is in the range of incompressible flows. The Reynolds number needs information on the wing mean aerodynamic chord, demanding a first sketch of the wing planform geometry. This is done by adding the taper ratio, $\lambda$, and leading-edge sweep angle, $\Lambda_{LE}$, to the known values of wing area, $S$, and aspect ratio, $AR$. Consequently, the wing span, $b$, root, $c_r$, tip, $c_t$ and mean aerodynamic, $\bar{c}$, chords are determined. At this point, $\lambda$ is set to unity for simplicity and $\Lambda_{LE}$ to zero according to historic trends based on the cruise Mach number [11]. Table 9 shows the results.

Table 9: Wing geometric parameters. Formulas taken from [10].

| Parameter | Formula | Value (m) |
|---|---|---|
| $b$ | $b = (S \cdot AR)^{1/2}$ | 6.26 |
| $c_r$ | $c_r = 2b/[AR(1+\lambda)]$ | 0.522 |
| $c_t$ | $c_t = \lambda \cdot c_r$ | 0.522 |
| $\bar{c}$ | $\bar{c} = 2c_r(1+\lambda+\lambda^2)/[3(1+\lambda)]$ | 0.522 |

With a characteristic length determined, the Reynolds number that defines cruise flight is computed as approximately $1.3 \times 10^6$, outside the low Reynolds number range according to the discussion in 2.2.2.

### 3.4.2 Airfoil Selection

The airfoil is the foundation of the wing, the primary source of its aerodynamic characteristics. Its shape is selected based on two criteria [10]: that it produces the *design* $C_L$ in level flight and that the range of $C_L$ values from the start to the end of cruise generates the minimum possible drag. In level flight, the required lift equals the weight of the aircraft which leads to the following expression for the lift coefficient [10]:

$$C_L = \frac{2W}{\rho V^2 S} \tag{11}$$

During cruise, as the aircraft burns fuel, its weight decreases. If altitude and velocity remain constant, this leads to a reduction in $C_L$. Having knowledge of the fuel mass

fractions, the designer is able to determine the aircraft weight at the start and at the end of cruise and, consequently, the corresponding lift coefficients. The respective values are $C_{L_{start}} = 0.42$ and $C_{L_{end}} = 0.352$. Their mean value yields $C_{L_{design}} = 0.386$.

Two options present themselves: either a new, custom airfoil is designed or one is selected from available sources. The first option requires considerable time and level of investment that the present project cannot afford. The second one is quite faster and cheaper and also enables the choice of a suitable airfoil given the vast and rich available database [2].

Therefore, having in consideration the previously calculated parameters (Reynolds number and $C_{L_{design}}$), maximization of the endurance parameter, $C_L^{3/2}/C_D$, and other important factors such as stall behaviour, thickness-to-chord ratio, $(t/c)$, and maximum lift coefficient, $C_{L_{max}}$, an exhaustive research is conducted in order to find the best airfoil. References [52] and [53] provide an extensive inventory of existing airfoils. Over 200 comprising Drela, David Fraser, Delft University, Eppler, Wortmann, NACA, Selig, Selig-Donovan, Selig-Giguere, amongst others are analysed.

All analysis are conducted using the software XFLR5 v6.33. Viscous flow with $M = 0.14$ and $Re = 1.3 \times 10^6$ is simulated over an airfoil discretized in 300 (maximum) panels using the $e^N$ transition criteria with $N_{crit} = 9$ over an angle of attack range varying from -10° to 20°. The selection process is narrowed down to six airfoils that are compared for performance purposes. Having the wing geometry defined, its 3D characteristics, based on each airfoil, are determined and represented in table 10. Naturally these, and not their 2D counterparts, act as decision criteria. As table 10 illustrates, there is no ideal airfoil. Best aerodynamic performance for cruise conditions occurs for a given airfoil whilst best stall behaviour and maximum lift coefficient are attained with a different one. The key objective of maximizing the endurance parameter acts as a tiebreaker, deciding in favour of the SG6042 airfoil, depicted in figure 15.

Figure 15: SG6042 airfoil. Adapted from [58].

The 3D lift coefficient is derived from theory and given as [10]:

Table 10: Performance results of the top six best airfoils.

| Parameter | NACA 25112 | W. FX63-147 | SG6042 | SG6043 | S1210 | S4180 |
|---|---|---|---|---|---|---|
| **Two-dimensional characteristics** | | | | | | |
| $C_{l_{max}}$ | 1.49 | 2.02 | 1.73 | 1.88 | 2.21 | 1.82 |
| $C_{l_\alpha}(/^\circ)$ | 0.113 | 0.117 | 0.097 | 0.103 | 0.113 | 0.112 |
| $\alpha_{0_l}(^\circ)$ | -1.2 | -7.7 | -5 | -7.3 | -6.8 | -4 |
| $C_{d_0}$ | 0.0082 | 0.011 | 0.009 | 0.02 | 0.07 | 0.0095 |
| $C_{d_{min}}$ | 0.0056 | 0.0065 | 0.005 | 0.0055 | 0.008 | 0.0055 |
| $C_{l_{minD}}$ | 0.1-0.3 | 0.6-1.0 | 0.4-0.8 | 0.7-1.1 | 0.6-1.2 | 0.4-1.0 |
| $(t/c)_{max}$ | 0.12 | 0.13 | 0.1 | 0.1 | 0.12 | 0.098 |
| $\alpha_{stall}(^\circ)$ | 15 | 16.4 | 16.5 | 16.5 | 13.5 | 15.5 |
| $C_{l_0}$ | 0.12 | 0.95 | 0.55 | 0.79 | 1.12 | 0.47 |
| **Three-dimensional characteristics** | | | | | | |
| $\alpha_{trim}(^\circ)$ | 2.8 | -3.8 | -0.85 | -3.1 | -2.7 | 0.1 |
| $\alpha_{stall}(^\circ)$ | 12.9 | 10.8 | 11.2 | 11.1 | 14.1 | 13.3 |
| $C_D$ | 0.011 | 0.011 | 0.0096 | 0.011 | 0.012 | 0.011 |
| $C_{L_{max}}$ | 1.34 | 1.82 | 1.51 | 1.69 | 1.98 | 1.64 |
| $C_L/C_D$ | 35.1 | 33.6 | 36.7 | 36.1 | 32.6 | 36.2 |
| $C_L^{3/2}/C_D$ | 21.8 | 20.9 | 22.8 | 22.4 | 20.3 | 22.5 |

$$C_{L\alpha} = \frac{2\pi AR}{2 + \sqrt{4 + (AR.\sqrt{1 - (M.\cos(\Lambda_{LE}))})^2(1 + \frac{\tan^2(\Lambda_{t/c})}{1-(M.\cos(\Lambda_{LE})^2}})} \tag{12}$$

$\Lambda_{t/c}$ represents the sweep angle of the wing maximum thickness line. It yields $C_{L\alpha} = 0.093/^\circ$. Due to the linear variation of the lift coefficient with angle of attack, the latter, for cruise conditions, is given as [10]:

$$\alpha_{trim} = \frac{C_{L_{design}} - C_{L_{\alpha=0}}}{C_{L_\alpha}} \tag{13}$$

$C_{L_{\alpha=0}}$ is the lift coefficient at zero angle of attack, determined having knowledge of the airfoil zero-lift angle of attack, $\alpha_{0_L} = -5^\circ$, and the referred linear variation. The output is $\alpha_{trim} = -0.85^\circ$, with $C_{L_{\alpha=0}} = 0.466$.

To provide complementary data, the wing is subject to an XFLR5 viscous flow analysis, at $Re = 1.3 \times 10^6$, using the VLM. Numerical calculations provide $C_{L_\alpha} = 0.087/^\circ$, $\alpha_{0_L} = -4.7^\circ$, $C_{L_{\alpha=0}} = 0.410$ and $\alpha_{stall} = 13^\circ$. The resulting angle of attack for cruise is $\alpha_{trim} = -0.27^\circ$. Due to their higher reliability, computational results are used throughout the project.

### 3.4.3 Wing Drag Estimation

The wing drag, divided into parasitic and induced drag, is the first component of the aircraft total drag to be determined. A two-dimensional parasitic drag coefficient, $C_{d_0}$, has already been determined during the airfoil selection process. However, due to three-dimensional effects such as flow disturbances caused by the wing attachments to the fuselage and surface imperfections like hinge gaps at movable surfaces, the three-dimensional coefficient is actually larger than the estimated $C_{d_0}$. The 3D parasite drag coefficient can be computed in the following manner [10]:

$$C_{D_0} = C_f \cdot F \cdot Q \cdot \frac{S_{wet}}{S} \tag{14}$$

In the former equation, $C_f$ is the viscous drag coefficient, $F$ the form factor, $Q$ the interference factor and $S_{wet}$ the wing wetted area.

In order to estimate $C_f$, at this stage of design, one assumes the theoretically well understood flow over a flat plate with the same Reynolds number [11]. Since transition is expected to occur, contributions of both laminar and turbulent portions of the flow are considered. A transition Reynolds number of $1 \times 10^6$ is assumed [10]. The form factor estimates the form drag contribution, particularly due to flow separations. It depends heavily on the maximum thickness-to-chord ratio of the airfoil and also on its location, sweep angle at its line and Mach number [11]. The interference factor predicts the increase in parasitic drag caused by fuselage and wing attachments interference effects. High wings have $Q = 1$ [10].

The induced drag coefficient, $C_{D_i}$, accounts for the drag generated due to lift and corresponds to the second term of equation 6.

For cruise conditions, equation 14 yields $C_{D_0} = 0.004$ and the second term of equation 6 provides $C_{D_i} = 0.0056$. The wing total drag coefficient comes as $C_D = 0.0096$. The resulting drag force is approximately 32 N.

In comparison, XFLR5 calculations provide $C_D = 0.010$, which results in a drag force around 35 N. Keeping in mind the worst case scenario approach to design and the more conservative nature of numerical results, these prevail over the semi-empirical ones.

## 3.5 Enhanced Lift Design

Typically, the enhanced lift design is conducted in later stages of the conceptual design, in order to achieve desired values of $C_{L_{max}}$, usually to meet take-off and landing distance requirements [10]. It is the author's decision to conduct such an analysis at this point to obtain better estimates of the actual values of $C_{L_{max}}$. This variable is important in the design point selection and, therefore, having a better estimate allows a more accurate prediction of the wing loading and power-to-weight ratio, reducing the chances of having to iterate the entire process at later stages.

The goal of the enhanced lift design is to achieve a given value of $C_{L_{max}}$ that satisfies take-off and landing distance requirements. In order to do so, two techniques can be employed: passive and active lift enhancement. The latter is usually the subject of STOL (short take-off and landing) and ultra-STOL aircraft designs [10] and is not justified for the present case. Passive enhancement comprises the use of traling-edge and leading-edge devices. The use of both increases the number of parts to manufacture along with the wing weight and such may not be necessary. As a starting point, only trailing-edge devices are contemplated.

Trailing-edge flaps act to increase the camber of the airfoil section, which shifts $\alpha_{0_L}$, producing a higher lift coefficient at a given angle of attack. The most common types of trailing-edge flaps are plain, slotted, split and fowler flaps [10]. For the sake of manufacture simplicity, only plain and single slotted flaps are considered for analysis.

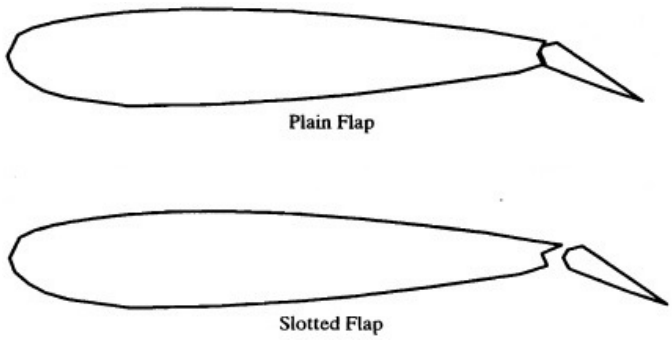


Figure 16: Schematic of trailing-edge plain and slotted flaps. Adapted from [10].

As shown in figure 16, a plain flap is merely a deflection of the trailing-edge of the airfoil section whilst a slotted flap is a plain flap with the addition of a slot at the hinge point to allow high pressure air from the lower side of the airfoil to pass over the upper surface, delaying boundary layer separation [10].

The spreadsheet approach requires three input variables and information on the type of flap desired in order to produce its output. The input variables are the ratio of the planform area of the wing having the flap span to the total wing planform area, $S_{W_F}/S_W$, the flap deflection angle, $\delta_f$, and the ratio of the flap chord to the wing chord, $c_f/c$. The output variables are the maximum lift coefficient produced by the wing, $C_{L_{max}}$, and the increase in parasitic drag due to flap deflection, $\Delta C_{D_0}$.

Table 11: Performance characteristics of different trailing-edge devices.

| **Flap Type** | $C_{L_{max}}$ | $\Delta C_{D_0}$ |
|---|---|---|
| Plain | 2.45 | 0.058 |
| Slotted | 2.61 | 0.018 |

The results shown in table 11 are obtained with $S_{W_F}/S_W = 0.54$, $\delta_f = 30°$ and $c_f/c = 0.3$. The planform area ratio is limited by the need to leave enough room for the ailerons, the deflection angle attempts to maximize the lift coefficient without generating too much drag and the chord ratio is based on historic trends [10]. The single slotted flap provides more lift and less parasitic drag than its plain counterpart, making it the best choice regarding aerodynamic performance.

The use of flaps causes the stall angle to decrease. The spreadsheet approach provides a stall angle of $\alpha_s = 11.2°$ for the wing with a clean configuration. With the flaps deflected, it decreases to $\alpha_s = 9.4°$.

## 3.6 Fuselage Sizing

The fuselage must house the payload, propulsion system, fuel storage, avionics and the remaining fixed equipment. When sizing the fuselage, the main goal of the aircraft designer is to guarantee proper dimensions in terms of height, width and length that provide the internal volume necessary for the referred accommodations while keeping its parasitic drag to a minimum [2].

In order to make the best use of the available volume, minimize empty spaces, and keep a simple concept, the fuselage cross-section is conceived as rectangular with rounded corners. Its dimensions vary along the fuselage length since different stations accommodate equipment with different volume requirements. Both width and height extend from 0.3 to 0.4 m.

Having width and height fixed by internal volume constraints, determination of the fuselage length follows. The fineness ratio, $d/l$, is defined as the ratio of the fuselage maximum diameter to its length [10]. In compliance with the former definition, considering a circular cross-section with the same area as the rectangular one, an equivalent diameter is calculated at each cross-section. The highest value is taken as the fuselage maximum diameter, $D_{max} = 0.45$ m. For subsonic conditions, the fuselage total drag coefficient is minimized by a fineness ratio of approximately 0.3 [10], resulting in a total length of $L = 1.5$ m.

With the fuselage geometry completely defined, the designer is in position of estimating the drag it generates, determining another component of the aircraft drag build-up. In this case, since there is no lift produced, only parasitic drag is generated [10]:

$$D_0 = q \cdot S_{wet} \cdot C_f \cdot F \cdot Q \tag{15}$$

In the previous equation, $q$ represents the dynamic pressure and $S_{wet}$ the fuselage wetted area. Again the friction coefficient comes from flat plate studies and depends on whether the flow is laminar or turbulent. The form factor accounts for form drag and depends solely on the fineness ratio. The interference factor is, in most cases, negligible when considering the fuselage and a value of $Q = 1$ is assumed [10].

In order to estimate the total drag, the fuselage is divided into $N$ segments of constant length. For each, the wetted area and friction coefficient are calculated and the segment drag is found. One should note that the Reynolds number used in determining $C_f$ is the local Reynolds for each segment, where the characteristic length is the segment position from the start of the fuselage. The total drag is obtained by summing up all segment contributions. [10].

At this point, given the short length produced by the theoretical optimum fineness ratio, a parametric study is conducted in order to investigate how the fuselage total drag varies with $d/l$.

One can observe by means of figure 17 that the fineness ratio for best aerodynamic performance is situated in the range 0.15–0.25, lower than the expected 0.3. Motivated by the former and by the need to increase the fuselage length (1.5 m is perceived as too short to properly harbour all components and provide adequate tail moment arm), the fineness ratio is changed to 0.15, yielding a total length of 3 m. The corresponding

fuselage drag is approximately 16.7 N ($C_{D_0} = 0.005$).

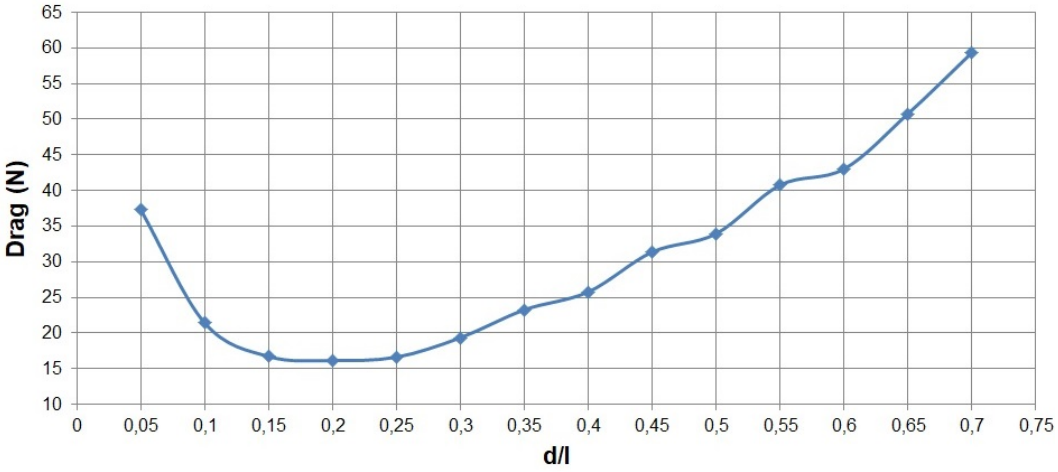


Figure 17: Fuselage total drag vs fineness fatio.

## 3.7 Tail Design

### 3.7.1 Horizontal Tail Sizing

Initial sizing of the horizontal tail is based on empirical data through the use of a coefficient that correlates features of different aircraft relevant to the tail design. It is defined as [10]:

$$C_{HT} = \frac{S_{HT} \cdot l_{HT}}{\bar{c}_w \cdot S} \tag{16}$$

$S_{HT}$ represents the horizontal tail planform area, $l_{HT}$ the distance between the quarter-chord locations of the mean aerodynamic chords of the main wing and horizontal stabilizer, and $\bar{c}_w$ the main wing mean aerodynamic chord.

Due to the lack of empirical data and historic trends on RPA design, there is no information on tail coefficients available in the literature. Therefore, an approximation has to be made based on aircraft similarity. With this in mind, the horizontal tail coefficient is taken from the *homebuilt* aircraft category, yielding $C_{HT} = 0.5$ [11].

In order to meet the coefficient requirement, the designer can adjust the tail surface area or its location. Increasing the surface area results in a weight and wetted area increase, both undesirable. Corke [10] suggests fixing $l_{HT}$ and, consequently, calculating $S_{HT}$. In compliance with this, and considering the fuselage length and the estimated

locations of both wing and horizontal tail, $l_{HT}$ is initially fixed at 1.44 m, resulting in a surface area of $S_{HT} = 0.59\ m^2$.

Having the area and location defined, determination of the planform shape follows. Typically, for aft-horizontal tails, aspect ratio varies from 3 to 5 and the taper ratio is situated in the range 0.3–0.6 [10]. At this stage of conceptual design, the author sets $AR = 4$ and $\lambda = 1$ in order to provide some aerodynamic efficiency yet keep the simple design of a rectangular surface that mitigates the risk of tip stall. Using the formulas in table 9, the following parameters follow: $b = 1.54$ m, $\bar{c} = 0.385$ m. No immediate advantages follow from sweeping the horizontal stabilizer at the given cruise Mach of 0.14. If anything, not adding sweep facilitates the structural design and manufacturing process.

Flow over the horizontal tail is defined by a Reynolds number around $1 \times 10^6$. This parameter is of key importance in the next step of the tail sizing, which is the airfoil selection. The airfoil section used for the tail should be selected based on two criteria: being a symmetric airfoil and having a low parasitic drag coefficient [10]. An additional important factor is the need to provide pitch-up control. To do so, the selected airfoil must ensure that the horizontal stabilizer stalls after the main wing, $\alpha_{s_{HT}} > \alpha_{s_W}$.

Several symmetric airfoils of the NACA family are subject to XFLR5 v6.33 flow analysis. The simulations are characterized by viscous flow with $M = 0.14$ and $Re = 1 \times 10^6$ over an airfoil discretized in 300 panels using the $e^N$ transition criteria with $N_{critic} = 9$. Angle of attack varies from -10° to 20°. The most significant results are displayed in table 12. The NACA 0009 (figure 18) is selected as a compromise between obtaining a low drag coefficient and a high stall angle.

Table 12: Performance results of NACA airfoils considered for the tail design.

| **Parameter** | **NACA 0008** | **NACA 0009** | **NACA 0010** | **NACA 0012** |
|---|---|---|---|---|
| **Two-dimensional characteristics** | | | | |
| $C_{l_{max}}$ | 1.08 | 1.20 | 1.28 | 1.35 |
| $C_{d_0}$ | 0.004 | 0.0045 | 0.0048 | 0.0055 |
| $C_{l_{minD}}$ | 0-0.2 | 0-0.2 | 0-0.2 | 0-0.2 |
| $(t/c)_{max}$ | 0.08 | 0.09 | 0.1 | 0.12 |
| $\alpha_{stall}$ (°) | 10.8 | 12.2 | 13.5 | 15.0 |
| **Three-dimensional characteristics** | | | | |
| $C_{D_0}$ | 0.00063 | 0.00065 | 0.00066 | 0.00069 |
| $\alpha_{stall}$ (°) | 14.2 | 15.8 | 16.8 | 17.8 |

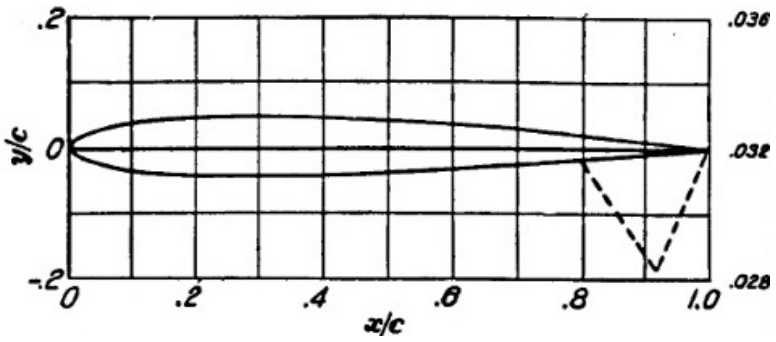


Figure 18: NACA 0009 airfoi. Adapted from [52].

At this point, lack of information prevents the designer from determining the required tail lift to trim the aircraft. Thus, the horizontal tail induced drag cannot be predicted. Consequently, only parasite drag, expressed in the form of a drag coefficient given by equation 14, is estimated. The previous discussion in 3.4.3, regarding equation 14, applies for the tail design as well, with some differences: the form factor, $F$, is increased by 10% in order to account for the effects of hinge gaps that occur by the elevator and the interference factor, $Q$, depends on the tail arrangement. For an H-Tail, $Q = 1.08$ [10]. The ratio $S_{wet}/S$ is the ratio of the horizontal tail wetted area to the wing planform area. The horizontal stabilizer drag is estimated as 2.2 N ($C_{D_0} = 0.00065$).

For comparison purposes, the horizontal tail is subject to an XFLR5 viscous flow analysis, at $Re = 1.0 \times 10^6$, using the VLM. Results yield a stall angle of 16.5° and a drag force of 2.6 N. Both are considerably similar to the semi-empirical estimates. For the drag build-up, the more conservative value is used.

### 3.7.2 Vertical Tail Sizing

The sizing of the vertical tail follows the same procedure as the horizontal one. It starts with the use of a tail coefficient, $C_{VT}$, based on empirical data of similar aircraft [10]:

$$C_{VT} = \frac{S_{VT} \cdot l_{VT}}{b_W \cdot S} \tag{17}$$

$S_{VT}$ represents the planform area of the vertical tail, $l_{VT}$ the distance between the quarter-chord locations of the mean aerodynamic chords of the main wing and vertical stabilizer, and $b_W$ is the span of the main wing. As for its horizontal counterpart, the vertical tail coefficient is chosen from the *homebuilt* category as $C_{VT} = 0.04$ [11].

Given the fact that the vertical tail is aligned with the horizontal stabilizer, an approx-

imation is made in which their quarter-chord locations are assumed to be the same, i.e., $l_{VT} = l_{HT}$ =1.44 m. Equation 17 provides $S_{VT} = 0.57\ m^2$. Since the vertical tail is divided in two panels, one at each end of the horizontal tail, the area of each panel comes as $S_{panel} = S_{VT}/2 = 0.28\ m^2$.

Typical values of aspect and taper ratio range from 1.3 to 2 and from 0.3 to 0.6, respectively [10]. Observing the approach used for the horizontal tail planform, as a starting point, the designer sets $AR = 2$, $\lambda = 1$ and $\Lambda_{LE} = 0$. Again, using the expressions in table 9, the planform shape of each panel is characterized by: $b = 0.75$ m, $\bar{c} = 0.377$ m.

A Reynolds number of approximately $9.8 \times 10^5$ characterizes the flow regime over each vertical panel. Since both horizontal and vertical stabilizers operate at very similar Reynolds, the results obtained with the XFLR5 simulations in 3.7.1 are considered valid for the vertical tail. The NACA 0009 airfoil follows as the best choice.

Regarding the drag contribution of the vertical tail, the foregoing discussion (3.7.1) applies. On the one hand, semi-empirical estimates yield a panel drag of 1.05 N ($C_{D_0} = 0.0003$) that results in a total drag of 2.1 N ($C_{D_0} = 0.0006$). On the other hand, numerical results provide a panel drag of 1.26 N which results in a total drag of 2.5 N. According to the worst case scenario approach, the latter is used throughout the project.

## 3.8 Propulsion System

Due to project organization issues, the analysis of the propulsion system is assigned to a different member of the design team and the selected engine is simply inputted into the present work. However, there is a need to check the engine performance characteristics to make sure they meet the mission requirements. To do so, one must first compute the total aicraft drag, which, according to the equations of motion for steady level flight, equals the amount of thrust that the propulsion system has to generate [10].

### 3.8.1 Drag Build-Up

At this point, drag contributions of the main wing, fuselage and tail surfaces have been accounted for. However, the drag build-up is not completed since information concerning landing gear and external payload drag is missing.

Estimates for the landing gear drag are taken from [14] since they are considered by the author as more refined, capable of providing better predictions. The landing gear components that generate drag are the tires and struts. The respective equations for determining their contributions to the aircraft parasitic drag coefficient are [14]:

$$C_{D_{0_{tires}}} = \sum_{i=1}^{n} C_{D_{0_{tires\ i}}} \left( \frac{S_{tires\ i}}{S} \right) \tag{18}$$

$$C_{D_{0_{strut}}} = \sum_{i=1}^{n} C_{D_{0_{strut\ i}}} \left( \frac{S_{strut\ i}}{S} \right) \tag{19}$$

In the former set of equations, $n$ is the number of wheels/struts, $C_{D_{0_{tires\ i}}}$ and $C_{D_{0_{strut\ i}}}$ represent the drag coefficient of each wheel/strut, and $S_{tires\ i}$ and $S_{strut\ i}$ the frontal area of each wheel/strut.

The landing gear is divided into main and nose gear. The former has two wheels and struts whereas the latter has simply one wheel and strut, of smaller dimensions. Their respective drag coefficients are $C_{D_{0_{tires\ i}}} = 0.3$ and $C_{D_{0_{strut\ i}}} = 0.1$ (fairing devices are considered for the struts) [14]. At an early stage of design, it is hard to have accurate information of the final landing gear geometry. As a starting point, the diameter and width of the tires, as well as the length and width of the struts are based on the *Antex X03*, justified by operational experience acquired by the AFARC. The previous set of equations yields $C_{D_{0_{tires}}} = 0.0021$ and $C_{D_{0_{strut}}} = 0.0031$. The total drag created by the landing gear is approximately 17.4 N.

Both gimble and SR are the payload components that, during cruise, are exposed to the external airflow and therefore generate parasitic drag. Lack of information concerning the latter's dimensions prevents the designer from estimating its drag. Nevertheless, it is possible to approximate the geometry of a gimble to that of a sphere and determine its contribution to the total drag [2]:

$$C_{D_{sphere}} = C_{d_{sphere}} \frac{S_{f_{sphere}}}{S} \tag{20}$$

In equation 20, $C_{d_{sphere}}$ is the sphere drag coefficient and, $S_{f_{sphere}}$ its frontal area. Considering a sphere diameter of 0.14 m which results in a Reynolds of $3.65 \times 10^5$, empirical data determines $C_{d_{sphere}} = 0.41$ [2]. The result is $C_{D_{sphere}} = 0.0019$, giving a drag force of 6.5 N.

Summing up the contributions from the main wing, fuselage, tail surfaces, landing gear and payload, the aircraft total drag, for cruise conditions and a clean configuration, is roughly 80 N.

### 3.8.2 Engine Performance

The propulsion system comprises the UAV Engines's *AR741*. Table 13 shows the engine specifications, as provided by the design team.

Table 13: UAV Engines's *AR741* specifications.

| Parameter | Value | Units |
|---|---|---|
| Power (maximum) | 38 | BHP |
| Rotational Velocity ( Maximum Power) | 7800 | RPM |
| Weight | 10.7 | kg |
| Fuel Consumption (Maximum Power) | 0.57 | lb/bhp/hr |
| Fuel Consumption (Cruise) | 0.52 | lb/bhp/hr |

A thrust force of 80 N is mandatory to assure level flight. The shaft power required to produce this force can be found using the definition of the propulsive efficiency [10], where $T$ represents thrust:

$$\eta_P = \frac{Thrust\ Power\ Output}{Shaft\ Power\ Input} = \frac{TV}{P} \tag{21}$$

With the estimated propeller efficiency of 0.4, at cruise conditions the required shaft power input is around 12.5 HP, easily achieved with the present engine.

The propulsive system is equipped with a two-blade composite propeller having a diameter of approximately 70 cm. Propeller tip compressibility effects typically occur at propeller tip Mach numbers, $M_{tip}$, above 0.85 [10]. Due to lack of information on engine performance curves (not yet supplied by the manufacturer), it is hard to estimate the engine rotational velocity at cruise conditions. In light of this, the designer considers a worst case scenario situation, with the engine operating at maximum power during cruise, yielding $M_{tip} = 0.88$. In this situation, compressibility effects at the propeller tips occur which, have a negative impact on the propulsive efficiency. Additionally, propeller-generated sound levels become significant at $M_{tip} > 0.85$ [10]. However, since cruise flight at maximum power output is not expected, the compressibility effects due to high propeller tip speeds can be neglected for this flight segment.

As a final check on engine performance, static thrust $(V = 0)$ is determined. The propulsive system is able to supply the RPA with a static thrust of 695 N at mean sea level (MSL) conditions and 562 N at an altitude of 10000 ft. These values are used in later stages of design, during the take-off and landing analysis.

## 3.9 Refined Weight Analysis

In order to properly address the forthcoming issues of static and dynamic stability as well as aircraft performance, a more precise and accurate weight estimate is needed. The weight analysis conducted in section 3.2 typically provides suitable approximations that are roughly within 20% of the true weight. Nonetheless, they do not capture design details and tend to underpredict $W_{TO}$. As the design matures and more information about the aircraft is known, more complex weight relationships can be used. The main objective is to define the MTOW and distribute the weights across major groups with more detail and accuracy where possible. The methodology used to accomplish this depends on statistical information based on previous designs. The aircraft total weight is divided into five main groups: structural weight, $W_{struct}$, propulsion system weight, $W_{pwr}$, fixed equipment weight, $W_{feq}$, payload weight, $W_{PL}$, and fuel weight, $W_{fuel}$ [2].

The structural weight is composed by the wing, fuselage, tail and landing gear weights. No ideal statistical approach exists. Empirical relations used in the design of crewed aircraft [10], although abundant, are not expected to comply with a RPA design as they are based on reference aircraft with considerably different performance characteristics and total gross weight. Conversely, empirical data specifically gathered for RPAs can be found in [2], although its reliability is of question due to the paucity of data. Both approaches are considered for comparison purposes. Concerning the first approach, empirical data is obtained from the *general aviation* aircraft category as it is the available category which resembles class I RPAs the most.

As one can observe in table 14, only the wing weight does not change significantly with the approach used. There is a general tendency for the approach suggested in [10] to provide higher values. Following the basis of assuming the worst case scenario, $W_{struct} = 51.6$ kg.

The propulsion system weight comprises the engine, propeller, fuel system and generator weights. The fuel system consists of fuel tanks, pumps, fuel lines, valves

Table 14: Structural weight determined by crewd aircraft [10] and RPA [2] statistical approaches. Units are in kg.

| Structural component | Corke [10] | Gundlach [2] |
|---|---|---|
| Wing | 18.9 | 18.5 |
| Fuselage | 12.1 | – |
| Tail | 4.8 | 2.8 |
| Landing gear | 15.7 | 9 |
| **Structural Weight** | **51.6** | **30.3** |

and venting. The uninstalled engine and generator weights are known. The remaining are estimated via empirical relations [2].

The fixed equipment weight contains the instrumentation, communications, wiring, flight control system, electrical system, environmental control system, auxiliary power unit and also the paint weight. The instrumentation subgroup consists of the autopilot, air data system, GPS antenna, inertial navigation system and the onboard computation processors. The latter and the autopilot are known, the remainder are taken from statistical estimates [2]. The communications subgroup comprises the data link equipment, the line-of-sight (LOS) communication equipment and the SatCom, all of which are known weights. The flight control system, auxiliary power unit and electrical system (composed by the batteries and the energy converter box) are also known. Wiring, environmental control system and paint weights are estimated from historic data [2]. The sum of all these weights is multiplied by an installation factor, yielding the installed fixed equipment weight.

The weight of all payload elements has been identified in section 3.2. The fuel weight estimate is refined in order to account for the oil weight [2].

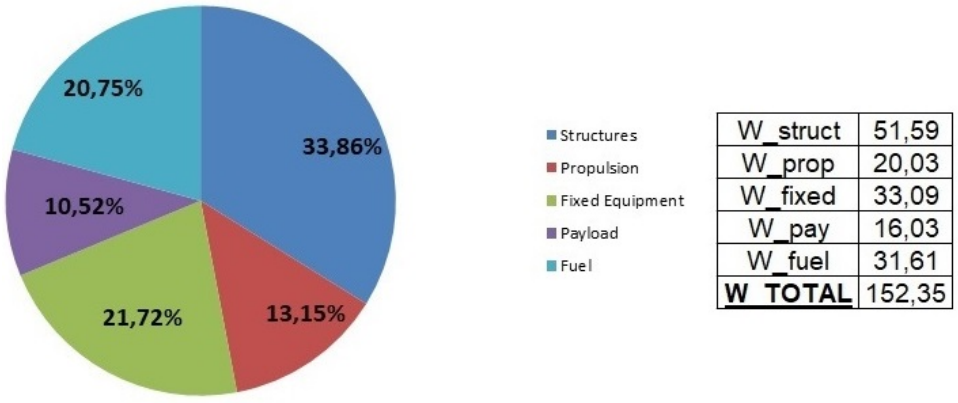


Figure 19: Maximum take-off weight and respective subgroups. Units in kg.

The refined weight analysis results in a take-off gross weight of 152.4 kg, above the maximum allowable MTOW for class I RPA. Since several worst case scenarios were assumed in the weight build-up process and some of the empirical relations used tend to overpredict the weight, it is plausible that the actual MTOW is under 150 kg. However, an accurate estimate can only be performed at the preliminary design level.

## 3.10 Static Stability

Static stability exists if, given a disturbance of an equilibrium state of flight, the forces created by the disturbance act in order to restore the aircraft to its original state of motion. It is of key importance that the aircraft is statically stable in flight for any of the three directions of motion: longitudinal (pitch), lateral (roll) and directional (yaw) [10].

### 3.10.1 Static Margin

The static margin is defined by equation 22, where $x_{np}$ is the longitudinal position of the aircraft neutral point (NP) and $x_{cg}$ the longitudinal position of the aircraft center of gravity. For stability, the static margin has to be positive which means that the CG must to be forward of the NP [10].

$$SM = \frac{x_{np} - x_{cg}}{\bar{c}_w} \tag{22}$$

The refined weight analysis allows an initial prediction of weight distribution along the aircraft length. As the engine is installed in the rear of the aircraft, the fixed equipment and payload ought to be placed, if possible, in the front in order to balance the weight. Since the fuel tanks should be situated near the CG in order to minimize its variation as fuel is burned, an aircraft CG without considering the fuel system is firstly computed. Subsequently, two separate fuel tanks are placed forward and aft of the formerly determined CG, at the same distance, in order to keep its position constant.

The neutral point is defined as the CG location that provides no change in pitching moment as angle of attack is varied. A semi-empirical estimate is performed, accounting for wing, fuselage, tail and engine contributions [11].

According to the design team's operational experience, the static margin should be in the range 15%-30%. Compliance with this recommendation proved difficult and

could only be achieved after an exhaustive iterative process, in which the location of several components was constantly adjusted. The designer settled for a static margin of roughly 20%, obtained with CG and NP locations of 1.48 m and 1.58 m, respectively.

However, compliance with static margin recommendations was achieved at the cost of tail effectiveness. In order to move the NP away from the CG, the main wing had to be placed aft of its initial position, resuting in a decrease in tail moment arm from the initial 1.44 m to 1.19 m. Due to this reduction, both horizontal and vertical tail coefficients dropped to 0.41 and 0.033, respectively. Further investigation on this topic led the to the conclusion that, for an H-tail design, the horizontal tail coefficient can be reduced by 5% [10], resulting in an initial requirement of $C_{HT} = 0.475$. Nevertheless, both actual horizontal and vertical tail coefficients are below the recommended values of 0.475 and 0.04, respectively. This does not necessarily represent a design handicap since these values are taken from the *homebuilt* aircraft category (simply the one that evidences greater similarity with RPAs) as a reference for the tail initial sizing. Future calculations prove that the actual tail coefficients are adequate.

### 3.10.2 Stability Derivatives

The stability derivatives measure the aircraft's reponse to a changing pitch, roll or yaw angle condition. The longitudinal, lateral and directional stability requirements, in terms of their derivatives, are given as [10]:

$$C_{M_\alpha} = \frac{dC_M}{d\alpha} < 0 \quad ; \quad C_{\mathcal{L}_\beta} = \frac{dC_\mathcal{L}}{d\beta} < 0 \quad ; \quad C_{n_\beta} = \frac{dC_n}{d\beta} > 0 \tag{23}$$

In the previous set of equations, $C_M$, $C_\mathcal{L}$ and $C_n$ represent, respectively, the pitching moment, rolling moment and yawing moment coefficients of the aircraft and $\alpha$ and $\beta$ the aircraft angle of attack and sideslip angle.

All derivatives are computed from semi-empirical relations that take into account the contribution of different aircraft components [11]. $C_{M_\alpha}$ is determined directly from the symmetric of the product between the static margin and the main wing lift coefficient, considering contributions from the main wing, fuselage, horizontal tail and engine. $C_{n_\beta}$ depends on the main wing, fuselage and vertical tail. As for $C_{\mathcal{L}_\beta}$, both the main wing and vertical stabilizers exert a considerable influence.

Calculations demonstrate that $C_{M_\alpha} = -1.05$, $C_{n_\beta} = 0.08$ and $C_{\mathcal{L}_\beta} = -0.04$. An

appropriate range of values for the first two derivates is $-1.5 < C_{M_\alpha} < -0.16$ and $0.08 < C_{n_\beta} < 0.28$ [10]. $C_{\mathcal{L}_\beta}$ should have a magnitude about half that of $C_{n_\beta}$ at subsonic speeds [11]. As expected, the longitudinal and lateral derivatives are negative and the directional derivative positive, with their magnitudes in the expected range of values. Hence, at a conceptual level, the aircraft is considered to have adequate static stability characteristics.

### 3.10.3 Tail Force & Trim Drag

In order to keep the aircraft balanced, the horizontal tail must generate lift [10]. Knowing the total weight and CG location during cruise, as well as the location of the main wing and horizontal stabilizer's aerodynamic center, an initial estimate of the resulting tail force is computed as approximately -61 N (downwards).

In section 3.4 it is stated that for level flight the lift generated by the main wing must compensate the aircraft weight. However, as the present section illustrates, in order to keep the airplane trimmed, the wing lift must compensate both the aircraft weight and negative lift produced by the horizontal tail [10]. An iteration is therefore required in order to update $C_{L_{design}}$.

Since the horizontal tail generates lift, it will also generate lift induced drag – trim drag – that must be accounted for. This drag component is defined as [10]:

$$D_{trim} = \frac{L_{HT}^2}{q \cdot S_{HT} \cdot \pi \cdot AR_{HT} \cdot e_{HT}} \tag{24}$$

$L_{HT}$ represents the horizontal tail lift, $AR_{HT}$ the horizontal tail aspect ratio and $e_{HT}$ its Oswald efficiency factor, estimated as approximately 0.8 [11].

For cruise conditions, $D_{trim} = 0.6$ N. As a rule of thumb, the trim drag should be less than 10% of the airplane total drag [10]. In the current case it is roughly 0.7%, proving that the static margin does not have a negative impact on performance.

The trim drag has to be included in the drag build-up, leading to a new value for the aircraft total drag at cruise conditions. Iterating, the total drag comes as 83 N and the required power for cruise as 12.9 HP.

### 3.10.4 Control Surfaces Sizing

Initial sizing of the primary control surfaces – ailerons, elevator and rudder – is dealt with in the present section. In order to keep a coherent, linear wing structure, the aileron chord is set to equal the flap chord, i.e., 30% of the wing chord. According to historical guidelines, this ought to correspond to a ratio of total aileron span and wing span in the range 0.3-0.37 [11]. Knowing that 6.4% of the wing span is integrated on the fuselage and 54% is occupied by the flaps, the remaining 39.6% is left available for the ailerons. Consequently, these are designed to extend along 36% of the wing span, meeting the empirical recommendations and leaving a safety margin of 3.6%. According to Raymer's semi-empirical formulas [11], for the referred parameters, an aileron deflection of 30° results in a roll rate of approximately 22.4 °/s.

Elevators and rudders generally begin at the side of the fuselage and extend to about 90-100% of the tail span and 25-50% of the tail chord [11]. In lack of a methodic approach to elevator sizing, the design team considers a worst case scenario corresponding to stall, in order to design this control surface. When flying at stall speed, the horizontal tail needs to generate a lift coefficient around -0.39 to trim the airplane. XFLR5 simulations show that, for an elevator extending from the fuselage to the tip of the tail, with 30% of the tail chord and a deflection of 30°, the necessary lift coefficient is attainable. Thus, an initial prediction of this control surface design is accomplished.

The rudder is typically sized in order to provide directional control capable of holding a zero sideslip angle based on a worst case condition consisting of one of two scenarios: an asymmetrical power condition caused by having one engine out or landing and take-off in a cross-wind of $0.2V_{TO}$ and $\beta = 11.5°$ [10]. Since the RPA under design is equipped with a single engine, the first scenario is inapplicable. Considering the landing and take-off in cross-wind situation, a rudder with roughly 30% of the vertical stabilizer area and a deflection of 20° should be able to provide proper directional control [10]. This condition yields a necessary control surface area of 0.085 $m^2$ that can be achieved with the rudder extending along the entire span of the tail and up to 30% of its chord.

## 3.11 Dynamic Stability

After assuring that the aircraft is statically stable in all three directions of motion, the following design step deals with guaranteeing dynamic stability. Dynamic stability adresses the way the airplane returns to the equilibrium state after being disturbed, considering restoring and damping forces, as well as mass distribution. If the dynamic motions of the aircraft allow a return to the original flight state, the aircraft is said to be dynamically stable. If not, and the result is an overshot of the original state, causing the airplane to oscillate with increasing amplitude, eventually losing control, it is said to be dynamically unstable [11].

Dynamic stability analysis is complex and demands a computational approach in order to obtain accurate results [11]. Estimation of an aircraft's dynamic motions at a conceptual design level is not exactly straightforward considering the lack of information in conceptual design reference textbooks (viz. [2], [10] and [11]). In order to bypass this obstacle, the author gathers information from references [54], [55] and [56], and adds a new *step* to the spreadsheet approach, in which dynamic stability characteristics are assessed.

The general idea lies in solving the equations of motion and determining the oscillatory modes. The referred equations are governed by pitch, yaw and roll rotations as well as vertical, lateral and longitudinal velocities. Taking into account the airplane symmetry, it is possible to separate the longitudinal system of equations from the lateral-directional one, resulting in two separate systems of equations that characterize both longitudinal and lateral-directional motions [11], [54].

To solve both systems, the following sequence must be observed. Determination of longitudinal and lateral-directional dimensionless derivatives, using semi-empirical relations [54], is the starting step. Calculation of the dimensional derivatives follows. Having these determined, along with information on the aircraft's moments of inertia, computed in accordance with [11], the longitudinal and lateral-directional matrices are filled [54]. Solving for the eingenvalues, one obtains the oscillatory modes for each system of equations, represented in tables 15 and 16.

A dynamic mode is said to be stable if the real part of its eigenvalue is negative. Both longitudinal modes are stable and two of the lateral-directional as well, the dutch roll and roll modes. The spiral mode is unstable, yet, such instability does not necessarily

Table 15: Longitudinal oscillatory modes and their respective natural frequencies, $\omega_n$, and damping factors, $\xi$.

| **Oscillatory Mode** $(a \pm bi)$ | **a** | **b** | $\omega_n$ (rad/s) | $\xi$ |
|---|---|---|---|---|
| Phugoid | -0.0073 | 0.3606 | 0.3607 | 0.0202 |
| Short Period | -2.1047 | 4.6152 | 5.0725 | 0.4149 |

Table 16: Lateral-directional oscillatory modes and their respective natural frequencies, damping factors, time constants, $\tau$, and time to double the amplitude, $t_2$.

| **Oscillatory Mode** $(a \pm bi)$ | **a** | **b** | $\omega_n$ (rad/s) | $\xi$ | $\tau$ | $t_2$ (s) |
|---|---|---|---|---|---|---|
| Dutch Roll | -0.3437 | 3.1724 | 3.19 | 0.1077 | – | – |
| Roll | -11.788 | 0 | – | – | 0.0848 | – |
| Spiral | 0.0433 | 0 | – | – | – | 15.98 |

pose a problem as the time to double the amplitude of motion may be long enough to perform the proper corrections [11].

Flying qualities can be assessed by taking into consideration the aircraft class and the flight phase category. The former is class I (small, light airplanes) and the latter is category B or C, whether the flight phase is a nonterminal one with gradual maneuvers or a terminal one with precise flight path control, respectively [55]. According to flying qualities criteria [56], the short period, dutch roll and roll modes are evaluated as level 1. This means that the flying qualities associated with each mode are adequate for the mission flight phase. The phugoid and spiral modes demonstrate flying qualities of level 2, i.e., the mission flight phase can be accomplished at the cost of an increase in pilot workload and/or degradation in mission effectiveness. Due to the lack of information concerning RPAs, the referred criteria is based on military specifications for piloted airplanes and is employed merely to provide a reference of the conceptual airplane's flying qualities.

## 3.12 Performance

### 3.12.1 Stall Speed & Cruise Velocity Optimization

Stall speed is defined as [10]:

$$V_s = \sqrt{\frac{2W}{\rho S C_{L_{max}}}} \tag{25}$$

Mission requirements demand a maximum stall speed of 55 kts at cruise conditions, with a clean configuration, and a maximum of 45 kts at take-off and landing conditions, with the flaps deployed. Table 17 demonstrates how both requirements are met.

Table 17: Stall speed at different flight conditions.

| **Flight Condition** | **Configuration** | $V_s$ **(kts)** |
|---|---|---|
| Cruise | Clean | 45 |
| Cruise | Flaps | 35 |
| Take-off (MSL) | Flaps | 33 |
| Take-off (10000 ft) | Flaps | 38 |
| Landing (MSL) | Flaps | 31 |
| Landing (10000 ft) | Flaps | 36 |

Performance in steady level flight is assessed by endurance and range. According to the Breguet equations, for propeller-powered aircraft, the former can be maximized by maximizing the endurance parameter, $C_L^{3/2}/C_D$, which is done by flying at the velocity for minimum power. Maximization of range requires maximization of the lift-to-drag ratio, $L/D$, accomplished by cruising at the velocity for minimum thrust. Both velocities can be determined analytically assuming that the zero-lift drag is constant with velocity, and drag due to lift follows the parabolic approximation in which $K$ is constant with velocity. These assumptions are acceptable only in the case of airplanes with high aspect ratio wings flying at low Mach numbers [11]. Indeed, such is the case of the current design. Nonetheless, in order to augment the level of confidence in the results, a graphical analysis is performed, as recommended [11], in which the actual thrust and power required are plotted against the velocity.

In practice, to properly determine the velocities that maximize endurance and range, engine performance has to be considered. However, due to lack of information concerning the latter, the author is unable to perform an accurate assessment. The following results are, therefore, based on the aforementioned theoretical postulates.

Looking up at figure 20, the velocities for minimum thrust and power can be identified as approximately 76 kts and 56 kts respectively. Both curves point to the fact that the specified cruise speed of 90 kts is far from optimizing performance, suggesting the pertinence of a revision and possible redefinition of the mission requirements.

After due consideration and discussion of the topic with the design team, a cruise speed of 70 kts was specified. Such decision is based on a compromise between

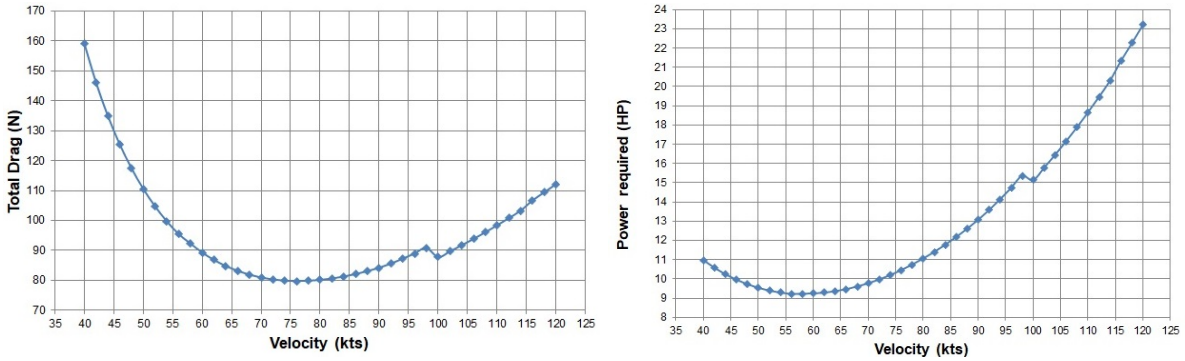


(a) (b)

Figure 20: Thrust (a) and power (b) required vs cruise velocity.

approximating the cruise velocity to the endurance optimization speed (56 kts) and not deviating too far from the initial requirement (90 kts). An additional benefit is the fact that the selected velocity is close to the range optimization speed (76 kts). Naturally, such a fundamental change in the mission requirements demands a new iteration of the whole design process.

### 3.12.2 Steady Climbing, Gliding and Level Turning Flight

Analytical optimization of velocity for rate of climb (ROC) can be cumbersome. Graphical analysis is more reliable and regarded as the most accurate method [11]. In figure 21, rate of climb is plotted against velocity, using actual thrust and drag data (cruise conditions), and determined by identifying the peak of the curve. Table 18 shows the best rate of climb in three different situations: at cruise, take-off at MSL conditions and take-off at 10000 ft. Additionally, the rate of climb attained with the cruise speed of 70 kts and take-off speed is also presented.

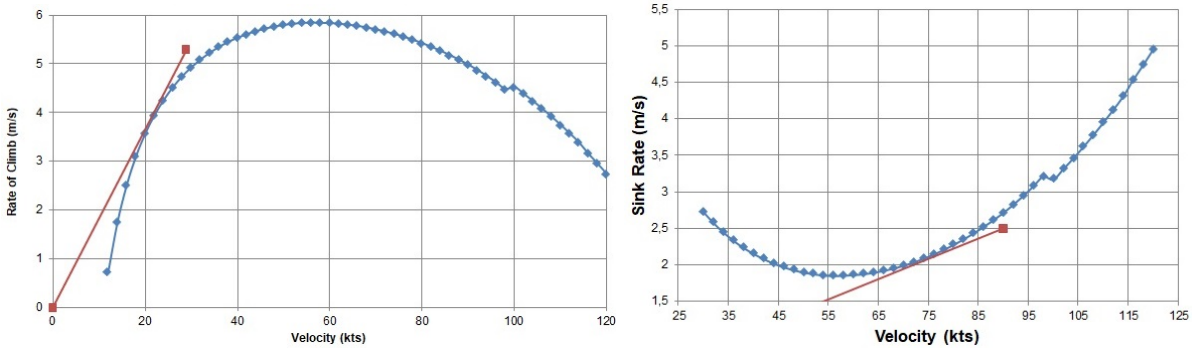


(a) (b)

Figure 21: Climb rate (a) and sink rate (b) vs cruise velocity.

Table 18: Rate of climb at different flight conditions. Flight speed, $V$, and the ratio of flight and stall speed, $V/V_s$, are represented for comparison purposes.

| **Flight Condition** | $ROC$ **(kts)** | $V$ **(kts)** | $V/V_s$ (%) |
|---|---|---|---|
| Best ROC at cruise | 11.4 | 56 | 24 |
| ROC at cruise speed | 11.1 | 76 | 56 |
| Best ROC at MSL | 11.8 | 52 | 58 |
| ROC at MSL & $V_{TO}$ | 11.6 | 36 | 10 |
| Best ROC at 10000 ft | 11.3 | 60 | 58 |
| ROC at 10000 ft & $V_{TO}$ | 10.7 | 36 | 10 |

According to Corke [10], for military aircraft, a minimum climb speed of $1.2V_s$ must be observed. Table 18 demonstrates that the optimimum velocities meet this requirement for every condition considered. It can also be seen that, for the referred conditions, the rate of climb does not change significantly. The design proposal specifies a minimum climb rate of 750 ft/min (7.4 kts) at MTOW, and as table 18 clearly illustrates, the rate of climb is considerably above the required minimum in any flight condition.

In figure 21(a), the point of tangency to the straight line from the origin represents the velocity for best climb angle – 22 kts. Such situation is impractical due to the extremely low velocity required, significantly below the stall speed.

In gliding flight, the thrust is set to zero and the motion of the airplane is determined by the glide ratio (GR), i.e., the ratio between horizontal distance tavelled and altitude lost which is equal to the lift-to-drag ratio. Hence, maximizing this parameter implies flying at the velocity for minimum drag. An additional important parameter is the sink rate (SIR), i.e., the vertical component of velocity which determines how much time the airplane can remain in the air. The best sink rate is achieved when flying at the velocity for minimum power [11].

Table 19: Glide ratio and sink rate at different flight conditions. Flight speed, $V$, and flight and stall speed ratio, $V/V_s$, are represented for comparison purposes.

| **Parameter** | $GR$ | $SIR$ **(kts)** | $V$ **(kts)** | $V/V_s$ |
|---|---|---|---|---|
| Best Glide Ratio | 19 | 4 | 76 | 69 |
| Best Sink Rate | 16.6 | 3.4 | 56 | 24 |
| Cruise at 70 kts | 18.9 | 3.7 | 70 | 56 |

Table 19 displays the graphical results for three different situations. As illustrated, best glide ratio occurs at cruise speed, which minimizes drag and therefore maximizes

$L/D$. Best sink rate occurs at the velocity for minimum power, as expected. Figure 21(b) illustrates the evolution of the sink rate curve, with the point of tangency to a line from the origin representing the velocity for best glide ratio.

Regarding gliding flight, no minimum speed is imposed. For consistency, a safety margin of 20% is assumed. Table 19 illustrates how such margin is respected for every situation under analysis. A minimum glide ratio of 10 is demanded by the design proposal and, as shown, no difficulties arise in meeting the requirements.

Regarding level turning flight, no performance requirements are specified in the design proposal. At cruise conditions, a typical bank angle of 45° results in a turn rate of 15.6 °/s. This means that the aircraft takes roughly 12 seconds to perform a 180° turn and 23 seconds to complete a full circle.

### 3.12.3 Take-off and Landing

Estimation of take-off and landing distances is in accordance with the spreadsheet approach [10], complemented with data from [11]. A detailed discussion of the procedure and its governing equations is outside the scope of this text. However, the following notes are in order.

Take-off comprises four segments: ground roll, rotation, transition and climb (figure 22(a)) [10]. During the ground roll, the forces acting on the aircraft, in the direction of motion, are thrust, drag and the rolling friction of the wheels. The latter is expressed as a rolling friction coefficient, $\mu_r$, whose value depends on the runway surface. Thrust varies with velocity. However, due to lack of data regarding engine performance, a constant value of static thrust is assumed throughout this segment. Drag due to flap deflection is added to the clean configuration drag and the influence of ground effect is take into account. For small aircraft, the rotational time is on the order of one second and the acceleration is assumed to be negligible over such short time interval [11]. The obstacle height is 50 ft, derived from manned aircraft regulations and adopted by RPAS [2].

Landing also comprehends four segments: approach, transition (or flare), free-roll and braking (figure 22(b)) [11]. During the braking segment no thrust is applied and the rolling friction of the wheels is again modeled by the rolling friction coefficient, adapted to account for the braking effect. Braking devices such as spoilers or speed brakes

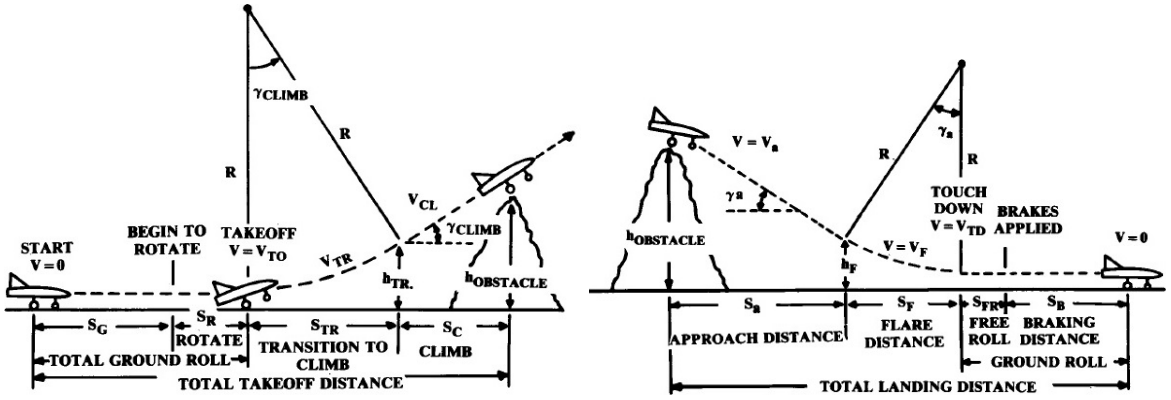


(a) (b)

Figure 22: (a) Take-off and (b) landing breakdown schematic. Adapted from [11].

are not used, therefore the net drag coefficient is the same as the one for take-off. It should be noted that a worst case scenario is assumed in which, at the beginning of the landing phase, the aircraft is carrying half of its take-off fuel weight [10].

Operational requirements demand that the combined portions of ground roll and rotation, in the case of take-off, and free-roll and braking, in the case of landing, remain under 150 meters. Furthermore, the aircraft must be able to take-off and land in gravel and non-prepared runways and at a maximum altitude of 10000 ft. Tables 20 and 21 show the results obtained for the current analysis.

Table 20: Take-off distance under different conditions. All distances in meters.

| **Take-off condition** | $S_G$ | $S_R$ | $S_{TR}$ | $S_C$ | $S_{G+R}$ | **Total distance** |
|---|---|---|---|---|---|---|
| At MSL | 43.3 | 18.5 | 40.3 | 66.4 | 61.8 | 168.5 |
| At 10000 ft | 75.7 | 21.5 | 54.5 | 59.3 | 97.2 | 211 |

Table 21: Landing distance under different conditions. All distances in meters.

| **Landing condition** | $S_A$ | $S_{TR}$ | $S_{FR}$ | $S_B$ | $S_{FR+B}$ | **Total distance** |
|---|---|---|---|---|---|---|
| At MSL | 86.9 | 30.5 | 17.5 | 112.5 | 130 | 247.4 |
| At 10000 ft | 81.6 | 41.3 | 20.4 | 152.2 | 172.6 | 295.5 |

For both altitudes, the resulting distances represent worst case scenarios in terms of the runway's quality, which happens for take-off and landing in wet grass. Regarding take-off, all requirements are met, i.e., the airplane is able to perform the ground roll and rotation under 150 meters, in any type of runway, up to a maximum altitude of 10000 ft. Concerning landing, performance is acceptable at MSL conditions, for any type of

runway, however, at 10000 ft, the minimum free-roll and braking distance is not met. The installation of spoilers in the main wing, which act in order to increase the total drag during braking, therefore reducing the landing distance, was subject to debate by the design team. Considering the trade-off between the benefits of reducing the landing distance and the drawbacks of increasing the aircraft weight, structural analysis and manufacturing complexity, a decision was made not to incorporate these devices in the design. The design team considers that a reduction in landing distance, at an altitude of 10000 ft, can be attained with external devices such as arresting nets.

## 3.13 Aircraft Layout and Characteristics

At this point, in the scope of the present dissertation, conceptual design is completed and a RPA capable of adequately fulfilling the mission requirements is designed. Subsequently, the exterior layout of the aircraft is displayed and its main characteristics summarized. The author points out the fact that a longer endurance above 8 hours is attainable, as shown in table 22.

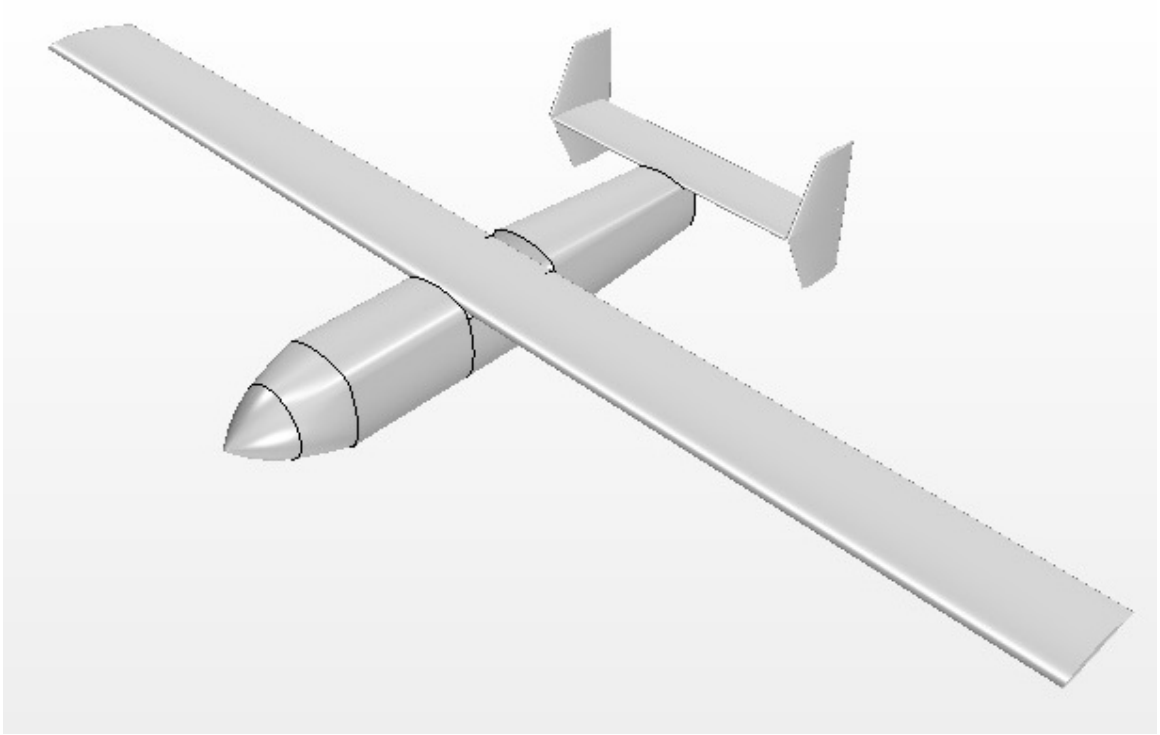

Figure 23: Projected view.

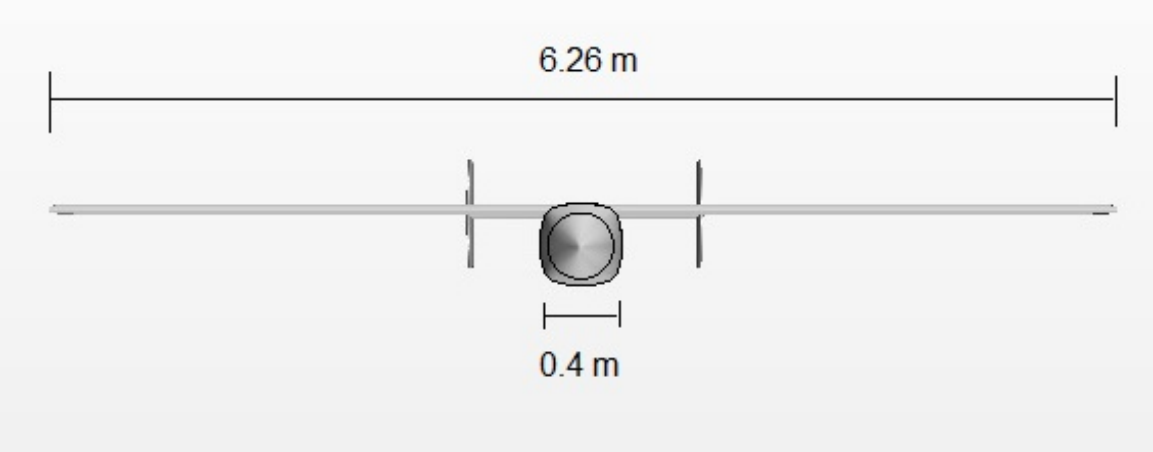


Figure 24: Front view.

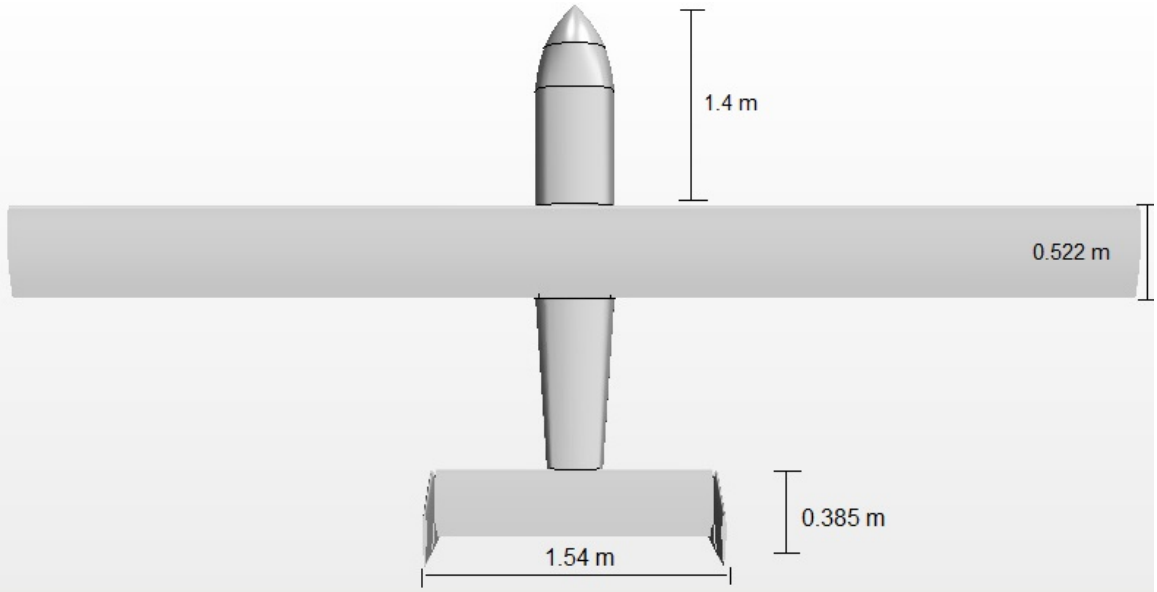


Figure 25: Top view.

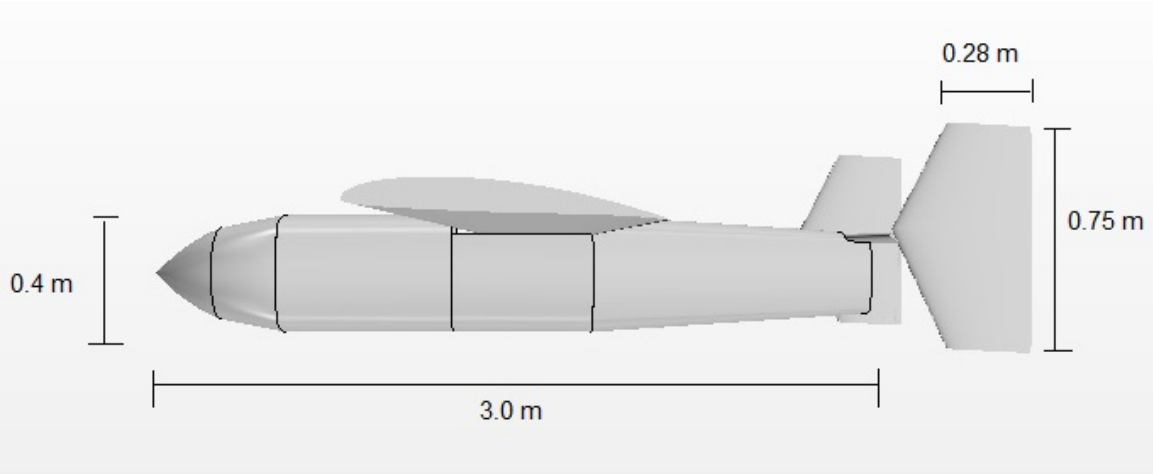


Figure 26: Lateral-projected view.

Table 22: Summary of the aircraft's main characteristics.

| Weights (kg) | | | | | |
|---|---|---|---|---|---|
| $W_{TO}$ | $W_{struct}$ | $W_{pwr}$ | $W_{feq}$ | $W_{PL}$ | $W_{fuel}$ |
| 150 | 50.7 | 19.8 | 33.1 | 16.0 | 30.4 |
| **Cruise Data** | | | | | |
| Altitude (ft) | $V$ (kts) | Mach | Reynolds | AoA (°) | $C_L$ |
| 8000 | 70 | 0.11 | $1 \times 10^6$ | 4 | 0.72 |
| **Main Wing** | | | | | |
| $S\ (m^2)$ | $AR$ | $b$ (m) | $\bar{c}$ (m) | $\alpha_{stall}$ (°) | $C_{L_{max}}$ |
| 3.27 | 12 | 6.26 | 0.522 | 13 | 1.52 |
| **Fuselage** | | | | | |
| Maximum Width (m) | | Maximum Height (m) | | Length (m) | |
| 0.4 | | 0.4 | | 3 | |
| **Horizontal Tail** | | | | | |
| $S_{HT}\ (m^2)$ | $AR$ | $b$ (m) | $\bar{c}$ (m) | $\alpha_{stall}$ (°) | $l_{HT}$ (m) |
| 0.59 | 4 | 1.54 | 0.385 | 15 | 1.19 |
| **Vertical Tail (panel)** | | | | | |
| $S_{VT}\ (m^2)$ | $AR$ | $b$ (m) | $\bar{c}$ (m) | $\alpha_{stall}$ (°) | $l_{VT}$ (m) |
| 0.28 | 2 | 0.75 | 0.377 | 23.5 | 1.19 |
| **Engine Performance** | | | | | |
| $P_{max}$ (HP) | $P_{cruise}$ (HP) | $c_{p_{max}}$ (lb/hp/hr) | $c_{p_{cruise}}$ (lb/hp/hr) | RPM | $\eta_p$ |
| 38 | 10.5 | 0.57 | 0.52 | 7800 | 0.4 |
| **Static Stability** | | | | | |
| $x_{np}$ (m) | $x_{cg}$ (m) | SM (%) | $C_{M_\alpha}$ | $C_{\mathcal{L}_\beta}$ | $C_{n_\beta}$ |
| 1.58 | 1.47 | 20 | -1.09 | 0.08 | -0.05 |
| **Dynamic Stability** | | | | | |
| Phugoid | | | Short Period | | |
| $\omega_n$ (rad/s) | $\xi$ | | $\omega_n$ (rad/s) | $\xi$ | |
| 0.018 | 0.36 | | 5.43 | 0.39 | |
| Dutch Roll | | | Roll | Spiral | |
| $\omega_n$ (rad/s) | $\xi$ | | $\tau$ | $t_2(s)$ | |
| 3.2 | 0.108 | | 0.085 | 15.7 | |
| **Performance at cruise conditions** | | | | | |
| $E$ (h) | $R$ (km) | $V_s$ (kts) | ROC (kts) | GR | SIR (kts) |
| 9h20m | 1570 | 45 | 11 | 18.9 | 3.7 |
| **Performance at MSL** | | | | | |
| $V_{s_{TO}}$ (kts) | $V_{s_{Lan}}$ (kts) | ROC (kts) | $S_{TO}$ (m) | $S_{LAN}$ (m) | |
| 33 | 31 | 12 | 169 | 211 | |
| **Performance at 10000 ft** | | | | | |
| $V_{s_{TO}}$ (kts) | $V_{s_{Lan}}$ (kts) | $ROC(kts)$ | $S_{TO}$ (m) | $S_{LAN}$ (m) | |
| 38 | 36 | 11 | 247 | 296 | |

# 4 Preliminary Design

It is not possible for the present text to encompass all aerodynamic, stability and control analysis conducted during the preliminary design phase. Therefore, the focus is the aerodynamic analysis of the main wing, namely, the parametric study elaborated in order to improve its configuration for the endurance mission. The referred study comprises a set of analyses using the CFD commercial software Star-CCM+ v.8.04. In addition, the author managed to perform further aerodynamic analyses that incorporated the horizontal and vertical tail surfaces. These are also described in the present chapter.

## 4.1 2D Analysis: Methodology Validation

A two-dimensional analysis, where the object of study is the airfoil, is conducted prior to the three-dimensional one in which the object of study is the main wing, therefore dividing the CFD analysis in two phases of increasing complexity. The main reason behind such decision is the simplicity associated with the first case, where a simple airfoil geometry is analysed in the x-y plane, demanding lesser computational and temporal effort, allowing the user to quickly familiarize with the software. Moreover, the existence of published wind tunnel data enables validation of the CFD results and methodology. On top of it, the possibility of correlating the results with reference data easily obtained from XFLR5 simulations enhances the validation process.

### 4.1.1 Methodology Definition

The starting point for the establishment of a robust CFD methodology to be applied in the study of the main wing is the *Best Practice Guidelines in CFD External Aerodynamics: Applied to Unmanned Aerial Vehicles at Cruise Conditions* [28]. This reference presents a set of recommedations regarding geometry definition, mesh generation, selection of physics models, imposition of boundary conditions and solution monitoring, concerning the software of interest: Star-CCM+. It is adequate for the present design project as it was elaborated for use in CFD external aerodynamics applied to RPAs flying at cruise conditions very similiar to the ones in consideration, i.e., with similar Mach and Reynolds numbers.

The airfoil under study is the SG6042. Its coordinates are manipulated at the trailing edge in order to obtain a finite (segment) instead of an infinite trailing edge (point) to provide increased grid quality and numerical stability for future simulations. In order to simulate the flow over the airfoil, a control volume has to be created. For a 2D analysis, this is defined as a square with the object of interest, the airfoil, placed at the center. The far-field distance, measured from the airfoil, should be roughly 60 times the airfoil chord in order to properly simulate the freestream, undisturbed flow [28]. For an airfoil having $\bar{c} = 0.522$ m, half the side of the square will be approximately 32 m (60$\times$0.522).

The physics model should be able to accurately predict the flow field characteristics and phenomena in the domain of interest, specifically near the airfoil. It is divided into several submodels that define specific aspects of the flow physics: space, time, material, flow, equation of state, viscous regime, turbulence model, transition model and wall treatment, all defined in accordance with [28].

Table 23: Best practice guidelines concerning the physics model.

| **Parameter** | Space | Time | Material |
|---|---|---|---|
| **Best practice** | Two-dimensional | Steady | Gas (air) |
| **Parameter** | Flow | Equation of state | Viscous regime |
| **Best practice** | Segregated | Constant density | Turbulent |
| **Parameter** | Turbulence model | Transition model | Wall treatment |
| **Best practice** | RANS with k-$\omega$ SST | $\gamma - Re_\theta$ | Low $y^+$ |

In compliance with an airfoil analysis, two-dimensional space is modeled. In order to solve the steady-state governing equations, a steady model is selected. Since the aircraft moves in the atmosphere, the material is gas (air) and its properties, namely, density, $\rho$, and dynamic viscosity, $\mu$, correspond to cruise altitude conditions.

Segregated flow is modeled because of its incompressible nature ($M = 0.11 < 0.3$). The segregated flow model, in opposition to the coupled flow model, is advantageous in terms of computational resources since it solves the flow governing equations in a segregated, uncoupled manner, i.e., sequentially, one equation after the other, linking them by means of a correction equation. Also linked to the incompressible behaviour of the flow is the equation of state model – constant density. This model is used to compute the density and its derivatives with respect to pressure and temperature. A constant density model assumes that this variable is invariant throughout the entire

domain [57].

Given the Reynolds number of $1 \times 10^6$ that characterizes the flow, boundary layer transition is expected to occur, i.e., the initial portion of the flow over the airfoil is laminar up to the transition region where it begins to develop as turbulent. To model this situation, one defines the viscous regime as turbulent and selects appropriate turbulence and transition models. The recommended turbulence model is the Reynolds-Averaged Navier-Stokes (RANS) with the k-$\omega$ SST model. As discussed in 2.4.2, it demonstrates excellent performance near walls in boundary layer flows, namely under the influence of intense adverse pressure gradients, providing accurate predictions of flow separation phenomena while keeping the sensitivity to freestream/inlet conditions to a minimum.

The $\gamma - Re_\theta$ transition model is selected. According to the investigation performed in 2.4.3, this is a correlation-based model coupled with the k-$\omega$ SST model that offers very good transition prediction capabilities and is perfectly compatible with unstructured CFD codes and aeronautical flow applications. It possesses an important parameter that must be defined by the user: the freestream edge. Definition of this parameter is recommended to be around four times the estimated maximum boundary layer thickness, $\delta$ [28]. To complete the physics model, a low $y^+$ wall treatment model is selected. This one is suitable for low Reynolds number turbulence models, as is the case, and assumes that the viscous sublayer is correctly resolved, which in turn requires a fine mesh near the wall.

Proper definition of boundary conditions is of key importance in assuring that the final solution converges and accurately represents the real flow field phenomena. The upwind (inlet) and lateral boundaries of the control volume must be defined as velocity inlets and the downwind (outlet) boundary as a pressure outlet. This requires the velocity to be defined in terms of its components relative to a reference axis so that, in practice, the velocity is normal to the upwind boundary (inlet) and tangent to the lateral boundaries. The velocity magnitude corresponds to the aircraft cruise speed. Two extremely important parameters that are imposed as boundary conditions are the turbulence intensity, $Tu$, and the turbulent viscosity ratio (TVR), both prescribed at the inlet and as ambient turbulence. Values range from 0.001-0.01 for the former and 1-10 for the latter [28].

Initial conditions specify the initial field data for the simulation. Values of velocity,

turbulence intensity, turbulent viscosity ratio and pressure at the outlet should meet the boundary conditions values so that the simulation might reach the final converged solution faster and reduce computational efforts. However, for steady-state simulations, the final converged solution itself is independent of the initial conditions [57].

Perhaps the most critical aspect in the establishment of a solid CFD methodology for a particular application is the mesh setting. For the sake of clarity, the following discussion is split into three topics: meshers, default controls and custom controls.

Star-CCM+ offers two meshing strategies for unstructured meshing: Parts-Based Meshing (PBM) and Region-Based Meshing (RBM). For better control and automation, since it detaches the meshing from the physics and provides a flexible and repeatable meshing pipeline [57], the first strategy is adopted. The mesh models (meshers) used are the trimmed cell and prism layer meshers. The former offers a robust and efficient method for generating a high quality grid in which cells are predominantly hexahedral with minimal skewness, refinement is based on surface mesh sizing and user-defined controls, and the mesh is aligned with a user specified coordinate system [57]. The latter creates orthogonal prismatic cells next to wall surfaces or boundaries, required to properly solve the governing equations and therefore capture the flow properties inside the boundary layer region. The prism layer mesher stretching function, responsible for providing the formula used in generating the cell layer thickness distribution, is a hyperbolic tangent. The corresponding stretching mode is *wall thickness*. This mode sets the thickness of the layer adjacent to the wall boundary as the starting point for the prism layer generation. Additional parameters of interest are the minimum thickness percentage and layer reduction percentage that are set to 0.01 and 0, respectively, the latter for conformal prisms in all layers [28].

Default controls are the main, generic mesh properties. The base size is recommended to be 10% of the airfoil chord [28]. Due to computational memory and processing constraints, the designer has to limit the base size to a maximum of 20% of the chord. However, values of $C_L$ and $C_D$ obtained with the coarser mesh differ -0.008% and -0.028%, respectively, from the ones obtained with the finer mesh, concluding that the referred limitation does not have a negative impact on the final results. The basic surface curvature ranges from 36 to 54. Cell size ranges from a minimum of 25% of the trailing edge thickness to a maximum of 100% of the chord. A minimum face quality of

0.2 is demanded. Surface growth rate ranges from 1.05 to 1.3 while volumetric growth rates are set to *very slow*. The prism layer around the airfoil is characterized by having 32 layers, a near wall thickness (first cell height), $y_1$, and a total height setting, $\delta$, given by [28]:

$$y_1 = \frac{y^+_{target} \cdot \mu}{\rho \cdot U_\tau} \quad ; \quad U_\tau = \sqrt{0.029 \cdot Re^{-0.2} \cdot V^2} \tag{26}$$

$$\delta \approx 0.37 \cdot Re^{-0.2} \cdot l \tag{27}$$

In the previous set of equations, $y^+_{target}$ represents the target wall $y^+$, preferably in the order of 0.25, $V$ the mean freestream velocity and $l$ the component reference length (airfoil chord). The prism layer total height setting corresponds to the boundary layer thickness estimate.

Custom controls are mandatory on every lifting surface and recommended in the outer boundaries. Mesh refinement close to the airfoil is required in order to properly capture the flow behaviour and solve the governing equations. This is done by generating a nearfield surrounding the airfoil, in which cell size matches the recommended 10% of the chord, and a surface control around the airfoil where the referred parameter is set to 12.5% of the base size. Further refinements at the leading and trailing edges are performed, setting the cell size to 3.125% of the base size. In addition, surface curvature on the airfoil should be increased to 76. In order to capture the airfoil wake, a refinement of 50% of the base size is done up to approximately 10 chords downstream of the lifting surface. Custom controls on the outer boundaries are generated with the purpose of avoiding an unecessary increase in computational effort by limiting the cell size to a minimum of 100% of the chord [28].

The final step in establishing a CFD methodology adresses the solution monitoring. As the software solvers attempt to resolve the flow in the control volume, specific parameters of interest are determined: these consist of the airfoil lift and drag coefficients, $C_l$ and $C_d$, respectively. Such parameters are the ultimate goal of the CFD simulations. Residuals are automatically calculated and plotted for all transported quantities, allowing the user to monitor their evolution as the simulation progresses. A similar set of monitors for $C_l$ and $C_d$ should also be created for the same purposes. The conver-

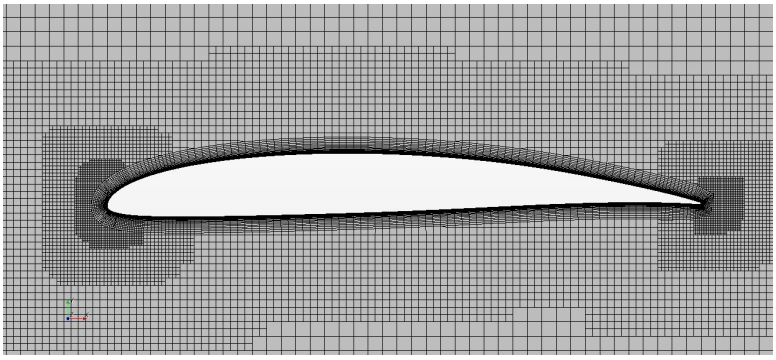

Figure 27: Detail of the 2D mesh surrounding the SG6042 airfoil.

gence criteria is recommended to be the stabilization of residuals and parameters of interest [28].

### 4.1.2 Results & Validation

The test case comprises a series of simulations, each corresponding to a given angle of attack and Reynolds number. The angles of attack range from -2° to 18°. Due to temporal constraints, only even values are submitted to analysis. Both Reynolds numbers of $1 \times 10^6$ and $5 \times 10^5$ are considered. The former defines cruise conditions whilst the latter corresponds to experimental wind tunnel tests conditions [58].

Due to its simplicity and reliability for simple aerodynamic calculations, XFLR5 is employed in order to produce additional results that may cross-validate the ones obtained from CFD simulations. Again, test cases of $Re = 1 \times 10^6$ and $Re = 5 \times 10^5$ are run, with the same variation in angle of attack (-2° to 18°). The airfoil is discretized in 300 panels and the $e^N$ transition criteria with $N_{critic} = 9$ is applied.

The experimental results, displayed for validation purposes, correspond to wind tunnel tests conducted by the Department of Aeronautical and Astronautical Engineering of the University of Illinois at Urbana-Champaign [58]. Unfortunately, these tests were conducted up to a maximum of $Re = 5 \times 10^5$ and therefore do not contemplate a range of Reynolds numbers that encompasses the design conditions. The author could not find available literature that contemplated experimental data of the SG6042 airfoil subject to a Reynolds number of interest. Nevertheless, the CFD methodology is put to the test against experimental data for $Re = 5 \times 10^5$.

Tables 24, 25 and figure 28 display a comparison between numerical and experimental data. Considering figure 28, one may observe how Star-CCM+ results describe

Table 24: Comparison between experimental and computational results for $Re = 5 \times 10^5$. Deviation of the latter from the former is expressed as a percentage. Angles in degrees.

| **AoA** | **Experimental** | | **XFLR5** | | | | **Star-CCM+** | | | |
|---|---|---|---|---|---|---|---|---|---|---|
| | $C_l$ | $C_d$ | $C_l$ | % | $C_d$ | % | $C_l$ | % | $C_d$ | % |
| -2 | 0.30 | 0.0090 | 0.32 | 6.7 | 0.0083 | -7.8 | 0.24 | -20 | 0.0071 | -21.1 |
| 0 | 0.51 | 0.0068 | 0.53 | 3.9 | 0.0065 | -4.4 | 0.45 | -11.8 | 0.0067 | -1.5 |
| 2 | 0.72 | 0.0073 | 0.75 | 4.2 | 0.0064 | -12.3 | 0.68 | -5.6 | 0.0073 | 0 |
| 4 | 0.93 | 0.0090 | 0.94 | 1.1 | 0.0078 | -13.3 | 0.90 | -3.2 | 0.0084 | -6.7 |
| 6 | 1.10 | 0.0126 | 1.11 | 0.9 | 0.0115 | -8.7 | 1.09 | -0.9 | 0.0108 | -14.3 |
| 8 | 1.25 | 0.0170 | 1.26 | 0.8 | 0.0155 | -8.8 | 1.25 | 0 | 0.0145 | -14.7 |
| 10 | 1.38 | 0.0220 | 1.40 | 1.4 | 0.0202 | -8.2 | 1.37 | -0.7 | 0.0214 | -2.7 |
| 12 | 1.46 | 0.0305 | 1.50 | 2.7 | 0.0272 | -10.8 | 1.44 | -1.4 | 0.0321 | 5.2 |
| 14 | 1.50 | 0.0430 | 1.56 | 3.4 | 0.0396 | -7.9 | 1.49 | -0.7 | 0.0442 | 2.6 |
| 16 | 1.49 | – | 1.56 | 4.7 | 0.0609 | – | 1.62 | 8.7 | 0.0728 | – |
| 18 | 1.45 | – | 1.52 | 4.8 | 0.0952 | – | 1.20 | -17.2 | 0.1800 | – |

Table 25: Comparison between experimental and computational results for $Re = 5 \times 10^5$. Deviation of the latter from the former is expressed as a percentage. Angles in degrees.

| **AoA** | **Experimental** | | **XFLR5** | | **Star-CCM+** | |
|---|---|---|---|---|---|---|
| | $C_l/C_d$ | $C_l^{3/2}/C_d$ | $C_l/C_d$ (%) | $C_l^{3/2}/C_d$ (%) | $C_l/C_d$ (%) | $C_l^{3/2}/C_d$ (%) |
| -2 | 33.3 | 18.3 | 15.9 | 19.1 | 1.5 | -9.5 |
| 0 | 75.0 | 53.6 | 8.7 | 10.8 | -10.4 | -15.9 |
| 2 | 98.6 | 83.7 | 18.9 | 21.3 | -5.5 | -8.2 |
| 4 | 103.3 | 99.7 | 16.7 | 17.2 | 3.7 | 2 |
| 6 | 87.3 | 91.6 | 10.5 | 11 | 15.6 | 15 |
| 8 | 73.5 | 82.2 | 10.6 | 10.9 | 17.3 | 17.3 |
| 10 | 62.7 | 73.7 | 10.5 | 11.3 | 2.1 | 1.7 |
| 12 | 47.9 | 57.8 | 15 | 16.8 | -6.3 | -6.9 |
| 14 | 34.9 | 42.7 | 12.9 | 15.2 | -3.2 | -3.4 |

the anticipated behaviour of both lift and drag curves. In fact, it can be seen that, in the linear portion of the $C_l - \alpha$ curve and in the region of minimum drag of the $C_d - C_l$ graph, numerical and experimental results correlate quite favourably, with no immediate distinction between both Reynolds. This points out to the possibility of extrapolating results, i.e., if the CFD methodology is successfully validated for $Re = 5 \times 10^5$, it is safe to assume that, at the least for the referred portions of both curves, it is also validated for $Re = 1 \times 10^6$.

Investigation of table 24 shows that Star-CCM+ predictions tend to underestimate

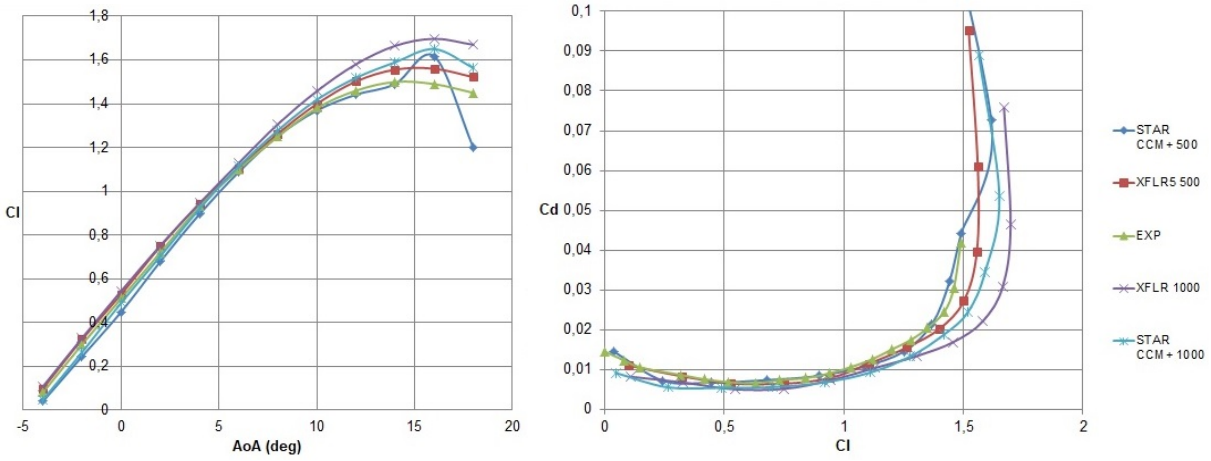


(a) (b)

Figure 28: (a) Lift coefficient vs angle of attack and (b) drag coefficient vs lift coefficient curves for the experimental data and both computational simulations at Reynolds numbers of $1 \times 10^6$ and $5 \times 10^5$.

lift and drag while XFLR5 tends to overestimate lift and underestimate drag. In design, considering that a certain amount of uncertainty is ever present, a conservative approach underpredicts lift and overpredicts drag, therefore establishing a safety margin. It is also observable that Star-CCM+ drag results correlate more favourably with experimental data, while regarding lift XFLR5 shows better agreement. When considering both coefficients together, in the form of lift-to-drag ratio and endurance parameter, Star-CCM+ outperforms XFLR5, as demonstrated in table 25.

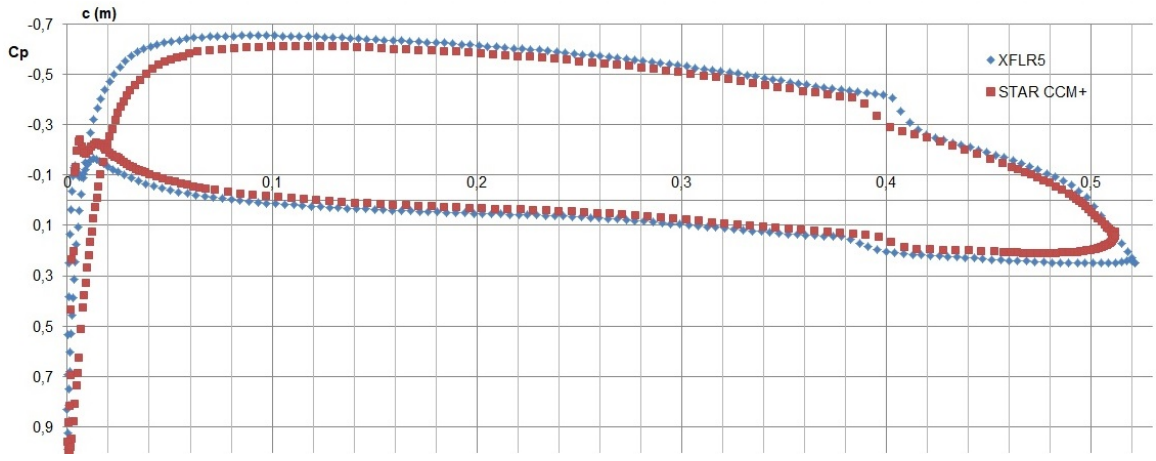


Figure 29: Pressure coefficient distribution over the SG6042 airfoil with AoA=0°and $Re = 1 \times 10^6$.

The pressure distribution over an airfoil constitutes an important parameter in a CFD validation procedure [28]. Pressure coefficient values, for both upper and lower surfaces of the SG6042 airfoil, obtained via computational simulations using Star-CCM+

and XFLR5, are plotted in figure 29. There is an evident resemblance between the results obtained with both tools, a similitude that allows cross-validation of both results. The existence of laminar separation bubbles in the pressure and suction surfaces of the airfoil is represented by each curve (steep variation near c=0.4 m), i.e., as expected, both numerical tools are able to capture such phenomenon. CFD results anticipate and delay the location of the LSB in the suction and pressure surfaces, respectively. The favourable performance demonstrated in predicting the pressure coefficient distribution around the airfoil reinforces the validation of the CFD methodology for the Reynolds number of interest.

In light of the foregoing results, the established CFD methodology is considered validated and may be applied in preliminary design analyses.

### 4.1.3 Application to 3D Flow

The two-dimensional methodology formerly defined can be applied for three-dimensional flows, if compliance with the following remarks is met [28].

For three-dimensional flows, the control volume is defined as an hexahedron and one of its faces corresponds to the wing (aircraft) symmetry plane. This detail points out the simplification of simulating the flow over only half of the body due to its symmetry about the longitudinal axis. The remaining faces correspond to the far-field boundaries (inlet, outlet, top, bottom and lateral boundaries) and must distance 60 chords from the reference object.

The physics model is characterized by a three-dimensional space model to properly simulate 3D flow. The hexahedron face containing the wing root section is defined as a symmetry plane and the lateral far-field boundary as a velocity inlet, with the velocity direction tangent to the surface.

Further refinements are required in order to generate a proper 3D mesh. A custom surface control around the wing tip, similiar to the one created around the leading and trailing edges, should be set, as well as a custom volumetric control downstream of the wing tip, necessary to capture vortices that are shed in these locations. The volumetric control refinement is conducted up to 8 chords downstream of the body, specifying a cell size of 25% of the base size in the y-z plane (perpendicular to the aircraft longitudinal axis).

## 4.2 3D Analysis: Wing Configuration Parametric Study

At the preliminary design level, the main wing is the object of more refined and reliable aerodynamic CFD simulations, conducted in order to determine the best combination of geometric parameters that will, ultimately, define its external configuration. The main goal of this process is to provide a wing geometry that maximizes endurance, keeping in mind the increase in aerodynamic performance against the increase in manufacture and structural design effort.

According to conceptual design predictions, for cruise at 70 kts, the main wing is, by far, the major contributor to the aircraft total drag, being responsible for more than half of it (approximately 60%). It is also estimated that roughly 78% of the wing drag is lift-induced drag. This means that 47%, nearly half of the aircraft total drag, comes from the main wing induced drag, a statistic which is in accordance with the drag discussion performed in 2.2.3.

In light of the foregoing data, the referred parametric study is conducted in order to decrease the main wing lift-induced drag component.

### 4.2.1 Configuration Layout

According to equation 6, the induced drag coefficient is a function of the lift coefficient, $C_L$, aspect ratio, $AR$, and Oswald efficiency factor $e$. For a given set of cruise conditions, the lift coefficient is determined by the need to counter both the aircraft total weight and negative lift produced by the horizontal tail. Therefore, it cannot be changed without adjusting the mission requirements, $W_{TO}$ or trim conditions. For the current analysis, $C_L$ is regarded as a fixed value.

Increasing aspect ratio is, on the one hand, beneficial in terms of aerodynamic performance, as it reduces both the amount of lift lost due to 3D effects and induced drag. On the other hand, it increases the wing weight, which consequently aggravates structural and manufacture complexity. Moreover, high aspect ratio wings are more prone to tip stall and, for constant wing area, produce shorter chords, reducing the likelihood of transition from laminar to turbulent flow. In the event of boundary layer separation, this is a drawback, as the flow will not be able to reattach to the surface. Considering the pros and cons of increasing aspect ratio, a compromise of $AR = 12$ was achieved at conceptual design. For the purpose of the wing parametric study, this

parameter is regarded as immutable.

According to lifting line theory, the elliptic spanwise lift distribution, obtained with an ellipse-shaped wing, gives the minimum induced drag. The Oswald efficiency factor measures the deviation of the actual lift distribution from the ideal elliptic. Therefore, increasing $e$ , i.e., bringing the lift distribution closer to an elliptic one, improves the overall airplane aerodynamic performance [11]. Taper ratio, $\lambda$, and twist angle, $\theta$, both affect lift distribution and so are regarded as the variables of the parametric study.

The starting point for the optimization process is the rectangular untwisted wing, with an aspect ratio of 12 and a planform area of $3.67m^2$, sketched at the conceptual design level. The planform area is determined by wing loading requirements and, therefore, is considered a fixed value.

Defined as the tip chord to root chord ratio, the taper ratio is typically employed in order to approximate the lift distribution to an elliptic lift distribution by means of delineating a trapezoidal planform shape. For unswept wings, taper ratios about 0.4-0.5 minimize $C_{D_i}$ [11]. Parametric studies conducted at a conceptual level show that for a given angle of attack, the endurance parameter is maximized by having a taper ratio in the scope of 0.4-0.6.

The wing twist, $\theta$, is a combination of geometric and aerodynamic twist. In order to avoid unecessary design and manufacture complexity, the option of incorporating aerodynamic twist is put aside, keeping the airfoil section constant. The resulting geometric twist serves two purposes: to prevent tip stall and approximate the lift distribution to an elliptic one. Tapering the wing causes a tip chord reduction which, in turn, reduces the tip Reynolds number, increasing the likelihood of flow separation and stall. Applying *wash-out* (placement of the tip airfoil at a negative angle compared to the root airfoil) reduces the angle of attack of the airfoil sections located near the wing tip, therefore preventing tip stall. *Wash-out* also reshapes the lift distribution due to the angle of attack reduction near the tip. It is, however, of important notice that optimization of the lift distribution by twisting the wing is only valid for a particular lift coefficient and is quite a difficult and complex task to achieve such optimization. As a starting point, a twist angle of -3°, as recommended [11], is selected for the tip airfoil incidence. It varies linearly along the span.

In conformity with the foregoing discussion, the following wing configurations are

selected for CFD analysis.

Table 26: Wing configurations subject to CFD analysis. Twist angle in degrees.

| **Wing Configuration** | A | B | C | D |
|---|---|---|---|---|
| $\lambda$ | 1 | 0.6 | 1 | 0.6 |
| $\theta$ | 0 | 0 | -3 | -3 |

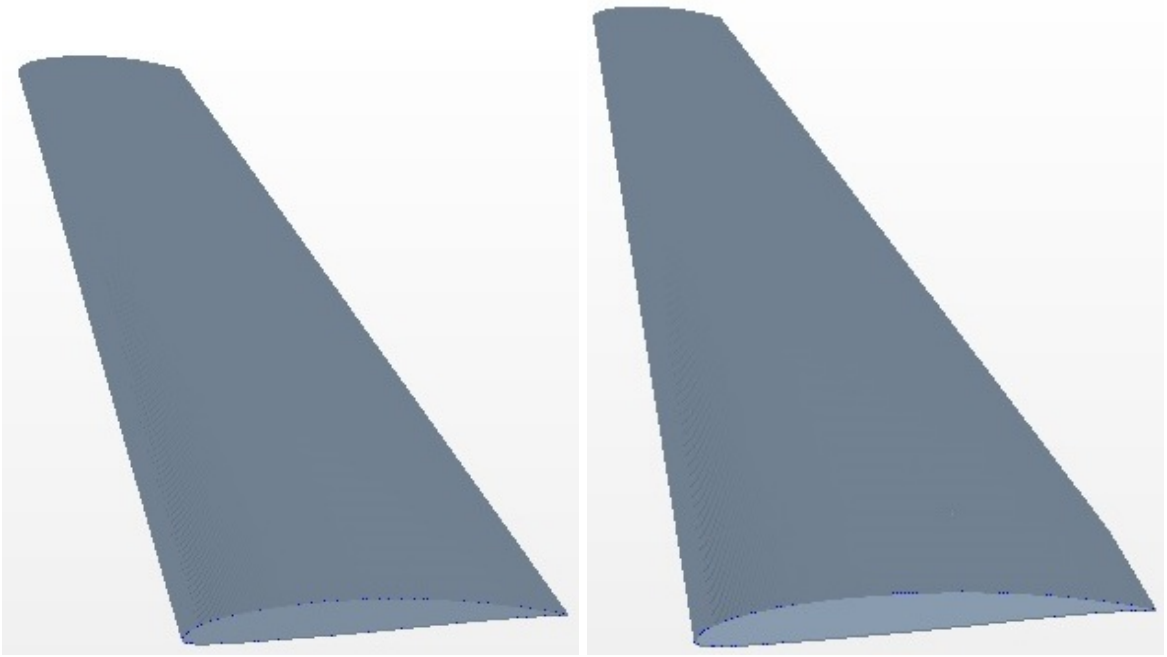

(a) (b)

Figure 30: Configurations A (a) and B (b). C and D have the same planform shape but different twist angles, hard to notice, hence not represented. Only half span is displayed.

When tapered, the wing remains with a zero leading edge sweep angle. This is done to prevent the lift decrease caused by the lower effective dynamic pressure when the wing is swept and also to facilitate the structural design and wing manufacture.

In the wing-fuselage intersection region, the fuselage cross-section has a width of 0.4 m. This means that the first 0.2 m of wing span (considering half span) are located directly above the fuselage. When introducing taper, the wing span remains constant due to the previously referred fixation of its planform area and aspect ratio. Consequently, the root, tip and mean aerodynamic chords are adjusted to comply with $\lambda$. In practice, the root chord increases and the tip decreases. As shown in figure 30(b), the first 0.2 m of wing span have a constant chord equal to the root chord. This results in a slight increment in wing planform area and is done in order to avoid unecessary

structural and manufacture difficulties.

### 4.2.2 Parametric Study Results

Figure 31 displays a comparison between the results obtained with Star-CCM+ and XFLR5 for configuration A. Flow characterized by $Re = 1 \times 10^6$ is simulated in order to represent cruise conditions. Angles of attack of 2°, 4°, 6° and 8° were tested with the CFD tool. The results reveal an excellent agreement with the expected evolution of both curves, i.e., $C_L$ varies linearly with angle of attack and $C_D$ shows a parabolic variation with $C_L$. Star-CCM+ calculations provide lower values of lift and higher values of drag when compared to the ones obtained with XFLR5. This observation is in line with the idea of a more conservative approach of CFD.

The same behaviour is evidenced by the remaining three configurations. However, in order to avoid unecessary repetition of information, the author chose not to display them.

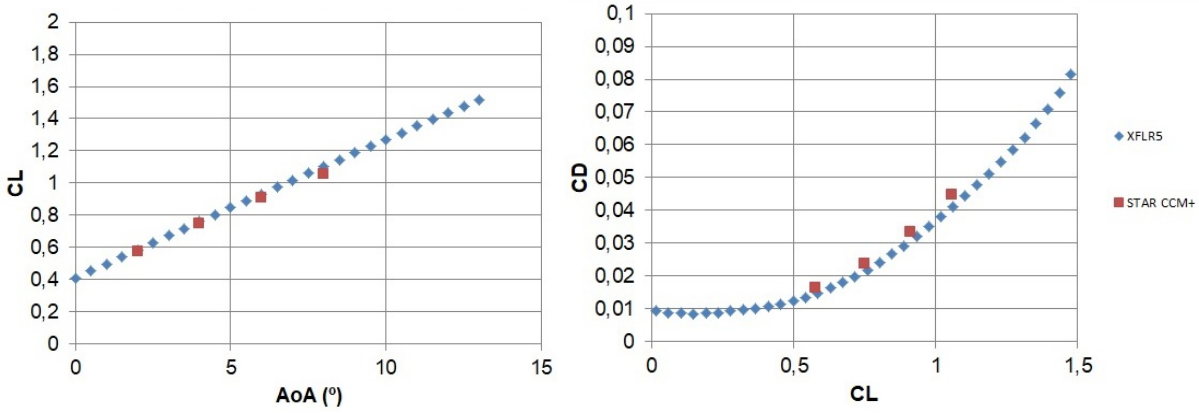


(a) (b)

Figure 31: (a) Lift coefficient vs angle of attack and (b) drag coefficient vs lift coefficient curves for both Star-CCM+ and XFLR5 simulations of configuration A. $Re = 1 \times 10^6$.

In conceptual design, a cruise angle of attack of approximately 4° was determined in order to provide the required amount of lift. Table 27 shows the aerodynamic performance of all four configurations at the referred angle of attack.

Relative to the rectangular, untwisted wing (condiguration A), the tapered, untwisted wing (configuration B) reveals an increment in lift coefficient. This is due to a slight increase in wing surface area, mentioned in the previous section. As a result, the decrement in induced drag caused by introducing taper is offset by the increment in

Table 27: Star-CCM+ results of all four wing configurations at an angle of attack of 4°.

| **Wing Configuration** | $C_L$ | $C_D$ | $C_L/C_D$ | $C_L^{3/2}/C_D$ |
|---|---|---|---|---|
| A | 0.751 | 0.0239 | 31.44 | 27.24 |
| B | 0.761 | 0.0236 | 32.19 | 28.08 |
| C | 0.639 | 0.0182 | 35.14 | 28.10 |
| D | 0.702 | 0.0208 | 33.75 | 28.28 |

lift coefficient. The resulting decrease in drag coefficient is nearly negligible. Still, the aerodynamic performance of configuration B is slightly superior.

The introduction of twist alone (configuration C) causes a considerable decrease in both lift and drag coefficients. The first is explained by the fact that a considerable portion of the wing is operating at lower effective angles of attack and the second due to the reshaping of lift distribution and lower $C_L$. Configuration C outperforms both previous configurations. Combining taper and twist in configuration D results in lift and drag coefficients situated between the ones obtained with configurations B and C. In terms of overall performance, this arrangement is the best for endurance and is surpassed by configuration C for range. It is noticeable that configurations B, C and D have practically the same endurance performance.

The author is aware of the fact that modifying the wing configuration changes the lift coefficient generated, despite keeping a constant angle of attack. This means that the wing is no longer generating the required $C_L$ for steady level flight and must change the angle of attack in order to do so. In practice, configurations B, C and D have to operate at angles of attack different than 4°, resulting in distinct values of $C_L$ and $C_D$.

The ideal procedure would be to examine all four configurations operating at a specific lift coefficient, despite their angle of attack. However, in a CFD simulation, one does not know *a priori* the lift coefficient associated with a particular flight condition. In other words, $C_L$ is an output and not an input to the CFD analysis. Therefore, the temporal effort required to attempt to guess a particular lift coefficient for four distinct wing arrangements would be unbearable.

Nonetheless, the endurance parameters shown in table 27 correspond roughly to their maximum values for each configuration. Even if the operating conditions change to match the cruise requirements, the resulting $C_L^{3/2}/C_D$ will be lower than the one displayed. Therefore, the data collected in table 27 is suitable for comparison purposes

relative to configuration A.

For a clearer understanding of the operational benefit of each configuration, fuel weight fractions and endurance specifications are also displayed.

Table 28: Performance of various wing arrangements.

| **Wing Configuration** | $C_L^{3/2}/C_D$ | $W_{fuel}/W_{T0}$ | $W_{fuel}/W_{T0}$ % | **Endurance** | **Endurance** % |
|---|---|---|---|---|---|
| A | 27.24 | 6.73 | – | 15h49m | – |
| B | 28.08 | 6.54 | 2.90 | 16h18m | 3.09 |
| C | 28.10 | 6.53 | 2.95 | 16h18m | 3.14 |
| D | 28.28 | 6.49 | 3.56 | 16h24m | 3.82 |

The fuel weight fraction represented is defined as the fuel weight required for the endurance mission (eight hours) divided by the total weight of the aircraft and is expressed in the form of a percentage. The *Endurance* column is simply a different way to examine performance. It represents how much time each configuration could remain in the air for the same amount of fuel. Alternatively, both fuel fraction and endurance are expressed as a percentual decrease and increase, respectively, relative to the rectangular, untwisted wing (configuration A) values.

According to the tabled data, the configuration that provides the best aerodynamic performance for the endurance mission is configuration D. It yields the lowest fuel weight fraction and the highest endurance, resulting in an increase of 3.82% (approximately 35 minutes) in endurance relative to configuration A.

It is of key importance to notice that the results under discussion refer to the main wing of the airplane and, therefore, do not reflect the aerodynamic performance of the aircraft as a whole. This is due to the fact that the remaining aircraft components such as fuselage, tail, landing gear and external payload produce drag, yet, have a negligible influence on lift, causing the final total aircraft endurance parameter to decrease significantly when compared to the main wing's alone. Naturally, the benefit of changing the wing configuration, if considering the total aircraft, will be less significant, a reduction that at this stage is hard to estimate. In light of the former examination, considering the humble increment in endurance (3%-4%), and the increase in structural and manufacture complexity associated with the introduction of taper and twist, the design team decides in favour of the rectangular, untwisted wing, i.e., configuration A.

## 4.3 Vertical Tail Planform

Aesthetics is regarded by the design team as a factor that should not be discarded. A rectangular vertical stabilizer is not aesthetically appealing, in fact it is seldomly designed, as the market research demonstrates. Tappering the referred surface improves its looks and may lead to a drag reduction. In order to check the possible aerodynamic advantages of a planform modification, a CFD analysis of the vertical stabilizer at cruise conditions is performed. The geometries subject to analysis are represented in figure 32.

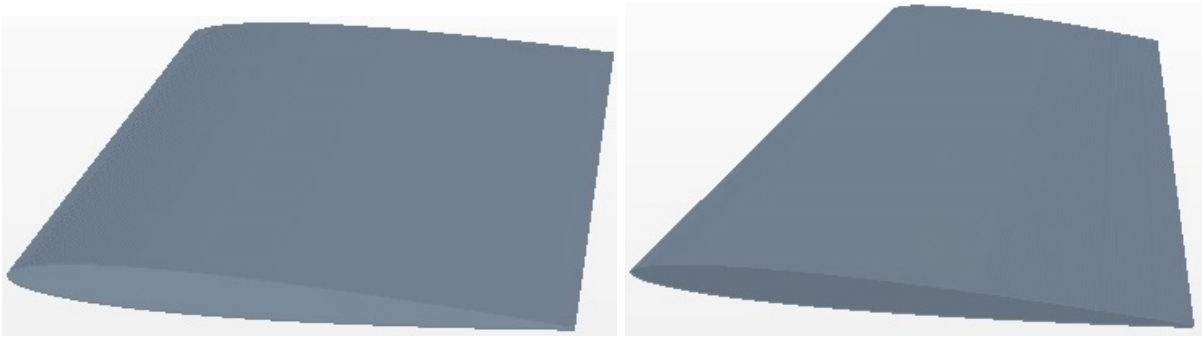

(a) (b)

Figure 32: Rectangular (a) and tapered (b) planforms of each panel of the vertical stabilizer. Only half span is represented.

The modified geometry has a taper ratio of 0.6, based on historic trends [10], whereas the original one has unity taper ratio. This results in a slightly longer root chord and shorter tip chord in order to keep the span and planform area equal. Higher values of $\lambda$ could be used to further decrease drag, however, it would be at the cost of even shorter tip chords, prone to stall and loss of control efficiency.

CFD calculations yield values of 0.66 N for the drag generated by the original geometry and of 0.60 N for the tapered one, i.e., a decrease of roughly 9%. Considering the aircraft overall drag, the aerodynamic benefits of tapering the vertical stabilizers is essentially negligible. However, since the introduction of taper improves aesthetics and, considering the vertical tail's dimensions, does not increase structural and manufacture complexity, the modified geometry is regarded as superior.

## 4.4 Horizontal Tail Incidence

At cruise conditions, for a given tail area and CG position, the horizontal stabilizer must operate at a determined lift coefficient in order to trim the aircraft. This may be accomplished by either setting a tail incidence angle or via a constant elevator deflection [11]. In the design team's view, fixing an incidence angle is the best option since it generates less drag.

A tail lift coefficient of -0.18 is demanded for trimming the airplane. Considering the three-dimensional lift characteristics of the horizontal stabilizer, it would require a horizontal stabilizer angle of attack around -2.8 °to achieve the desired lift coefficient. In truth, this angle is significantly lower due to downwash and endplate effects. The former is due to the main wing vortex system that induces a downstream downwash velocity, decreasing the tail effective angle of attack. The latter is justified by the tail arrangement as an H-tail, i.e., both vertical stabilizer panels act as endplates and decrease the intensity of the tip vortices, increasing the amount of lift generated by the horizontal stabilizer. Both effects have not been accounted thus far and that is precisely the objective of the current section's CFD analysis.

As a starting point, the horizontal tail alone is analysed at cruise conditions to check for drag and lift. The result is D=2.57 N and zero lift, as expected. The drag force is larger than the conceptual design estimate of 1.45 N, which is coherent with the conservative nature of the CFD analysis.

The main wing, with zero incidence, is incorporated into the control volume to quantify the downwash effect. The result is a tail lift coefficient of -0.077. An incidence of 4° is then given to the main wing, representing actual cruise conditions. A new simulation provides -0.15 of lift coefficient. As expected, an increase in the main wing angle of attack intensifies the downwash effect.

Finally, the vertical stabilizer is introduced and another simulation performed. Its output reveals that, at zero incidence and taking into account downwash and endplate effects, $C_{L_{HT}} = -0.18$. In practice, this means that the horizontal stabilizer $C_{L_0}$ is not zero (as expected of a NACA 0009 wing), rather -0.18. Thus, no incidence angle is necessary to provide the required trim lift coefficient.

This concludes the preliminary design analyses conducted in the scope of the present dissertation.

# 5 Conclusions & Recommendations

## 5.1 Conclusions

The objective which the author set out to accomplish was the design of a class I remotely piloted aircraft, intended for maritime surveillance, with special emphasis on aerodynamics, flight stability, exterior design and flight performance, based on a set of mission requirements and performance specifications previously defined. As a longer endurance above the required minimum was considered a key advantage of the system, significant effort was expected in order to maximize this parameter. The vehicle itself was meant to be built at the Air Force Academy Research Center, making use of its facilities and resources. Therefore, cost and feasibility issues constrained the design from the start, guiding the designer towards a necessarily simple, yet reliable, solution.

In compliance with the project demands, an extensive literature review of fundamental concepts concerning three major areas was performed. The first covered the subjects of design, performance and aerodynamics. The aircraft design process was described, flight performance postulates regarding interest areas of the current design were presented, aerodynamics of viscous flows was succintly discussed and an overview of drag components and its reduction techniques conducted. The second part covered the fundamentals of the computational approach to design, focusing on XFOIL, vortex lattice method and computational fluid dynamics (CFD). Ultimately, the state-of-the-art of remotely piloted aircrafts design was discussed, exploring the benefits and drawbacks of different configurations and culminating in a market research.

Chapter 3 provided a detailed description of the aircraft's conceptual design. From early concept generation, selection and initial sizing, followed by the design of the main wing, fuselage, tail surfaces and refined weight, static and dynamic stability analysis, finishing with a performance check, the first of the three major phases of aircraft design was thoroughly scrutinized. The spreadsheet approach proposed by Thomas Corke [10] served as the primary design tool, guiding the author in a step-by-step method that allowed an intuitive and orderly airplane build-up. Whenever possible and appropriate, relevant information from other literary sources, namely [2], [11], [14], and from XFLR5 calculations was added and inputted into the spreadsheets, complementing and enhancing the design.

By the end of chapter 3, conceptual design was completed and a flyable airplane, capable of fulfilling the mission requirements and performance specifications was projected. The author points out the fact that no structural analysis were conducted as such was not in the scope of its work, being assigned to a different designer.

In chapter 4, preliminary design was initiated. Based on the best practice guidelines [28], a solid methodology for CFD analyses was established and employed in three-dimensional simulations of various aircraft components. The nucleus of preliminary design was a parametric study of the main wing for longer endurance. Results demonstrated that, from an aerodynamic point of view, the tapered and twisted wing provided the best performance. However, since the actual increase in endurance was not significant and such configuration resulted in a considerable increase in structural and manufacture complexity, the rectangular untwisted wing prevailed. Subsequently, the vertical stabilizer was subject to analysis in order to define its final planform – untwisted tapered surface. The final design effort gradually incorporated the main wing, horizontal and vertical tail surfaces into one simulation, accounting for downwash and endplate effects and fixing the horizontal stabilizer's incidence angle to guarantee trim at cruise conditions.

The objectives initially outlined were all successfully completed. Conceptual design is consummated and important steps have been taken in the prosecution of preliminary design, which is not yet finished. The author enhances the benefits of being able to go beyond the initial goals and provide valuable information for the remainder of the current project.

## 5.2 Recommendations

The work developed in the course of the present dissertation represents a noteworthy step towards the complete design and development of a class I remotely piloted aircraft for the Portuguese Air Force. However, important tasks remain unaccomplished as temporal and equipment resources available were limited.

Although the main wing parametric analysis failed to provide considerable aerodynamic advantages, the aircraft total drag can still be reduced, and the key advantage of a longer endurance achieved. Such may be accomplished with the introduction of wingtip devices such as winglets. CFD analyses have to be performed in order to assess

the influence of such devices on the overall aircraft drag, and the eventual aerodynamic benefits of their incorporation must be balanced against the drawbacks of increasing weight, structural and manufacture complexity. Other measures such as the use of riblets and reduction of the surface roughness can also be employed to reduce parasitic drag and improve aerodynamic performance.

CFD analyses of the flow over the vehicle at cruise conditions were performed, in which the main wing, horizontal and vertical stabilizers were modeled, therefore representing the aircraft. The remaining components should be gradually incorporated in these analyses in order to provide a more realistic representation of the actual airplane. The presence of a fuselage under a specific section of the wing results in an actual lower lift coefficient which in turn causes its incidence angle to be higher than expected. The same effect occurs for the horizontal tail. As such, including the fuselage should be the next move as it would allow for a more precise estimate of the required angle of incidence of the main wing and horizontal tail. After that, the remaining components such as landing gear struts and wheels, propeller and external payload should also be modeled. Performing a full-configuration analysis is paramount as it provides insight into the flowfield phenomena that characterizes cruise flight and yields a more precise estimate of the aircraft total drag, lift and pitching moment.

Furthermore, the author suggests using CFD as a tool to determine the aerodynamic derivatives for stability, considering all three directions of motion, as well as to model the control surfaces and enhanced lift devices (ailerons, elevator, rudder and flaps) and determine the aerodynamic derivatives for control.

Ideally, CFD should be complemented with experimental wind tunnel tests. However, the author is aware of the inherent difficulties of the latter in the Portuguese Air Force due to the lack of available qualified personnel.

If the former recommendations are followed and the remainder of the design team is able to provide an accurate, computational, finite-element based, structural analysis of the complete aircraft, preliminary design may be considered accomplished. Detail design must follow, with the identification of each and every component and subcomponent of the aircraft, and the integration of all systems and subsystems. The final output must be a series of drawings detailing the internal and external layout of the airplane, which by then can be assumed ready for manufacture.

# References


[1] BARNHART, Richard K. [et al.] – **Introduction to Unmanned Aircraft Systems**. Boca Raton: CRC Press Taylor & Francis Group, 2012. ISBN 978-1-4398-3520-3

[2] GUNDLACH, Jay – **Designing Unmanned Aircraft Systems: A Comprehensive Approach.** Reston: American Institute of Aeronautics and Astronautics, Inc., 2012. ISBN 978-1-60086-843-6

[3] CORNELL, Doug [et al.] – World Military Unmanned Aerial Systems: Market Profile and Forecast, Teal Group Corporation [Online]. 2017. Updated 08 Nov. 2017. [Acessed 25 Jan. 2018]. Available at WWW:<URL:http://www.tealgroup.com/index.php/pages/press-releases/47-teal-group-predicts-worldwide-military-uav-production-of-80-billion-over-the-next-decade-in-its-2017-uav-market-profile-and-forecast>.

[4] AUSTIN, Reg – **Unmanned Aircraft Systems: UAVS Design, Development and Deployment**. Chichester: John Wiley & Sons Ltd, 2010. ISBN 978-0-470-05819-0

[5] FORÇA AÉREA – **MFA 500-12: Visão Estratégica Para Sistemas De Aeronaves Não Tripuladas**. [s.l.]: [s.n.], 2013.

[6] MARQUES, Rafael – Capacidade ISR Na Força Aérea Portuguesa: Competências Atuais e Perspetivas Futuras de Aplicação de UAS. Revista Científica da Academia da Força Aérea. Sintra. ISSN 2182-2174. N°6 (2016), p. 16-27.

[7] MORGADO, José Augusto; DE SOUSA, João Tasso Borges – O Programa de Investigação e Tecnologia em Veículos Autónomos Não Tripulados da Academia da Força Aérea. Cadernos do IDN. Lisboa. ISSN 1646-4397. N° 4 (2009), p. 9-24.

[8] MORGADO, José Passos – Centro de Investigação da Academia da Força Aérea: Atividades de Investigação, Desenvolvimento & Inovação na Área dos Sistemas Aéreos Autónomos Não-Tripulados. Cidadania e Defesa. Lisboa. N° 53 (2015), p. 16-21.

[9] MARINHA – Portugal, uma nação marítima. [Online]. [Acessed 18 Feb. 2018]. Available at WWW:<URL:http://www.marinha.pt/pt-pt/historia-estrategia/estrategia/folhetospt/Portugal_uma_nacao_maritima.pdf.>.

[10] CORKE, Thomas C. – **Design Of Aircraft.** New Jersey: Pearson Education, Inc., 2003. ISBN 0-13-089234-3

[11] RAYMER, Daniel P. – **Aircraft Design: A Conceptual Approach.** 2nd ed. Washington: American Institute of Aeronautics and Astronautics, Inc., 1992. ISBN 0-930403-51-7

[12] BRANDT, Steven A. [et al.] – **Introduction to Aeronautics: A Design Perspective**. 2nd ed. Reston: American Institute of Aeronautics and Astronautics, Inc., 2004. ISBN 1-56347-701-7

[13] NICOLAI, Leland – Designing the Engineer. Aerospace America. [s.l.]. (1992), p. 72-78.

[14] SADRAEY, Mohammad – **Aircraft Performance: Analysis.** Saarbrücken: VDM Verlag Dr. Müller, 2009. ISBN 978-3639200133

[15] GUNSTON, Bill – **The Cambridge Aerospace Dictionary**. 2nd ed. New York: Cambridge University Press, 2009. ISBN 978-0-521-19165-4

[16] ROSKAM, Jan; LAN, Chuan-Tau Edward – **Airplane Aerodynamics and Performance**. Lawrence: Design, Analysis and Research Corporation, 1997. ISBN 1-884885-44-6

[17] ANDERSON, John D. – **Fundamentals of Aerodynamics**. 3rd ed. New York: McGraw-Hill, Inc., 2001. ISBN 0-07-237335-0

[18] KUETHE, Arnold M.; CHOW, Chuen-Yen – **Foundations of Aerodynamics: Bases of Aerodynamic Design**. 4th ed. New York: John Wiley & Sons, Inc., 1986. ISBN 0-471-85954-0

[19] MUELLER, Thomas J.; DELAURIER, James D. – Aerodynamics of Small Vehicles. Annual Review of Fluid Mechanics. [s.l.]. ISSN 1545-4479. Vol. 35, (2003), p. 89-111.

[20] INCROPERA, Frank P. [et al.] – **Fundamentals of Heat and Mass Transfer**. 6th ed. [s.l.]: John Wiley & Sons, Inc., 2007. ISBN 978-0-471-45728-2

[21] LANGTRY, R.B.; MENTER, F.R. – Transition Modeling for General CFD Applications in Aeronautics. AIAA Paper 2005-522. [s.l.]. (2005), p. 1-14.

[22] DE BREDERODE, Vasco – **Fundamentos de Aerodinâmica Incompressível**. 1st ed. Lisboa: [s.n.], 1997. ISBN 972-97402-0-8

[23] JAHANMIRI, Mohsen – Aircraft Drag Reduction: An Overview. Research Report 2011:02. [s.l.]. ISSN 1652-8549. (2011), p. 1-32.

[24] HOERNER, Sighard F. – **Fluid Dynamic Drag: Practical Information on Aerodynamic Drag and Hydrodynamic Resistance**. [s.l.]: [s.n.],1965.

[25] GUR, Ohad; MASON, William H.; SCHETZ, Joseph A. – Full Configuration Drag Estimation. Journal of Aircraft. [s.l.]. ISSN 0021-8669. Vol. 47, n°4 (2010), p. 1356-1367.

[26] HOUGHTON, E.L.; CARPENTER, P.W. – **Aerodynamics for Engineering Students**. 5th ed. Oxford: Butterworth-Heinemann, 2003. ISBN 0-7506-5111-3

[27] CUMMINGS, Russel M. [et al.] – **Applied Computational Aerodynamics: A Modern Engineering Approach**. 1st ed. Cambridge: Cambridge University Press, 2015. ISBN 978-1107053748

[28] VERÍSSIMO, Ricardo José Cabral – **Best Practice Guidelines in CFD External Aerodynamics: Applied to Unmanned Aerial Vehicles at Cruise Conditions**. Sintra: Academia da Força Aérea, 2016. Masters Dissertation.

[29] DRELA, Mark; YOUNGREN, Harold – **XFOIL 6.94 User Guide**. [s.l.]: [s.n.], 2001.

[30] DRELA, Mark – XFOIL: An Analysis and Design System for Low Reynolds Number Airfoils. In Low Reynolds Number Aerodynamics. Berlin: Springer-Verlag, 1989. ISBN 978-3-540-51884-3. p. 1-12.

[31] BERTIN, John J.; CUMMINGS, Russel M. – **Aerodynamics for Engineers**. 5th ed. New Jersey: Pearson Education, Inc., 2009. ISBN 0-13-235521-3

[32] KATZ, Joseph; PLOTKIN, Allen – **Low Speed Aerodynamics**. 2nd ed. New York: Cambridge University Press, 2001. ISBN 978-0-521-66219-2

[33] VAN INGEN, J.L. – The $e^N$ Method for Transition Prediction. Historical Review of Work at TU Delft. AIAA Paper 2008-3830. [s.l.]. (2008), p. 1-49.

[34] SMITH, A.M.O.; GAMBERONI, M. – Transition, Pressure Gradient and Stability Theory. DAC Technical Report ES-26388. [s.l.]. (1956).

[35] ANDERSON, John D. – **Computational Fluid Dynamics: The Basics with Applications**. New York: McGraw-Hill, Inc., 1995. ISBN 0-07-001685-2

[36] CASEY, Michael; WINTERGERST, Torsten – **ERCOFTAC Special Interest Group on "Quality and Trust in Industrial CFD": Best Practice Guidelines**. 1st ed. London: ERCOFTAC, 2000.

[37] HIRSCH, Charles – **Numerical Computation of Internal & External Flows**. 2nd ed. Oxford: Butterworth-Heinemann, 2007. ISBN 978-0-7506-6594-0

[38] FERZIGER, Joel H.; PERIĆ, Milovan – **Computational Methods for Fluid Dynamics**. 3rd ed. Berlin: Springer-Verlag, 2002. ISBN 3-540-42074-6

[39] MENTER, Florian R. – Turbulence Modeling for Engineering Flows. A Technical Paper from ANSYS, Inc. [s.l.]. (2011), p. 1-25.

[40] WILCOX, David C. – **Turbulence Modeling for CFD**. La Cañada: DCW Industries, Inc., 1994. ISBN 0-9636051-0-0

[41] LAUNDER, B.E.; SPALDING, D.B. – The Numerical Computation of Turbulent Flows. Computer Methods in Applied Mechanics and Engineering. [s.l.]. ISSN 0045-7825. Vol. 3, n°2 (1974), p. 269-289.

[42] MENTER, Florian R. – Influence of Freestream Values on $k-\omega$ Turbulence Model Predictions. AIAA Journal. [s.l.]. ISSN 0001-1452. Vol. 30, n°6 (1992), p. 1657-1659.

[43] MENTER, Florian R. – Zonal Two-Equation $k-\omega$ Turbulence Models for Aerodynamic Flows. AIAA Paper 93-2906. [s.l.]. (1993), p. 1-21.

[44] CHEN, H.C.; PATEL, V.C. – Near-Wall Turbulence Models for Complex Flows Including Separation. AIAA Journal. [s.l.]. ISSN 0001-1452. Vol. 26, n°6 (1988), p. 641-648.

[45] KALITZIN, Georgi [et al.] – Near-Wall Behavior of RANS Turbulence Models and Implications for Wall Functions. Journal of Computational Physics. [s.l.]. ISSN 0021-9991. Vol. 204, n°1 (2005), p. 265-291.

[46] ARCTURUS UAV – **TASE 400 DXR**. [Online]. [s.l.]: [s.n.]. [Acessed 11 Apr. 2018]. Available at WWW:<URL:https://arcturus-uav.com/product/tase-400-dxr>.

[47] SHEPARD – **Unmanned Vehicles Handbook.** Slough: The Shepard Press, 2008.

[48] INNOCON – **MiniFalcon Tactical UAV Family**. [Online]. [s.l.]: [s.n.]. [Acessed. 26 Feb. 2018]. Available at WWW:<URL:http://www.innoconltd.com/?CategoryID=180&ArticleID=105>.

[49] TEKEVER – **AR5 LIFE RAY EVOLUTION**. [Online]. [s.l.]: [s.n.]. [Acessed 26 Feb. 2018]. Available WWW:<URL:http://airray.tekever.com/ar5/>.

[50] SAATY, Thomas L. – Decision making with the analytic hierarchy process. International Journal of Services Sciences. [s.l.]. ISSN 1753-1454. Vol. 1, n°1 (2008), p. 83-98.

[51] MOREIRA, E. E. T.; SCHWENING, G. S.; ABDALLA, A. M. – An Application of AHP, TOPSIS-Fuzzy and Genetic Algorithm in Conceptual Aircraft Design. CEAS Air & Space Conference Paper. [s.l.]. (2013), p. 1-9.

[52] ABBOT, Ira H.; VON DOENHOFF, Albert E. – **Theory of Wing Sections: Including A Summary Of Airfoil Data.** New York: Dover Publications, Inc., 1959. ISBN 0-486-60586-8

[53] UIUC Applied Aerodynamics Group. Department of Aerospace Engineering. **UIUC Airfoil Coordinates Database.** [Online]. Illinois: [s.n.]. [Acessed 20 May 2017]. Available at WWW:<URL:http://m-selig.ae.illinois.edu/ads/coorddatabase.html>.

[54] ETKIN, Bernard; REID, Lloyd Duff – **Dynamics of Flight: Stability and Control**. 3rd ed. New York: John Wiley & Sons, Inc., 1996. ISBN 0-471-03418-5

[55] NELSON, Robert C. – **Flight Stability and Automatic Control**. 2nd. ed. Singapore: The McGraw-Hill Companies, Inc., 1998. ISBN 0-07-046273-9

[56] ROSKAM, Jan – **Airplane Flight Dynamics and Automatic Flight Controls**. Lawrence: Design, Analysis and Research Corporation, 2001. ISBN 1-884885-17-9. Pt. I.

[57] CD-ADAPCO – **Star-CCM+ Version 8.04 User Guide**. [s.l.]: [s.n.], 2013.

[58] LYON, Cristopher A. [et al.] – **Summary of Low-Speed Airfoil Data**. Virginia Beach: SoarTech Publications, 1997. ISBN 0-9646747-3-4. Vol. 3.